JACOBS UNIVERSITY

Molecular Modeling and Investigation of Ultrafast Dynamics in Nano-systems

by

Khadga Jung Karki

A thesis submitted in partial fulfillment
of the requirements for the degree of

Doctor of Philosophy
in
Computational Chemistry and Chemical Physics

Approved Dissertation Committee

Prof. Dr. Danilo Roccatano
Jacobs University Bremen, Bremen

Prof. Dr. Arnulf Materny
Jacobs University Bremen, Bremen

Dr. Giuseppe Milano
University of Salerno, Salerno

Date of Defense:
16th December 2011

School of Engineering and Science

Abstract

In this PhD thesis, the results of molecular dynamics simulation studies of structural properties of nano-aggregates and experimental time-resolved spectroscopy studies of exciton dynamics in nano-structures of chromophores are presented.

The OPLS force field parameters of chlorophyll a, astaxanthin (a carotenoid) and phenyltrimethoxysilane molecules are developed to study their structural, physical and thermodynamic properties in solution using classical molecular dynamics simulations. Simulations of chlorophyll a in different solvents show formation of monomeric, dimeric and multimeric structures in methanol, benzene and water, respectively. The structures of the aggregates show that different functional groups present in the ring of the molecule, hydrophobicity of the phytol tail and the water molecules coordinated to the Mg of the chlorin ring play important role in aggregation. Simulations of astaxanthin in water and ethanol mixtures show formation of aggregates in the mixtures in which the water content is more than 50%. The results show that hydrophobicity of the conjugated chain in astaxanthin plays a major role in aggregation.

Apart from the natural systems like light-harvesting complexes, chlorophylls and carotenoids also aggregate on surfaces. In light-harvesting complexes, the aggregation is controlled by proteins in such a way that the aggregates efficiently collect sunlight, which the plants use for photosynthesis. Such a controlled aggregation is also necessary to develop nano-antennas of these chromophores for artificial photosynthesis or other photovoltaic systems. One of the ways to control their aggregation in surfaces is to change the hydrophobicity of the surface. For this reason, a molecular model of the phenyltrimethoxysilane has been parameterized to model hydrophobic phenyl-functionalized inorganic surfaces like silica surface.

Functioning of nano-assemblies of chromophores for photovoltaic application relies on formation of excitons, their motion, energy dissipation, charge separation, etc. that follow the absorption of photons. The processes like formation of excitons and

charge separation are desirable while energy dissipation by vibrational relaxation are undesirable. In order to control aggregation such that the desirable functions are maximized, the different processes occurring in the nano-aggregates need to investigated. These processes, which occur in femto-second to pico-second timescales, can be studied using different techniques of time-resolved spectroscopy. However, the widely used techniques in time-resolved spectroscopy do not have spatial resolution high enough to study dynamics in individual nano-structures or nano-meter or sub-nanometer thin layers of chromophores. The experimental work presented here present the development and implementation of two techniques: near-field pump-probe technique to study the ultra-fast processes in nano-structures with 100 nm spatial resolution, and transient grating technique to study ultra-fast processes in few to sub-nanometer thin films of chromophores. Results of the investigation of exciton dynamics using the two techniques on 3,4,9,10 Perylenetetracarboxylic dianhydride show ultra-fast exciton annihilation and self-trapping of excitons at high exciton densities. The results also show that the pump-probe spectroscopy using the near field technique allows one to quantify the annihilation rate and diffusion constant of the excitons in nanocrystals. These techniques can also be used to investigate ultra-fast processes in the nano-structures of chlorophylls, carotenoids and their derivatives on functionalized surfaces.

Acknowledgements

I would like to thank my advisors for giving me the opportunity to work on a truly transdisciplinary project. This work would not have been possible without their continued support and guidance. I thank the members of the research groups involved in this work for their wonderful help and good time.

Financial support from NANOFUN Research Center (Jacobs University Bremen) for my doctoral stipend and DFG (MA-17 Femto-opt.Nahfeld) for the costs of the experiments are thankfully acknowledged.

To my parents.

Contents

List of Tables

List of Figures

Chapter 1

Introduction

This thesis describes the development of some molecular models to study aggregation phenomena and experimental techniques to study ultra-fast processes in molecular aggregates.

Some molecules self-assemble spontaneously into stable aggregates. This self-assembly is directed by multiple weak, reversible interactions – hydrogen bonds, ionic bonds and van der Waals interactions [1]. Self-assembly is common in nature; many biological structures like membranes, protein complexes (e.g. light harvesting complexes [2]), double helical DNA strands are self-assembled. These biological nano-structures have a large variety of functions that enable the complex machinery of life. Among them, the light harvesting complexes composed of proteins and self assembled chromophores, chlorophylls and carotenoids, are particularly interesting for investigating photo-chemical and photo-physical processes in nano-structures of biological or organic molecules.

Chrorophylls and carotenoids collect sunlight necessary for photosynthesis. Photosynthesis is an elaborate physico-chemical process, which begins with collection of the light energy and ends in the production of glucose, a source of chemical energy. One of the steps in the process involves splitting off of protons from water molecules.

This is a highly energetic process, which cannot be accomplished using only the energy absorbed by a single chromophore from the sunlight. To overcome this problem, chromophores are assembled into large antenna complexes consisting of hundreds of chlorophylls and carotenoids, which collect a large number of photons and funnel the energy to the reaction center in the photosystems where the splitting of water occurs [2]. Chlorophylls and carotenoids in the light harvesting complexes are located in the hydrophobic core of the thylakoid membrane of chloroplasts. However, they can also self-assemble, under appropriate conditions, in different model environments [4, 5]. The investigation of dynamic, structural and functional properties of such assemblies provides insight into how the aggregation process occurs and how the molecular environment influences the process. This information is very important to understand the self-assembly of the molecules and their functionality in the light harvesting systems.

Structural properties of aqueous aggregates are not easily accessible to experimental techniques. On the other hand, computational techniques, like molecular dynamics (MD) simulations, provide insight into the structural as well as dynamic properties of the aggregates with atomistic details. A short introduction to the MD simulations is presented in Chapter 2.

In this thesis, various properties of chlorophyll A (ChlA) – one of the most abundant chlorophylls in the nature –, and astaxanthin (AXT) – a carotenoid – are studied with molecular modeling and MD simulations.

Aggregation of ChlA has been observed in aqueous environments (see references in Chapter 3). Aggregation of ChlA in non-aqueous or mixed solutions is difficult to predict because of many functional groups present in the molecule. Some aggregation mechanisms have been postulated, which, however, have not been conclusively verified by experiments (see Chapter 3). In this context, MD simulations can be useful to study molecular interactions and aggregations with atomistic details. Chapter 3

describes the MD simulations of ChlA done in three different solvents, *viz*; water, methanol and benzene, which have different polarities and dielectric constants. The interaction of ChlA with the solvent molecules and their effect on aggregation are studied.

AXT is a xanthophyll (a carotenoid containing oxygen atoms), which is commonly found in aquatic animals. It is hydrophobic and aggregates in aqueous environment. The absorption spectrum of AXT depends on the structure of the aggregates; the blue and the red shifted absorption spectra observed in water-alcohol co-solvent mixtures with high and low water content, have been attributed to the formation of H- and J-aggregates, respectively. However, the exact structure of the aggregates and the role of the different interactions, like hydrophobic and hydrogen bonding interactions, on aggregation are not well known. We have used MD simulations to get insight into the details of the aggregation process. The results of the investigations are presented in Chapter 4.

Chlorophylls, carotenoids and their derivatives like chlorophyllides and porphyrins can also self assemble on inorganic surfaces. The models of the molecules presented in Chapters 3 and 4 can be used to investigate the properties of their aggregates on organic and inorganic surfaces using MD simulations. However, for practical applications like photo-voltaics, the structure of the aggregates need to controlled and fine tuned to minimize energy losses. As is shown in Chapters 3 and 4, hydrophobicity of the molecules can be exploited to control their aggregation. For this reason, it is desirable to model functional groups that impart hydrophobicity to inorganic surfaces. Chapter 5 of this thesis describes the modeling of liquid Phenyltrimethoxysilane (PhTMS). This compound is commonly used to functionalize silica surfaces with phenyl groups to produce hydrophobic surfaces. The model has been parameterized to reproduce various physical and thermodynamic properties of the liquid PhTMS

and the parameters of the model will be used to model hydrophobic phenyl groups on silica surfaces in the prospective works of the project in the near future.

For the practical applications of nano-aggregates, fundamental processes like charge transfer, energy transfer, formation of excitons, etc. need to be considered. In nano-aggregates of chromophores, which are important for photovoltaic applications, fundamental processes like absorption of photons and excitation into excited states, formation of excitons, their diffusion and trapping, charge separation, energy dissipation, etc. can be influenced by changing the size and the structure of the aggregates. Theoretical or computational investigation of these processes requires use of the principles of quantum mechanics, which is impractical for nano-systems; no standard computational methodology exists that can predict structure and dynamics of a system consisting of thousands of atoms just using the principles of quantum mechanics. However, these fundamental processes, which occur in femto-second to pico-second time scales, can be studied by applying the different techniques of time-resolved spectroscopy using ultra-short laser pulses; the pulses usually have few femto-seconds to pico-seconds durations. A brief introduction to time resolved spectroscopy is provided in Chapter 6.

The different techniques, like pump-probe spectroscopy, of time-resolved spectroscopy that are used extensively to study ultra-fast processes in solids, liquids and gases do not have spatial resolution high enough to study the dynamics in individual nano-systems. The spatial resolution is given by the interaction volume of the laser spot with the sample, which can be few to tens of microns depending on the setup of the experiments. When these techniques are used to study the ultra-fast processes in nano-aggregates, dynamics of an ensemble consisting of large number of nano-aggregates with different sizes and structures is obtained. On the other hand, spatially resolved dynamics in individual nano-aggregate can be useful in understanding how the size and the structure of the aggregate affect the different processes.

One of the ways to improve the spatial resolution in time-resolved spectroscopy is to combine the techniques with scanning near field optical microscopy (SNOM). Implementation of pump-probe spectroscopy with SNOM (PPSNOM) allows recording the ultra-fast dynamics with few tens of nano-meter lateral spatial resolution. In the implementation that is used in the experiments described in Chapter 7 a pump laser pulse is used to excite the sample to an excited state and the absorption of another probe laser pulse at various time delays after the pump pulse is recorded using 100-150 nm (diameter) optical fiber tips placed few nano-meters above the sample. In this technique, the spatial resolution is given by the tip of the optical fiber used to collect the photons rather than the interaction volume of the laser pulses with the sample.

Though PPSNOM has very high lateral spatial resolution, it cannot be used to investigate ultra-fast processes in ultra-thin films, nano-meter to sub-nano-meter thin films, of chromophores on surfaces. The absorption from the excited states in such thin films is too small to be isolated from the huge background noise – fluctuations – present in the probe pulses. Chapter 8 describes the implementation of another technique, *viz*; transient grating spectroscopy , to study the ultra-fast processes in nano-meter and sub-nano-meter layers of chromophores. The lateral spatial resolution of this technique, however, is determined by the spot size of the focus laser.

The experiments presented in Chapter 7 and 8 investigate exciton dynamics in layers of nano-crystals of 3,4,9,10 Perylenetetracarboxylic dianhydride (PTCDA). The samples are prepared by organic molecular beam evaporation in ultra-high vacuum condition that allows control of sample thickness with angstrom precision; such control, which is not possible currently with layers of ChlA or AXT, is necessary to characterize the technique. As the first experiments to study the exciton dynamics on nano-crystals of PTCDA have been successful, the techniques can be easily

adapted to study ultra-fast processes in nano-aggregates of biological chromophores like ChlA and AXT with very high spatial resolution.

Bibliography

[1] Timp, G. Nanotechnology; Springer-Verlag: New York Berlin Heidelberg, 1999.

[2] Taiz, L.; Zieger, E. Plant Physiology; Sinauer Associates Inc.: Sunderland MA, third edition, 2002.

[3] Abrahams, J. P.; Leslie, A. G. W.; Lutter, R.; Walker, J. E. *Nature* **1964,** *370*, 621–628.

[4] Agostiano, A.; Cosma, P.; Trotta, M.; Monsu-Scolaro, L.; Micali, N. *J. Phys. Chem. B* **2002,** *106,* 12820-12829.

[5] Britton, G.; Liaaen-Jensen, S.; Pfander, H. Carotenoids Volume 4: Natural Functions; Birkhäuser Verlag: Basel Boston Berlin, 2008.

[6] Mukamel, S. Principles of Nonlinear Optical Spectroscopy; Oxford University Press: 200 Madison Avenue, New York, 1995.

Part I

Molecular Modeling and Molecular Dynamics Simulations

Chapter 2

Introduction to MD Simulations

MD simulation is a computational technique used to explore the structural and dynamic properties of atomic and molecular systems. In this technique, the state of a system subjected to an analytical potential is propagated in time using the Newton's equation of motion for all the atoms in the system [2]:

$$\frac{d^2\mathbf{r}_i(t)}{dt^2} = m_i^{-1}\mathbf{F}_i = \mathbf{a}_i \tag{2.1}$$

where $\mathbf{r}$ denotes the position, m is the mass, t is the time, $\mathbf{F}$ is the force and $\mathbf{a}$ is the acceleration. The subscript i indexes the atoms with $i \in \{1, ..., N\}$ where N is the number of atoms in the system. The force acting on atom i is obtained from the gradient of the potential energy surface $\phi(\mathbf{r}_1, ..., \mathbf{r}_N)$ defined for the system:

$$\mathbf{F}_i = -\frac{\partial\phi(\mathbf{r}_1, ..., \mathbf{r}_N)}{\partial\mathbf{r}_i}, \tag{2.2}$$

and the potential energy surface is defined by an analytical function called force field. Integration of Equ.2.1 gives

$$\mathbf{v}_i(t) = \mathbf{v}_i(t_0) + \int_{t_0}^{t} \mathbf{a}_i dt \tag{2.3}$$

$$\mathbf{r}_i(t) = \mathbf{r}_i(t_0) + \int_{t_0}^{t} \mathbf{v}_i dt. \tag{2.4}$$

If the initial position $\mathbf{r}_i(t_0)$ and velocity $\mathbf{v}_i(t_0)$ are provided, Equ.(2.3) and (2.4) can be integrated numerically and each successive integration step provides a new configuration of the system. Among the different algorithms used to perform the numercial integration, leap-frog algorithm [3] has been used in the simulations presented in this thesis. In this algorithm the velocities and the coordinates are calculated using the relations,

$$\mathbf{v}_i(t + h/2) = \mathbf{v}_i(t - h/2) + h\mathbf{a}_i(t) \tag{2.5}$$

$$\mathbf{r}_i(t + h) = x(t) + h\mathbf{v}_i(t + h/2). \tag{2.6}$$

The leap-frog method is of 3rd-order accuracy in the time step h [2].

In an MD simulation perfomed using only the Equ.(2.5 and 2.6) the energy of the system, E, is conserved. As N and V (volume of simulation box) are also fixed, the average of any property over the trajectory approximates the measured value of that property for a microcanonical (NVE) ensemble. However, in practice, most of the properties of a system are measured at conditions in which temperature (T) and/or pressure (P) are kept constant instead of E and/or V, respectively. Different techniques have been developed to couple the system to a thermostat and a barostat to keep the temperature and the pressure constant [4]. In this thesis all the simulations have been performed using the Nosé-Hoover thermostat, first proposed by Nosé [5]

and later simplified by Nosé [6] and Hoover [7], to keep the temperature of the system constant.

In the algorithm for Nosé-Hoover thermostat, the Hamiltonian of the system is extended by an addition of a dynamical variable s which is associated with the parameter Q having the dimensions of energy·(time)^2. The dynamical variable s interacts with the system by scaling the velocity [6].

$$\mathbf{v}_i = s\frac{d\mathbf{r}_i}{dt}. \tag{2.7}$$

The equations of motion of the extended system can be written as

$$\frac{d^2\mathbf{r}_i}{dt^2} = m_i^{-1}\mathbf{F}_i - \gamma\frac{d\mathbf{r}_i}{dt} \tag{2.8}$$

and

$$\frac{d\gamma}{dt} = -k_B f\frac{T_0 - T}{Q} \tag{2.9}$$

where k_B is the Boltzmann constant, f is the number of degrees of freedom in the system, T_0 is the reference temperature, T is the instantaneous temperature and γ is the friction parameter defined as follows:

$$\gamma = \frac{1}{s}\frac{ds}{dt}. \tag{2.10}$$

The parameter Q characterizes the strength of coupling to the heat bath and thereby the effective temperature coupling time, which is given by,

$$\tau_T = \left(\frac{Q}{fk_BT_0}\right)^{\frac{1}{2}}. \tag{2.11}$$

Equ.(2.9) can also be written in terms of temperature coupling time, τ_T, as follows:

$$\frac{d\gamma}{dt} = -{\tau_T}^{-2}\left(1 - \frac{T}{T_0}\right). \tag{2.12}$$

The trajectory of the system generated by solving the Equ.(2.8) and (2.12) has been shown to produce a canonical (NVT) ensemble [6].

Like the temperature, the pressure of the system can be kept constant by rescaling the box-vectors of the simulation box. This is equivalent to coupling the pressure of the system to a constant external pressure. Coordinate of particle i in the original and the scaled frame are related by

$$\mathbf{r}_i = \mathbf{b}\ \tilde{\mathbf{r}}_i \tag{2.13}$$

where $\tilde{\mathbf{r}}_i$ is the coordinate in the scaled frame and $\mathbf{b} = (\mathbf{u}_1, \mathbf{u}_2, \mathbf{u}_3)$ is a transformation matrix from the scaled frame to the real frame ($\mathbf{u}_1, \mathbf{u}_2$ and $\mathbf{u}_3$ are the vectors forming the edges of the simulation box) [8]. The transformation matrix obeys the equation of motion

$$\frac{d^2\mathbf{b}'}{dt^2} = V\mathbf{W}^{-1}\mathbf{b}^{-1}(\mathbf{P} - \mathbf{P}_0) \tag{2.14}$$

where V is the volume of the box, $\mathbf{W}$ is the matrix parameter that determines the strength of the coupling, $\mathbf{P}$ is the instantaneous pressure, $\mathbf{P}_0$ is the reference pressure and $\mathbf{b}'$ is the transpose of $\mathbf{b}$. The coupling strength $\mathbf{W}$ determines the pressure time constant τ_P:

$$\left(\mathbf{W}^{-1}\right)_{ij} = \frac{4\pi^2\beta_{ij}}{3\tau_P^2 L} \tag{2.15}$$

where β is the isothermal compressibility and L is the length of the simulation box. The equation of motion of the particles themselves is given by

$$\frac{d^2\mathbf{r}_i}{dt^2} = m_i^{-1}\mathbf{F}_i - \mathbf{M}\frac{d\mathbf{r}_i}{dt} \tag{2.16}$$

with

$$\mathbf{M} = \mathbf{b}'^{-1}\left(\mathbf{b}'\frac{d\mathbf{b}}{dt} + \frac{d\mathbf{b}'}{dt}\mathbf{b}\right)\mathbf{b}^{-1}. \tag{2.17}$$

The idea of rescaled coordinate was first introduced by Andersen and was shown to generate isobaric-isoenthalpic ensemble (NPH) [9]. Using both the temperature and the pressure coupling algorithms in MD simulations generates a trajectory that follows isothermal-isobaric (NPT) ensemble.

2.0.1 Force Field

The phase space explored by a system in an MD simulation is governed by the potential energy surface $\phi(\mathbf{r}_1, ..., \mathbf{r}_N)$. The different physical properties of the simulated system are obtained as ensemble average over the phase space. Though the exact potential energy surface of a system can be conceptualized as the potential derived from the distribution of electrons and nuclei obeying the laws of quantum mechanics, it is computationally impractical to find or design an exact potential using the solution of the time dependent Schrödinger equation for a system with thousands of atoms. Hence, a potential that closely approximates the real system is used. For a molecular system, the potential energy surface is built by incorporating the parameterized important intra and inter-molecular interactions, and the forms of mathematical functions used to describe the interactions together with the parameters used constitute a force field. We have used the OPLS (optimized potentials for liquid simulations) force field [10, 11, 12, 13, 14, 15] in the simulations. The different inter and intra-molecular interactions in the OPLS force field are described by bonded and non-bonded interactions and the forms of the mathematical functions used to described the interactions are given below.

Non-bonded interactions: The non-bonded interactions include the Lennard-Jones (LJ) interaction and the Coulomb interaction, both of which are pair additive

(i.e. they can be written as sum of interaction between a pair of atoms) and centro-symmetric:

$$\phi(\mathbf{r}_1, ..., \mathbf{r}_N) = \sum_{i<j} \phi_{ij}(\mathbf{r}_{ij}) \tag{2.18}$$

$$\mathbf{F}_i = -\sum_j \frac{d\phi_{ij}(r_{ij})}{dr_{ij}} \frac{\mathbf{r}_{ij}}{r_{ij}} = -\mathbf{F}_j \tag{2.19}$$

where $i, j \in \{1, ..., N\}$.

The potential for LJ interaction is given by

$$\phi_{LJ}(\mathbf{r}_{ij}) = 4\epsilon_{ij} \left(\left(\frac{\sigma_{ij}}{r_{ij}} \right)^{12} - \left(\frac{\sigma_{ij}}{r_{ij}} \right)^{6} \right) \tag{2.20}$$

where ϵ_{ij} gives the depth of the potential and σ_{ij} gives the distance at which the potential is 0 as shown in Fig.2.1(a). The attractive part of the potential is due to the dipole induced dipole interactions which arises due to the correlated motion of the electrons between the different atoms, and the repulsive part of the potential signifies the fermionic nature of the electrons, that two electrons cannot be in the same quantum state (here the state would be characterized by position and spin). The

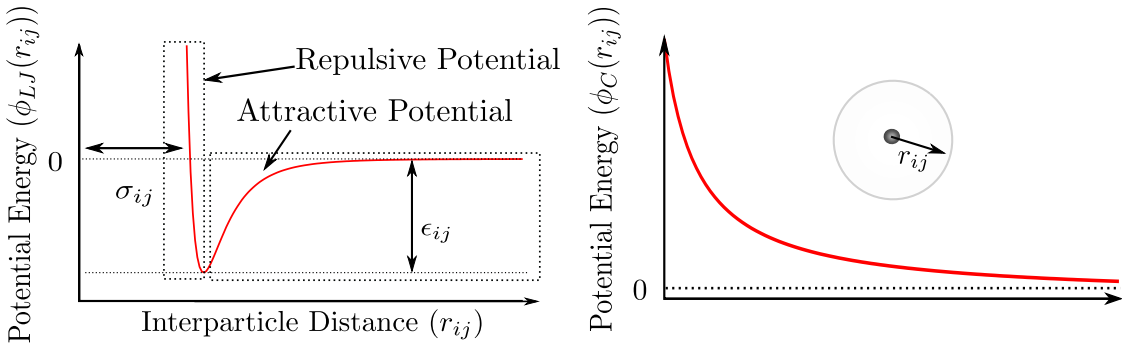

(a) Lennard-Jones potential (b) Coulomb potential

Figure 2.1: Qualitative description of the Lennard-Jones potential (a) and Coulomb potential (b).

Lorentz-Bertelot rules are used to construct the parameter matrix for LJ-parameters:

$$\sigma_{ij} = \frac{1}{2}(\sigma_{ii} + \sigma_{jj}) \tag{2.21}$$

$$\epsilon_{ij} = (\epsilon_{ii}\epsilon_{jj})^{\frac{1}{2}}. \tag{2.22}$$

The potential for Coulomb interaction (Fig.2.1 (b)) between two charged particles is given by

$$\phi_C(r_{ij}) = \frac{1}{4\pi\varepsilon_0}\frac{q_i q_j}{\varepsilon_r r_{ij}}, \tag{2.23}$$

where ε_0 is the vacuum dielectric permittivity, ε_r is the relative dielectric permittivity of the system being simulated and q_i and q_j are the (partial) charges present in the interacting atoms.

Bonded interactions: The bonded interactions include the intra-molecular interactions: *viz*; bonds, angles and dihedrals. The bond vibrations are two body interactions while the bond angle vibrations are three body interactions. The harmonic potential functions, shown in Fig.2.2, given by

$$\phi_b(r_{ij}) = \frac{1}{2}k^b_{ij}(r_{ij} - b_{ij})^2 \tag{2.24}$$

and

$$\phi_a(\theta_{ijk}) = \frac{1}{2}k^\theta_{ijk}(\theta_{ijk} - \theta^0_{ijk})^2, \tag{2.25}$$

where k^b is the bond energy, b_{ij} is the equilibrium bond distance between atoms i and j, k^θ is the energy for the angle and θ^0 is the equilibrium angle between the atoms i, j and k, are used to describe the potential energies for the bonds and and the angles, respectively.

The intra-molecular torsional motions are described by the dihedral angles. The dihedral interaction is a four body interaction. The dihedral angle formed by a set of four bonded atoms i, j, k and l is defined as the angle between the normals of the planes formed by the atoms i, j and k and atoms j, k and l as shown in Fig.2.3. The potential function for the dihedral interactions are given as the four [16] cosine terms

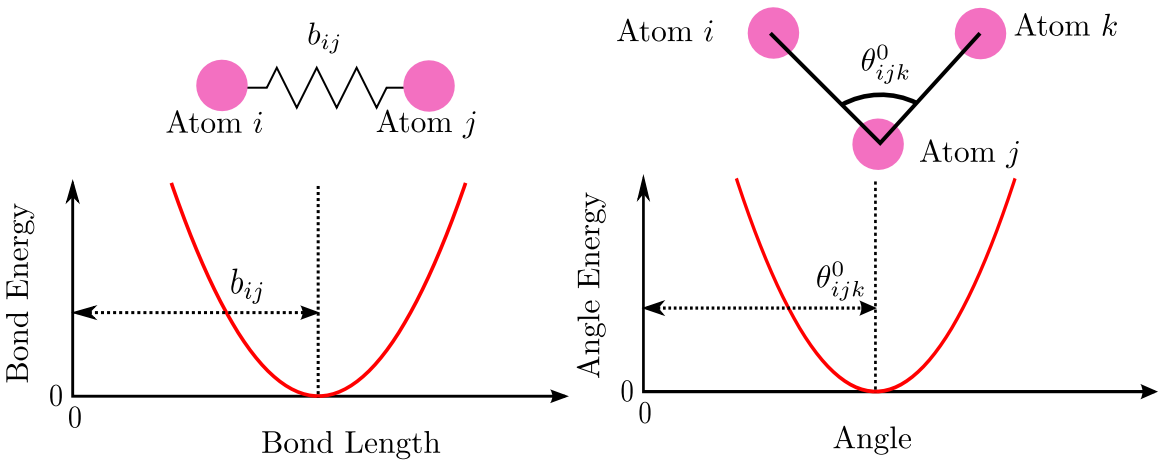

(a) Potential for bond vibrations

(a) Potential for angle vibrations

Figure 2.2: Qualitative description of the harmonic potentials for the bond vibrations (a) and angular distortions (b).

of a Fourier series:

$$\varphi_d(\phi_{ijkl}) = \frac{1}{2}[C_1(1+\cos(\varphi)) + C_2(1-\cos(2\varphi)) + C_3(1+\cos(3\varphi)) + C_4(1-\cos(4\varphi))]. \tag{2.26}$$

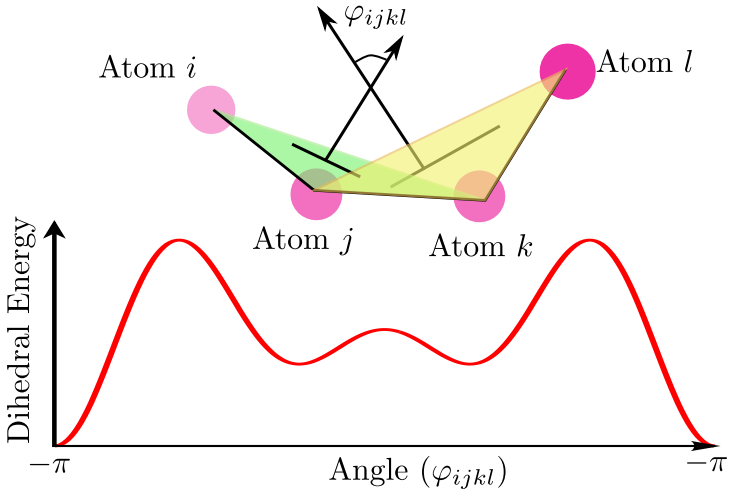

Figure 2.3: Potential for describing rotations of atoms around a bond using dihedral angle.

The theories and formulas used to calculate the different properties of the systems from the simulations are described in the following chapters.

Bibliography

[1] Abrahams, J. P.; Leslie, A. G. W.; Lutter, R.; Walker, J. E. *Nature*, **1964,** *370,* 621–628.

[2] van Gunsteren, W. E.; Berendsen, H. J. C. *Angew. Chem. Int. Ed. Engl.*, **1990,** *29,* 992–1023.

[3] Rapaport, D. The art of molecular dynamics simulation; Cambridge University Press: Cambridge CB2 2RU, UK, 2004.

[4] Leach, A. R. Molecular modelling: Principles and applications; Pearson Education Limited: Harlow, Edinburg Gate, Harlow, 2001.

[5] Nosé, S. *J. Chem. Phys.* **1984,** *81,* 511–519.

[6] Nosé, S. *Mol. Phys.* **1984,** *52,* 255–268.

[7] Hoover, W. G. *Phys. Rev. A* **1985,** *31,* 1695–1697.

[8] Nosé, S.; Klein, M. L. *Mol. Phys.* **1983,** *50,* 1055–1076.

[9] Andersen, H. C. *J. Chem. Phys.* **1980,** *72,* 2384–2393.

[10] Jorgensen, W. L.; Maxwell, D. S.; Tirado-Rives, J. *J. Am. Chem. Soc.* **1996,** *118,* 11225–11236.

[11] Kaminski, G. A.; Friesner, R. A.; Tirado-Rives, J.; Jorgensen, W. L. *J. Phys. Chem. B* **2001,** *105,* 6474–6487.

[12] Jorgensen, W. L.;Tirado-Rives, J. *J. Am. Chem. Soc.* **1998,** *110,* 1657–1666.

[13] Jorgensen, W. L. Encyclopedia of Computational Chemistry; Wiley: New York, 1998.

[14] Jorgensen, W. L.; McDonald, N. A. *J. Mol. Struct. (THEOCHEM)* **1998,** *424,* 145–155.

[15] Jorgensen, W. L.; McDonald, N. A. *J. Phys. Chem. B* **1998,** *102,* 8049–8059.

[16] Jorgensen, W. L.; Tirado-Rives, J. *Proc. Natl. Acad. Sci.* **2005,** *102,* 6665–6670.

Chapter 3

Molecular Dynamics Simulation Study of Chlorophyll a in Different Organic Solvents

Khadga Karki, Danilo Roccatano[1]

Abstract

Herein, we present a new model of chlorophyll a for molecular dynamics simulations based on the OPLS force field. The new model was used to study the structural and dynamic properties of the molecule in three different solvents: water, methanol and benzene. The results of the simulations show that structural and dynamic properties of the chlorin ring are similar in both methanol and benzene. In methanol and water, the magnesium in the chlorin ring binds the oxygen of the solvent molecules with residence times of 2566 ps and 1300 ps, respectively. In both methanol and benzene, the phytol tail shows a worm like chain distribution with a larger persistence length for the molecule in benzene. On the contrary, chlorophyll a in water adopts a more compact structure with the phytol chain folded onto the chlorin ring. This conformation is consistent with the expected conformation of the aggregates of chlorophyll a in aqueous environments. Finally, The rotational time constants obtained with our model from the simulations in methanol (125 ps)

[1]This chapter is reproduced without modifications from the article published in *J. Chem. Theory Comput.,* 2011, **7**, 1131-1140

and benzene (192 ps) are in good agreement with the value extrapolated from the experimental data.

Introduction

Chlorophylls are among the most important molecules in nature [1]. Chl A, one of the chlorophyll molecules, plays a key role in the light-harvesting complex (LHC) , by collecting and funneling light, and as an electron carrier in the photosynthetic reaction centers, by separating charges and transferring electrons across the photosynthetic membrane [2, 3]. These marvelous biological processes are the result of cooperative effects, depending crucially not only on the electronic properties of an individual Chl A molecule but also on the way they are assembled [4]. The structural organization of the chlorophyll molecules in photosynthetic systems is orchestrated by electrostatic and van der Waals, and other nuanced interactions of different functional groups with the surrounding environment. The phytol tail of Chl A is hydrophobic while the magnesium (Mg), being coordinatively unsaturated, attracts nucleophilic polar molecules. In non-polar solvents, like benzene, the coordination of Mg is saturated by the electron donor C=O group of another Chl A molecule leading to the formation of dimers and aggregates. In polar solvents, like methanol, the neucleophilic solvent molecules compete with the C=O group for the coordination with the Mg thereby preventing aggregation. However, in other polar solvent, like water, they form large aggregates [2] because of the intermolecular hydrogen bonding or, smaller aggregates like in mixture of acetonitrile/water because of the hydrophobic effects of the phytol tail [5].

Most of the experimental techniques employed to understand these interactions (for example see the references [6, 7, 8, 9, 10, 11]) do not provide the information

with atomic resolution. Therefore, use of theoretical/computational model can complement these data and provide useful insights for interpretation and comprehension of the interactions. Several computational study, based on molecular dynamics (MD) simulations and quantum mechanics (QM) methods, on the structural and spectroscopic properties of chlorophylls are available in literature [12]. MD simulation studies of chlorophylls, including the ones embedded in the LHCs (see for example [13, 14, 15, 16]), have also been reported. However, to the best of our knowledge, none of these models have been optimized and tested against the properties of isolated molecules in different solvents. In this first paper, we use a new model of Chl A based on the OPLS force field to study the structural and dynamic properties of Chl A in three different solvents: water, methanol and benzene. We have consider methanol (dielectric constant $\epsilon = 33$) and benzene ($\epsilon = 2.28$) because both of them dissolve Chl A, and hence, it is interesting to analyse their effect on the conformation of the molecule in the different environments. On the contrary, simulations in water can be used to test the force field and to get insights into the mechanism of water-mediated aggregation. In the paper, we have focused mainly on investigating the interaction of Chl A with the solvent molecules by comparing our results with the experimental data [17] and recently published QM calculations [18].

The paper is organized as follows. The modelling of the Chl A force field is presented in the Material and Method section. The structural and dynamic properties of the molecule are presented in the Results and Discussion section. In this part, we also report a preliminary study on the aggregation of Chl A. Finally, in the Conclusion, a summary of the study with an outlook on the further applications of the model is presented.

Material and Methods

QM calculations. Chlorophyllide a molecule was used instead of Chl A to calculate the binding energy of water and methanol to the Mg. The starting structure of chlorophyllide a with a water molecule coordinated to the Mg was obtained from the crystal structure of the ethyl derivative of the molecule [19]. The molecule was isolated from water and the ethyl group was substituted by a hydrogen to retain the chlorophyllide a structure. Geometry optimization was done with B3LYP method and 6-31G** basis set in implicit solvation condition using the integral-equation-formalism protocol [20] formulation of the polarizable continuum model (PCM) [21]. A water molecule was placed 0.3 nm above the Mg of the optimized chlorophyllide and the geometry of the complex was optimized again using the same procedure, after which counterpoise correction was used to calculate the binding energy of the water molecule to the Mg. Normal mode analysis were done on the water and the chlorophyllide molecules separately to estimate the thermal corrections used to calculate the Helmholtz free energy. Similar calculations were done in the case of methanol and benzene. The optimized geometries used in the QM calculations are given in the Supporting Information.

QM calculations were also done on Chl A taken from the crystal structure of the LHC of spinach [22] (pdb code: 1RWT) to obtain the optimized structure (shown in Figure 3.1) and the partial charges of the molecule. Geometry optimization was done using the restricted B3LYP method with the 6-31G* basis set and the atomic charges were calculated by fitting the molecular electrostatic potential of the electronic density using the CHELPG procedure [23]. The coordinates of the optimized structure and corresponding partial charges are reported in Table 1 and 2 of the Supporting Information.

All the QM calculations were performed using the program Gaussian 09 [24].

Chl A force field parameters. We used the OPLS-AA [25, 26, 27, 28] force field with additional parameters for partial charges, bond lengths, the angles and

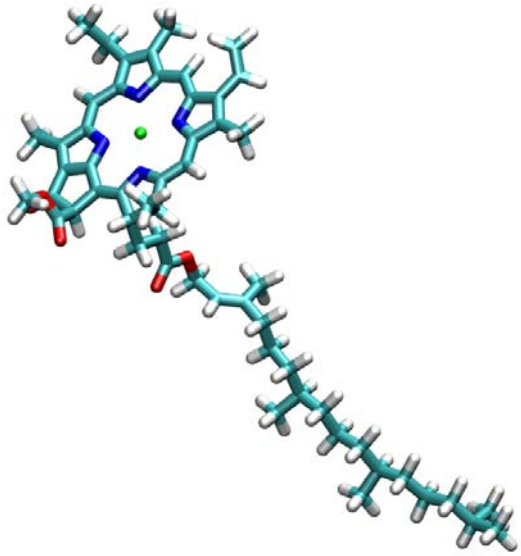

Figure 3.1: Optimized geometry of Chlorophyll a in vacuum.

the dihedral angles based upon our QM calculations. The force constants for the bond angles and the torsional interactions, and the Lennard-Jones parameters were adapted from the OPLS parameters while the partial charges were taken from the QM calculations described above. The full set of parameters are reported in the Supporting Information. OPLS force field based models were also used for methanol [25], water (TIP4P model [29]) and benzene [30].

MD simulations. All MD simulations and analysis were performed using the GROMACS package (version 4.0.7) [31]. The geometry optimized Chl A molecule was immersed in three boxes containing the three different solvents. The simulations in water was done in a 5.34 nm long cubic box containing 4999 water molecules coupled to an external bath at 300 K using the Nose-Hoover [32] thermostat and to a barostat at 1 bar using the Parrinello-Rahman [33, 34] isotropic pressure coupling method as implemented in GROMACS. The coupling time constants for the control of the temperature (τ_T) and the pressure (τ_P) were set to 0.2 and 1.0 ps, respectively, and the compressibility was set to 4.5×10^{-5} bar^{-1}. For the simulations in methanol, a cubic box of length 4.9 nm containing 1685 molecules was used. The coupling time

constants τ_T and τ_P were set to 0.1 and 1.5 ps, respectively, and the compressibility was set to 1.2×10^{-4} bar^{-1}. For the simulations in benzene, a cubic box of length 6.31 nm containing 1685 solvent molecules was used.The coupling time constants τ_T and τ_P were set to 0.2 and 2.5 ps, respectively, and the compressibility was set to 9.5×10^{-5} bar^{-1}. All the solvent molecules within 0.15 nm of any Chl A atom were removed and the systems were energy minimized with the steepest descent method for 5000 steps. The bond lengths were constrained using the SETTLE algorithm [35] for the water molecules and the LINCS algorithm [36] for the other molecules. A 1.0-1.2 nm switched cutoff radius was used for the Lennard-Jones interactions. The PME method [37] was used for the electrostatic interactions with PME order of 4, the Fourier spacing of 0.12 nm and dielectric permittivity of 1. The short-range neighbor list was set to 1.4 nm. All the atoms were given an initial velocity obtained from a Maxwellian distribution at 300 K. A time step of 2 fs was used in the simulations and they were equilibrated by 500 ps of MD runs to allow the relaxation of the solvent molecules. After the equilibration, 50 ns production run was performed for each simulation. Simulations were also performed at constant temperature and volume (NVT) conditions to calculate the potential of mean force (PMF) [38] of the interaction of the solvent molecules with the Mg. Simulations of systems with 10 Chl A molecules in the three solvents were also performed to test the formation of aggregates in the different solvents. The boxes used in the simulations contained 10889, 10828 and 10827 molecules of water, methanol and benzene, respectively.

Cluster analysis of the Chl A conformation. A reliable estimation of the conformational space explored by the simulations is the evaluation of the number of different configurations generated during the trajectory [39]. The cluster analysis of trajectories were performed using the method proposed by Daura et al. [40] on a total of 5000 structures sampled every 10 ps. The clustering algorithm was applied to the heavy atoms of Chl A. The criteria of similarity for two structures was a positional

root mean square deviation with the cut-off set to 0.3 nm. Similar analysis was done to the chlorin ring using the cut-off of 0.02 nm.

Phytol tail analysis. The conformational dynamics of the phytol chain was analysed by calculating the distribution of the beginning-to-end chain length. In the case of methanol and benzene, the distribution was compared with the worm-like-chain (WLC) [41, 42] model given by

$$P(R) = \frac{4\pi N R^2}{l_c^2 A^{\frac{9}{2}}} \exp\left(-\frac{3l_c}{4l_p A}\right) \tag{3.1}$$

where R is the coordinate along the contour of the tail, N is the normalization factor, l_p is the persistence length, l_c is the contour length and A is given by

$$A = 1 - \frac{R^2}{l_c^2}. \tag{3.2}$$

Translational and rotational diffusion. The diffusion coefficient of Chl A was calculated using the Einstein relation [43]:

$$6Dt = \lim_{t\to\infty} \langle |\mathbf{r}_i(t) - \mathbf{r}_i(0)|^2 \rangle \tag{3.3}$$

where $\mathbf{r}_i(t)$ is the coordinate vector of the particle i at time t, $\mathbf{r}_i(0)$ the coordinate vector of the particle i at time t=0.

Besides the translational diffusion, rotational diffusion provides useful information on how a solute interacts with the solvents. The rotational diffusion of the chlorin ring was calculated using the autocorrelation function of the vector normal to the plane of the ring:

$$C = < P_2(\mathbf{n}(0) \cdot \mathbf{n}(t)) > \tag{3.4}$$

where P_2 is the Legendre polynomial of the order 2, **n** is the unit vector pointing out of the plane of the ring and the brackets indicate the average along the trajectory [44]. The plane of the ring was determined using the atoms that show the least fluctuations in the ring.

Rotational relaxation time constants. The correlation function measured in the experiments is usually approximated by [45]

$$C_2(t) = a \exp\left[-(6D_r t)\right] = a \exp(-t/\tau_2) \tag{3.5}$$

where D_r is the rotational diffusion constant, τ_2 is the rotational relaxation time and the subscript 2 refers to the fact that this correlation corresponds to the correlation computed from the simulations using the second order Legendre polynomial (see equation 5.7). Thus, the relaxation time obtained from the simulations is related to the rotational diffusion coefficient by:

$$\tau_2 = \frac{1}{6D_r}. \tag{3.6}$$

Viscosity of the solvents. To compare the rotational relaxation time constants obtained from the simulations with the experimentally determined time constants, the viscosity of the solvents used in the simulations and the experiments have to be taken into account. The viscosities of the solvents used in the simulations were computed from the non-equilibrium MD simulations [46].

In this method, a sinusoidally varying acceleration with the profile given by

$$a_x(z) = A \cos(2\pi z/l_z), \tag{3.7}$$

where A is the amplitude of the acceleration and l_z is the height of the box, was applied in the x direction. In these simulations the length of the boxes in z-direction

were set three times longer than in the other directions. The generated velocity profile due to the acceleration can be written as

$$v_x(z) = V\cos(2\pi z/l_z), \tag{3.8}$$

where V is the amplitude of the generated velocity. The viscosity was then calculated using the relation

$$\eta = \frac{A}{V}\rho(l_z/2\pi)^2 \tag{3.9}$$

where ρ is the density of the solvent.

Different simulations were done varying the amplitude of the acceleration. The viscosity at the equilibrium were determined by interpolation.

Solvation geometry and energetics. The distribution of solvent molecules around the Mg plays important role in solvation and solvent mediated aggregation of Chl A molecules. The pair correlation function, $g_{x,y}(r)$, and the spatial distribution function (SDF) [47] were used to get insight into the local ordering of the solvent molecules. The subscripts x and y in $g_{x,y}(r)$ denote the particle types and r denotes the radial distance between the particles x and y. The number of solvent molecules in the different solvation shells of the Mg was calculated using the running integration number (RIN)

$$n = 4\pi\rho_0 \int_0^R g_{Mg,X}(r)r^2 dr \tag{3.10}$$

where X denotes either O(Oxygen atom) or C (carbon atom) and ρ_0 is the number density of the solvent molecule of which the RIN is calculated.

The anisotropic distribution of the solvent atoms around the chlorin ring was analysed using the SDFs calculated in cartesian coordinate system with the origin of the system fixed to the Mg, two of the vectors defined by the vectors joining Mg to

the nitrogen atoms and a third vector orthogonal to the plane defined by the first two vectors.

The PMFs of the interaction of the solvent molecules with the Mg, as a function of radial distance, were calculated from the pair correlation functions obtained from the NVT simulations using the relation [38]

$$g_{Mg,X}(r) = \exp\left(-\frac{w(r)}{kT}\right) \tag{3.11}$$

where $w(r)$ is the PMF and k is the Boltzmann constant.

Residence time of water and methanol. The lifetime of the contact between the Mg and the solvent molecules in a given solvation shell provides important information about the solvation dynamics. This information can be obtained from MD trajectories in different manners [44]. A common approach is the use of the so-called survival time correlation function [48]:

$$P_\alpha(t) = \sum_{j=1}^{N} \sum_{t'} P_{\alpha,j}(t', t'+t) \tag{3.12}$$

where the probability function, $P_{\alpha,j}(t', t'+t)$ is a binary function that adopts a value of one if the solvent molecule labelled j has been in the referred solvation shell around site a from time t' to time $t+t'$, without escaping in this time interval (or leaving the shell during this interval for a time not longer than a $t*$ interval), and zero otherwise. The value of $P_{\alpha,j}(t, t+t')$ is averaged over time and over all solvents molecules from conformations sampled from the MD simulation. $P_{\alpha,j}(t=0)$ equals the average number of solvent molecules belonging to the solvation shell of the site j (i.e. the coordination number), and $P_{\alpha,j}(t)$ gives the average number of solvent molecules that still remain in the hydration shell after a time t from when they first entered the shell. The relaxation trend of $P_{\alpha,j}(t)$ provides information about the local dynamics of the solvation molecules. The value of $P_{\alpha,j}(t)$ can be approximated to an

exponential function [48]:

$$C_\alpha(t) = A \exp(-t/\tau) \tag{3.13}$$

where τ is the residence time.

Results and Discussion

Structural properties.

The cluster analysis of the chlorin ring done with cutoff of 0.02 nm gave 11,10 and 9 clusters from 5000 sampled structures in water, methanol and benzene, respectively. The cumulative number of the clusters (Figure 3.2(a)) reach a plateau indicating a good sampling of the conformational space. The first 3 clusters account for 99% (80%, 10% and 9%), 99% (79%, 11% and 9%) and 99% (80%, 14% and 5%) of the structures in the three solvents, respectively. The representative structures of the first three clusters are shown in Figure 3.3. The average structure of the ring is planar. The deviations from the planarity involve different collective motions of the atom in the ring. The root mean square fluctuations of the atoms (Figure 3.4) show that atoms on the border of the chlorin ring have larger fluctuations than atoms that connect the aromatic rings or the atoms at the inner part of the rings. Though the pattern of fluctuations in all three solvents is similar, larger fluctuations are observed in water than in methanol or benzene due to the phytol tail which folds back onto the chlorin ring.

The cluster analysis of the complete molecule performed using a larger cutoff of 0.3 nm gave 12, 15 and 14 clusters from 5000 structures sampled from the simulations in water, methanol and benzene, respectively. The cumulative number of the clusters (Figure 3.2(b)) reach a plateau indicating a good sampling of the conformational space. The first 3 clusters account for 94, 71 and 75% of the total sampled structures in water, methanol and benzene, respectively. The large variety of conformations is

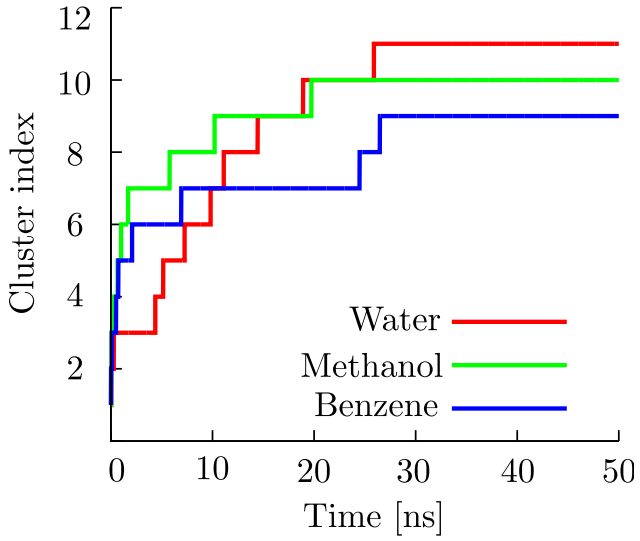

(a) Cumulative Distribution of the Chlorin Conformers

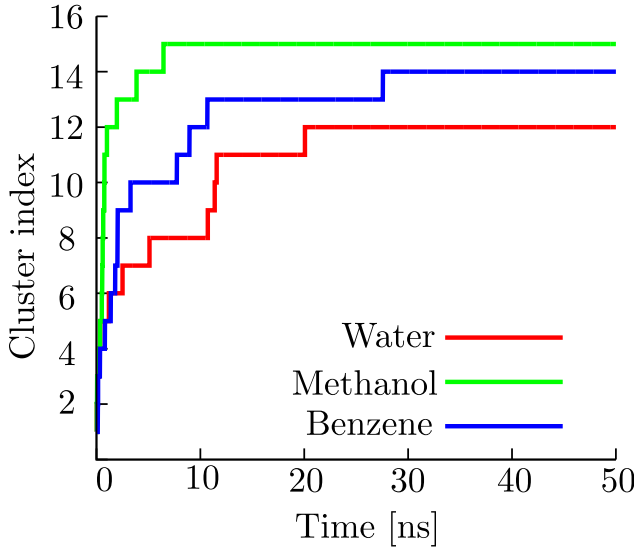

(b) Cumulative Distribution of the Molecule Conformers

Figure 3.2: Cumulative distribution of the number of clusters obtained from the water, methanol and benzene simulations. (a) chlorin ring, (b) all heavy atoms of Chl A.

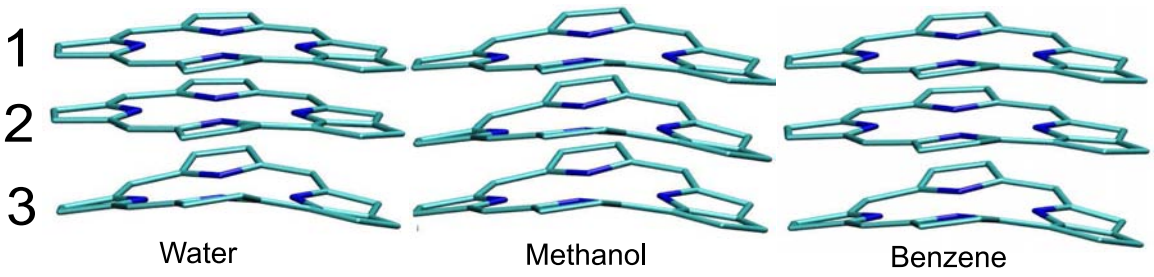

Figure 3.3: Representatives configuration of the three most populated clusters of the chlorin ring.

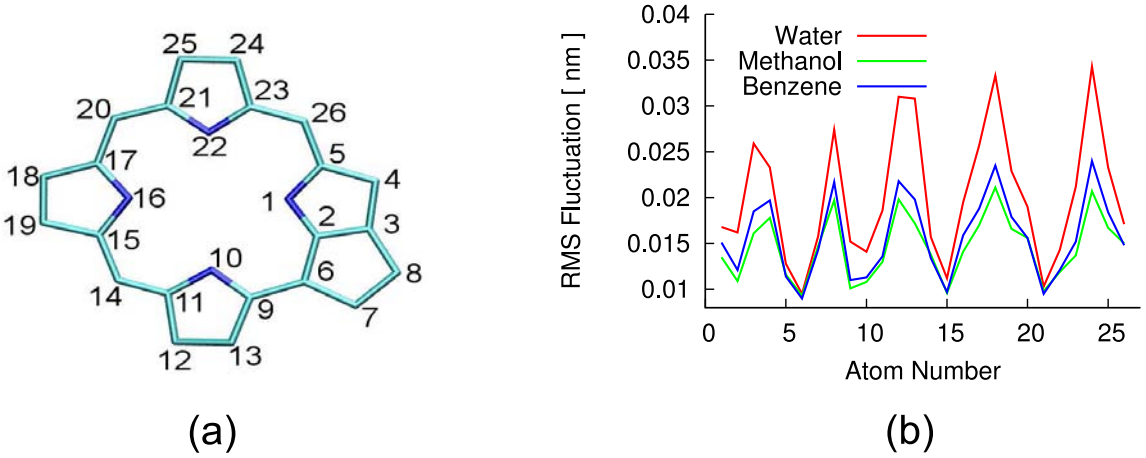

Figure 3.4: Root mean square fluctuations of the atoms of the chlorin ring (b). The numbering of the atoms is shown in (a).

mainly determined by the hydrophobic phytol chain. The smaller number of clusters observed in the simulation in water is due to the folded configuration of the tail, which reduces its mobility. On the contrary, in methanol and benzene, the flexibility of the tail resembles that of a freely floating chain thereby increasing the number of conformations. In Figure 3.5 the beginning-to-end distribution of the phytol chain is reported. In methanol and benzene, the distributions are similar, spanning from 0.36 to 2.33 nm, with the main peak in methanol at 1.57 nm and in benzene at 1.76 nm. The WCL (eq 3.1) model fitted to the distributions give contour and persistence lengths of $l_c = 2.47 \pm 0.02$ nm , $l_p = 0.239 \pm 0.006$ nm and $l_c = 2.575 \pm 0.009$ nm , $l_p = 0.266 \pm 0.003$ nm in methanol and benzene, respectively. The comparison of the persistence lengths indicates that the chain in benzene is stiffer than in methanol.

The distribution in water, which does not fit to the WLC model, is bimodal with the first peak at 0.57 nm corresponding to the tail folded onto the ring and the second peak at 1.4 nm corresponding to a more extended configuration.

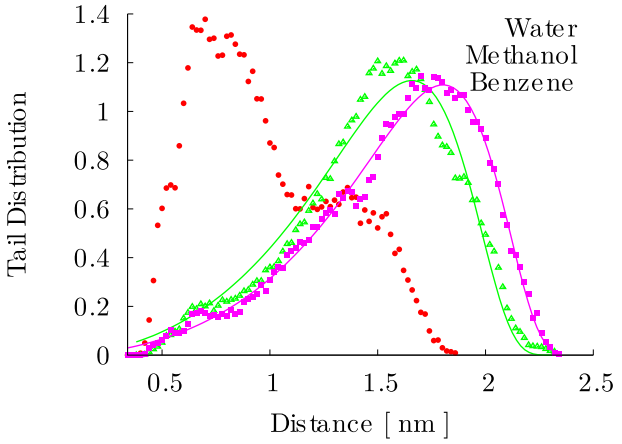

Figure 3.5: The distribution of the beginning-to-end distance of the phytol chain of Chl A in water, methanol and benzene. The symbols indicate the data obtained from the simulations. The distribution in benzene and methanol are fitted to the the worm-like-chain model distribution (solid lines).

Linear and Rotational Diffusion. The rotational diffusion of a molecule in solution can be measured in real time using pump-probe techniques with ultrashort laser pulses. In these experiments, a pump pulse is used to select molecules with a defined orientation, in some cases the molecules can also be aligned with the laser pulses, and the probe pulse is used to interrogate the transient anisotropy in the system induced by the pump pulse. Rotational diffusion makes the system isotropic thereby diminishing the signal from the induced anisotropy. Few of these experiments have been done to measure the rotational dynamics of chlorophyll molecules. In one of the transient grating studies done on zinc methyl 13-desoxopyropheophorbide (Zn DMPPH), an analogous molecule, the measured relaxation time of the rotation of the molecule dissolved in Tetrahydrofuran (THF) was 114 ps [49]. The relaxation time of the rotational dynamics of a molecule is directly proportional to the viscosity, η, of the solvent. Thus, to compare the experimental result with the results from simulations, the viscosities of the different solvents need to be taken into account. The

experimental viscosity of THF is $\eta_T = 4.8 \times 10^{-4}$ Pa.s. The viscosities of the solvent models used in the simulations, determined by non-equilibrium MD simulations [50], are $\eta_w = (5.6 \pm 0.7) \times 10^{-4}$ Pa.s, $\eta_m = (5.4 \pm 0.7) \times 10^{-4}$ Pa.s, and $\eta_b = (7.4 \pm 0.9) \times 10^{-4}$ Pa.s for water, methanol and benzene, respectively.

In the approximation that the geometry of the molecule is unchanged in different solvents, the viscosities and the rotational time constants τ follow the relation:

$$\frac{\tau_x}{\tau_y} = \frac{\eta_x}{\eta_y} \tag{3.14}$$

where subscripts x and y represent two different solvents. The expected rotational time constant of Zn DMPPH in water, methanol and benzene models estimated using eq 3.14 are $\tau_{2,w} = 135 \pm 15$ ps, $\tau_{2,m} = 128 \pm 14$ ps and $\tau_{2,b} = 176 \pm 30$ ps, respectively. Subscripts w, m and b refer to the solvents water, methanol and benzene, respectively. The time constants of the exponential functions used to fit the second order correlation functions obtained from the simulations (Figure 3.6) are $\tau_w = 99$ ps, $\tau_m = 125$ ps and $\tau_b = 192$ ps. The rotational diffusion time constants obtained from simulations in methanol and benzene are close to the respective estimated rotational time constants. In water, the time constant obtained from the simulation is slightly lower than the corresponding estimate from the experiment, which could be due to the influence of the solvent in the geometry of the molecule. In water, as noted previously, the tail folds back to the chlorin ring, thereby decreasing the cross-section of the molecule as well as the moment of inertia and hence the faster rotational motion.

The rotational diffusion coefficients computed using eq 3.6 are 1.68 rad^2/ns, 1.33 rad^2/ns and 0.87 rad^2/ns in water, methanol and benzene, respectively. To the best of our knowledge, direct experimental determination of rotational diffusion coefficients of Chl A or related molecules are not yet done. However, the values obtained from the simulations can be considered quite reliable as the relaxation times obtained from

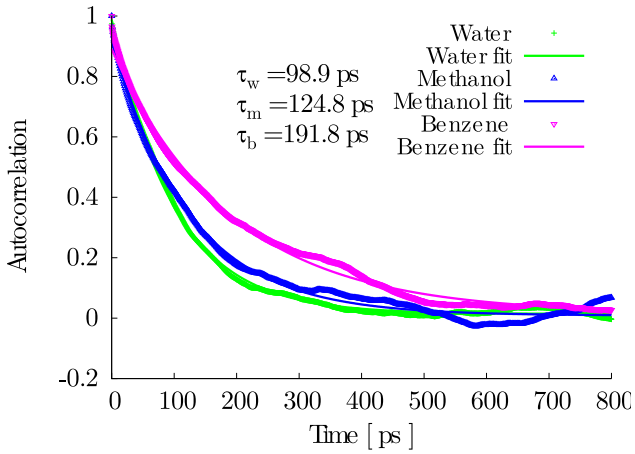

Figure 3.6: Correlation functions using second order Legendre polynomial for the rotational diffusion of Chl A in water, methanol and benzene. The correlation functions are fitted with exponential decay curves. The time constants for the decay, τ, are reported in the figure.

the simulations follow are close to those estimated from the available experimental data.

Finally, the linear diffusion constants estimated using eq 5.5 are 0.47×10^{-5} cm^{2}s^{-1}, 0.52×10^{-5} cm^{2}s^{-1}, and 0.40×10^{-5} cm^{2}s^{-1} in water, methanol and benzene, respectively.

Chl A solvation. The coordination unsaturation of the Mg can be satisfied by nucleophilic ligands [2]. The ligands can form both the Chl.L_1 and Chl.L_2 complexes, where Chl.L_1 is the complex formed with a ligand occupying one of the axial positions while Chl.L_2 is the complex formed with two ligands occupying the axial positions on both the sides of the chlorin plane. The coordination of the methanol and water molecules to the Mg can be studied with the pair correlation function $g_{Mg,O}$. In Figure 3.7, the $g_{Mg,O}$'s of both the solvents are shown. They have the first peak located at 0.21 nm. The narrow width of the peaks indicate that the oxygen atom is strongly bound to the Mg in both the solvents. The average number of oxygen atoms within the first solvation shell (up to 0.28 nm) are 1.02 and 1.01 for water and methanol, respectively (see Figure 3.7). This indicates that the Mg is predominantly

penta-coordinated. The average number of oxygen atoms within the second solvation shell (up to 0.50 nm in water and 0.52 nm in methanol) are 4.33 and 2.19 in water and methanol, respectively.

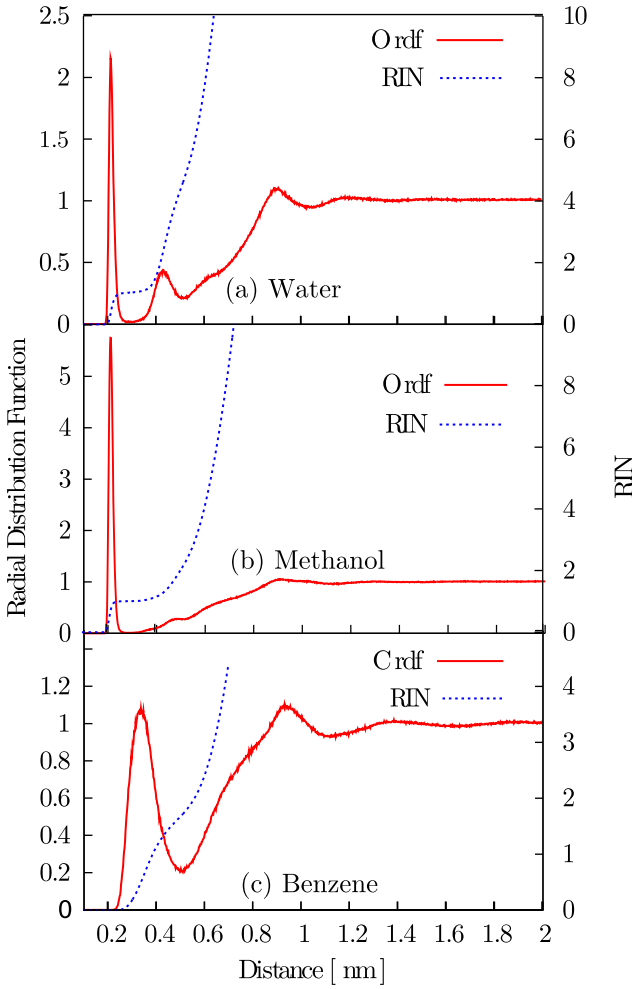

Figure 3.7: The radial distribution functions and the running integration numbers of the oxygen atoms of water and methanol and the carbon atoms of benzene around the Mg atom.

In Figures 3.8(a) and 3.8(b), the SDF of oxygen and hydrogen atoms of water and methanol around the chlorin ring are shown. The average structures of the chlorin ring shown in the figures are slightly distorted with the Mg atom displaced out of the plane of the ring. The distortion is opposite to the side with the ester C=O group. The distances between the Mg and the plane of the chlorin ring defined by atoms 1, 10 and 22 (Fig. 3.4(a)) are 0.023 nm and 0.027 nm in water and methanol,

respectively. The B3LYP/6-31G** optimized structures of water-chlorophyllide and methanol-chlorophyllide complexes (Figures 3.10(a) and (b), respectively) also show distortion of the chlorin ring. The distances between the Mg atom and the plane of the chlorin ring, as defined previously, are 0.040 nm and 0.037 nm in the water-chlorophyllide and the methanol-chlorophyllide complexes, respectively. The displacement observed in the optimized geometry of water-chlorophyllide complex is similar to the displacement of 0.039 nm observed in the crystal structure of ethyl-chlorophyllide a dihydrate [19]. The displacement observed in the MD simulations is less than the displacement observed in the chlorophyllide crystal structure and close to the range of displacement of 0.011-0.025 nm observed in the chlorophyll molecules of the spinach major LHC crystal structure (1RWT).

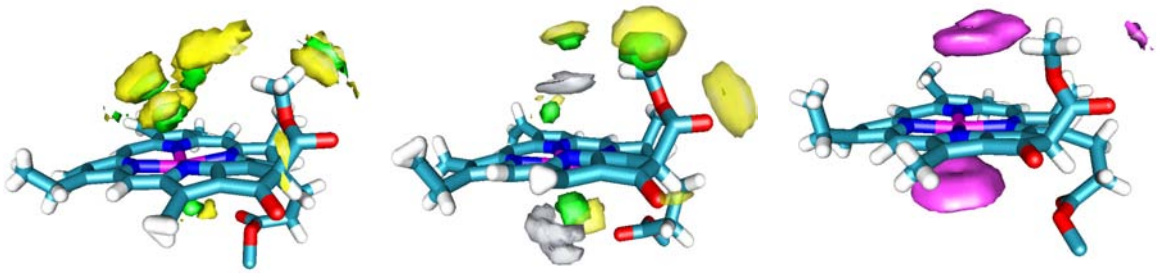

(a) Water (b) Methanol (c) Benzene

Figure 3.8: Spatial distribution function of oxygen and hydrogen atoms of water molecules (a), methanol molecules (b) and carbon atoms of benzene molecules (c) around the chlorin ring . Color coding for the contour surfaces: green for O, yellow for H in hydroxyl group, grey for H in methyl group and magenta for C in the benzene. The contour values of the iso-surfaces are 10 for both the hydrogens and oxygens in water, 22, 9 and 15 for methyl-hydrogens, hydroxyl hydrogens and oxygens, respectively, in methanol, and 12 for the carbons in benzene.

The SDF of the oxygen atoms of water (Figure 3.8(a)) shows two densities on the axial position on both the sides of the chlorin ring. In the same figure, the SDF of the hydrogen atoms of water shows that the hydrogens of the water molecules bound to the Mg point outward from the ring which is consistent with the B3LYP/6-31G** optimized structure of water-chlorophyllide complex as shown in Figure 3.10(a). The

distance between Mg and oxygen in the optimized structure is 0.211 nm which agrees with the position of the first peak of the $g_{Mg,O}$ from the simulation. In addition, the Mg-O distances in both the QM optimized geometry and the SDF are similar to the distance of 0.204 nm observed in the crystal structure of ethyl chlorophyllide a dihydrate [19]. The SDF of the oxygen atoms shows other two high density regions above the first on the upper side of the ring. The arrangement of these two regions indicates presence of hydrogen bonds between the water molecules in the two regions and the water molecules coordinated to the Mg. Aggregation of chlorophylls in aqueous medium has been attributed to the hydrogen bonding between the Mg-bound water molecule of one chlorophyll and the keto C=O group of another chlorophyll molecule [51, 52]. The presence of water molecules chained with hydrogen bonds to the Mg coordinated water molecule is supported by the crystal structure of ethyl chlorophyllide a.$2H_2O$ as proposed by Strouse et al. [19]. In this crystal structure, the Mg coordinated water molecule is simultaneously hydrogen bonded to keto C=O group of another ethyl chlorophyllide a and to the oxygen of the second water molecule. The second water molecule is then hydrogen bonded to the ester C=O of the first ethyl chlorophyllide and to the propionic ester C=O of a third ethyl chlorophyllide (see the cited paper of Strouse et al. [19]). Coordination of water molecule to the Mg also plays central role in proposed models of the photoactive chlorophyll special pair [52]; the SDF of the water molecules around the chlorin ring obtained from our simulations is consistent with these hypotheses.

The SDF of the oxygen of methanol (Figure 3.8(b)) shows three regions of high density of oxygen atoms: two above and one below the chlorin ring. The high densities on the axis above and below the Mg are due to the oxygen atoms bound to the Mg, the other high density on the side of the density above the Mg is due to methanol molecules hydrogen bonded to the former. The SDF of the hydroxyl hydrogens shows a high density in the vicinity of the ester and the keto oxygens indicating hydrogen

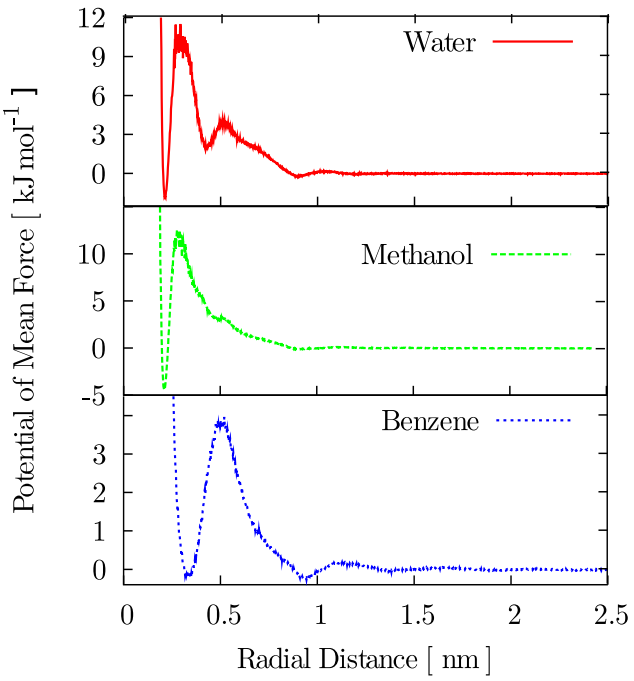

Figure 3.9: The potential of the mean force of the solvent molecules derived from the radial distribution functions.

bonding of methanol molecules with these groups. How the arrangement of the two methanol molecules affect the solubility/aggregation of chlorophylls is not clear from the simulations.

The pair correlation function $g_{Mg,C}$ of carbon atoms of benzene molecules around the Mg has the first peak at 0.35 nm (Figure 3.7(c)) which is similar to the distance of 0.38 nm between Mg and benzene in the B3LYP/6-31G** optimized chlorophyllide-benzene complex (Figure 3.10(c)). The number of solvent molecules in the first solvation shell (up to 0.5 nm radial distance) is 1.65. As in the case of water and methanol, the Mg is slightly displaced out of the plane of the ring by about 0.013 nm. The displacement of the Mg observed in the B3LYP/6-31G** optimized chlorophyllide-benzene (Figure 3.10 (c)) complex is 0.006 nm. The oblate doughnut shape densities, which slightly are at an angle to the chlorin plane in the SDF of benzene (see Figure 3.8c), agree well with the position of the benzene molecule in the QM optimized structure of chlorophyllide-benzene complex (see Figure3.10(c)).

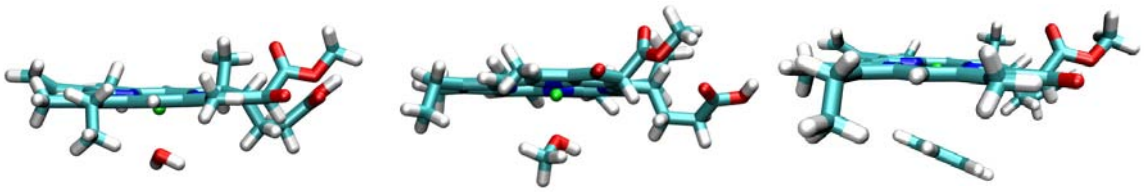

(a) (b) (c)

Figure 3.10: The optimized geometry of chlorophyllide-water (a), chlorophyllide-methanol (b) and chlorophyllide-benzene (c) complexes. The oxygen atom of water and methanol is bound to the Mg atom of the chlorin ring. The distance between the oxygen and the Mg is 0.21 nm (a,b). The distance of the Mg from the center of the benzene ring is 0.38 nm. The plane of the benzene ring is slightly tilted at an angle to the plane of the chlorin ring (c).

Binding energy and Helmholtz free energies of solvation of the Mg atom. The binding energies of water and methanol molecules in the chlorophyllide A.L_1 calculated using counterpoise corrected B3LYP/6-31G** method are -43.73 kJ/mol and -45.34 kJ/mol, respectively. QM calculations done by Fredj et. al. [18] on a similar model of Chl A gave a similar value of -51.46 kJ/mol, for the binding of water to the Mg. The Helmholtz free energy of binding (ΔF_b) obtained from our calculations are -7.95 kJ/mol and -7.96 kJ/mol in water and methanol, respectively. From the experimentally determined equilibration constant ($K = 56\ l\ mol^{-1}$) of dimers and methanol coordinated Chl A molecules in CCl_4 [17], a ΔF_b value of -10.04 kJ/mol can be estimated. As we expect that the ΔF_b for the binding of methanol to chlorophyllide a is similar to the one with Chl A, the QM calculated value is in good agreement with the experimental data.

The ΔF_b calculated from the MD simulations using the PMF (Figure 3.9) of the interaction between the methanol molecules and the Mg is -4.45 kJ/mol, which is lower than the value estimated from the experiment. However, it has been shown from QM calculations that the dielectric constant of the medium decreases the binding of the ligands. [18] Thus taking into account the difference in the dielectric constants of the

solvents in the experiment (CCl_4,$\epsilon = 2.24$) and the simulations (pure methanol, $\epsilon \approx$ 20 [53]), the lower values of the ΔF_b in the simulation can be considered reasonable.

The ΔF_b of water and benzene to the Mg obtained from MD simulations are -1.92 kJ/mol and -0.24 kJ/mo. Though experimental values are not available for these solvents, the values obtained from our simulation seem reasonable.

Chl A Aggregation. The structure of dimers and multimers obtained from the simulation of 10 Chl A molecules in the water and the benzene are shown in the Figures 3.11 and 3.12, respectively. No stable dimers or multimer was observed in the simulation in methanol. In the simulation in water a stable dimer and a pentamer were observed. The spherical shape of the pentamer with the chlorin rings pointing outwards is similar to the structure of the large aggregates of Chl A in water rich regions as proposed by Agostiano et. al. [5], wherein the self-aggregation is attributed to the hydrophobic interactions of the phytol tail. The dimer obtained from the water simulation (Figure 3.11 (a)) has a water molecule sandwiched between the two Chl A molecules while the pentamer in water (Figure 3.11 (b)) has two water molecules sandwiched between the Chl A molecules. It is possible that that the water molecules trapped in the aggregates also contribute to the aggregation by electrostatic and hydrogen bonding interactions.

The dimers observed in the simulation in benzene (Figure 3.12) have different geometries. In the first dimer (Figure 3.12(a)), the two molecules are bridged by the binding of the ester C=O group of the first molecule to the Mg of the second molecule. In the second dimer (Figure 3.12(b)), the two molecules are bridged by the binding of the ester C=O group of one molecule to the other. Though other dimeric and multimeric conformations are also expected to form [54], they probably were not observed in our simulations because of the limited size of the system and the length of the simulations.

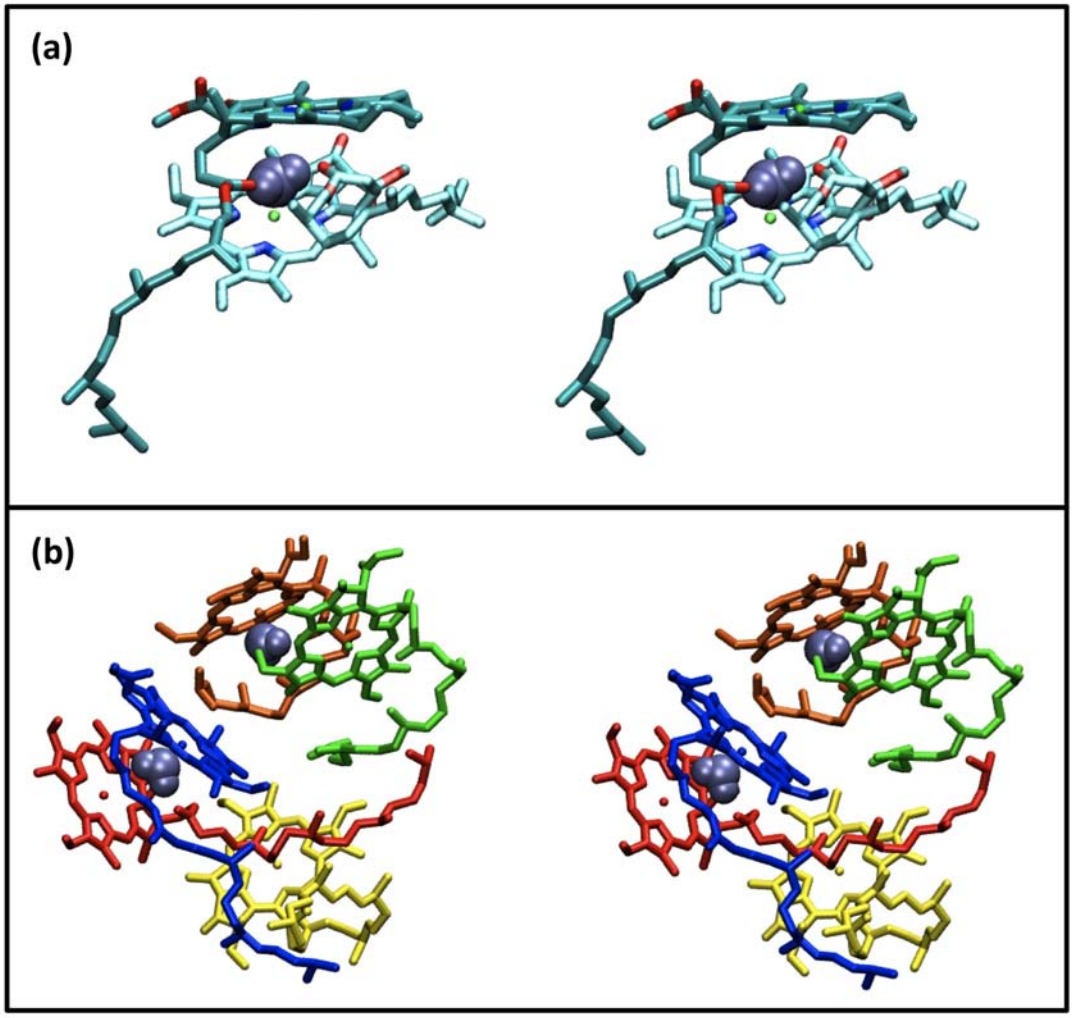

Figure 3.11: Stereo view of the structures of the dimer (a) and the pentamer (b) of Chl A formed in the water.

Residence time of water and methanol. As reported by Ballschimeter and Katz [51], a dynamic equilibrium exists between the 2Chl A.L complex and the isolated species for nucleophilic ligand L in non-polar solvents. The coordination of the ligand to the Mg is primarily responsible for the formation of Chl A.L complex. The time scales of the formation of the complex and its disaggregation can be calculated from the residence time of methanol and water coordinated to the Mg.

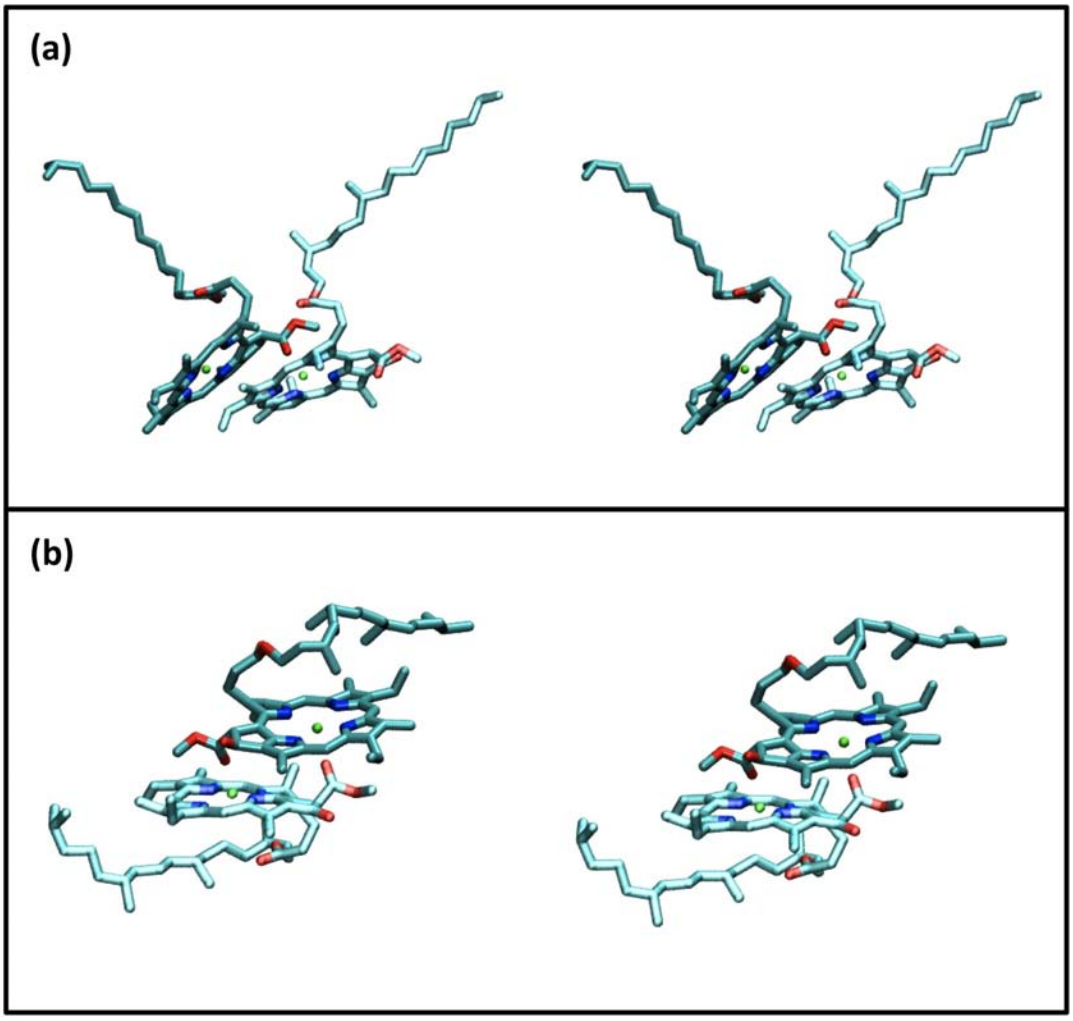

Figure 3.12: Stereo view of the structures of the dimers of Chl A in the benzene.

In the simulation in methanol, the solvent molecules in close contact to the Mg have residence times spanning from picoseconds up to few nanoseconds. The distribution of the short residence time is shown in Figure 1(a) of the Supporting Information. The exponential decay approximating the distribution gives a time constant of 5 ps. The distribution of the residence time longer than 100 ps is shown in the panel b of the same figure. The exponential function fitted to the distribution gives a time constant of 2566 ps.

A similar multi exponential distribution is observed for the residence times of water molecule in the chlorin ring (see Figure 2 in the Supplementary Information). Interestingly, in this case, intermediate time scales (hundreds of ps) are also observed. The three time scales obtained from fitting exponential functions are 10 ps, 200 ps and 1300 ps, respectively. The shortest and the longest time scales are associated with events involving a fast solvent exchange in the first shell of the Mg caused by molecular collision or conformational change of the chlorin ring. Interaction of other water molecules hydrogen bonded to the Mg coordinated molecule may be responsible for the presence of the intermediate residence time. However, as there are few data points available for the distributions of the residence times, the calculated decay constants can only be considered qualitatively.

Conclusions

In this paper, we have presented a new model of chlorophyll a for MD simulations based on the all-atom OPLS force field. The model was tested by studying structural and dynamic properties of the molecule in three different solvents: water, methanol and benzene. The rotational time constants obtained with our model from the simulations in methanol (125 ps) and benzene (192 ps) are in good agreement with the value extrapolated from experimental data.

The distribution of the phytol tail length in methanol and in benzene is consistent with WLC distribution. The stark differences in the configuration of the tail in different solvents raise interesting questions about the effect of the protein and lipid environment on the distribution of the Chl a in the photosynthetic complex of the chloroplasts. Furthermore, the Mg-coordinating water and methanol molecules have geometries comparable to the available experimental values. In particular, the spatial distribution of the oxygens and hydrogens of water and methanol molecules support

the proposed interaction of these solvent molecules with different functional groups of Chl A. The results of the simulations show that structural and dynamic properties of the chlorin ring are similar in both methanol and benzene. In methanol and water, the Mg atom in the chlorin ring bind the oxygen of the solvent molecules with residence times of 2566 ps and 1300 ps, respectively.

The overall good quality of the model makes it suitable for the study of interesting systems like self assembled micelles [55], mimicking the reaction center of light harvesting complex and interactions of the chlorophylls with inorganic surfaces.

Acknowledgements

This study was performed using the computational resources of the CLAMV (Computer Laboratories for Animation, Modeling and Visualization) at Jacobs University Bremen. This work was performed within the graduate program "Nanomolecular Science" and was financially supported by "Research Center for Functional Materials and Nanomolecular Science (NANOFUN)".

Bibliography

[1] Katz, J. J.; Oettmeier, W.; Norris, J. R. *Phil. Trans. R. Soc. Lond. B.* **1976,** *273,* 227-253.

[2] Katz, J. J. *Naturwissenschaften* **1973,** *60,* 32-39.

[3] Agostiano, A.; Cosma, P.; Trotta, M.; Monsu-Scolaro, L.; Micali, N. *J. Phys. Chem. B* **2002,** *106,* 12820-12829.

[4] Emerson, R.; Arnold, W. *J. Gen. Physiol.* **1931-1932,** *16,* 191-205.

[5] Agostiano, A.; Monica, M. D.; Palazzo, G.; Trotta, M. *Biophys. Chem.* **1993,** *47,* 193-202.

[6] Jiao, J.; Thamyongkit, P.; Schmidt, I.; Lindsey, J. S.; Bocian, D. F. *J. Phys. Chem. C* **2007,** *111,* 12693-12704.

[7] Anariba, F.; Viswanathan, U.; Bocian, D. F.; McCreery, R. L. *Anal. Chem.* **2006,** *78,* 3104-3112.

[8] Thamyongkit, P.; Yu, L.; Padmaja, K.; Jiao, J.; Bocian, D. F.; Lindsey, J. S. *J. Org. Chem.* **2006,** *71,* 1156-1171.

[9] Jiao, J.; Anariba, F.; Tiznado, H.; Schmidt, I.; Lindsey, J. S.; Zaera, F.; Bocian, D. F. *J. Am. Chem. Soc.* **2006,** *128,* 6965-6974.

[10] Zanoni, R.; Aurora, A.; Cattaruzza, F.; Decker, F.; Fastiggi, P.; Menichetti, V.; Tagliatesta, P.; Capodilupo, A.-L.; Lembo, A. *Mat. Sci. Eng. C* **2007,** *27,* 1351-1354.

[11] Simkiene, I.; Sabataityte, J.; Babonas, G. J.; Reza, A.; Beinoras, J. *Mat. Sci. Eng. C* **2006,** *26,* 1007-1011.

[12] Linnanto, J.; Korppi-Tommola, J. *Phys. Chem. Chem. Phys.* **2006,** *8,* 663-687.

[13] Damjanovic, A.; Kosztin, I.; Kleinekathofer, U.; Schulten, K. *Phys. Rev. E* **2002,** *65,* 1-24.

[14] Olbrich, C.; Kleinekathöfer, U. *J. Phys. Chem. B* **2010,** *114,* 12427-12437.

[15] Spezia, R.; Aschiy, M.; Nola, A. D.; Valentin, M. D.; Carbonera, D.; Amadei, A. *Biophys. J.* **2003,** *84,* 2805-2813.

[16] Palenćár, P.; Vácha, F.; Kuťz, M. *Photosynthetica* **2005,** *43,* 417-420.

[17] Katz, J. J.; Strain, H. H.; Leussing, D. L.; Dougherty, R. C. *J. Am. Chem. Soc.* **1968,** *90,* 784-791.

[18] Fredj, A. B.; Ruiz-López, M. F. *J. Phys. Chem. B* **2010,** *114,* 681-687.

[19] Chow, H.-C.; Serlin, R.; Strouse, C. E. *J. Am. Chem. Soc.* **1975,** *97,* 7230-7237.

[20] Cancés, E.; Mennucci, B.; Tomasi, J. *J. Chem. Phys.* **1997,** *107,* 3032-41.

[21] Miertuš, S.; Scrocco, E.; Tomasi, J. *Chem. Phys.* **1981,** *55,* 117-129.

[22] Liu, Z.; Yan, H.; Wang, K.; Kuang, T.; Zhang, J.; Gui, L.; An, X.; Chang, W. *Nature* **2004,** *428,* 287-292.

[23] Breneman, C. M.; Wiberg, K. B. *J. Comp. Chem.* **1990,** *11,* 361-397.

[24] Frisch, M. J.; Trucks, G. W.; Schlegel, H. B.; Scuseria, G. E.; Robb, M. A.; Cheeseman, J. R.; Scalmani, G.; Barone, V.; Mennucci, B.; Petersson, G. A.; Nakatsuji, H.; Caricato, M.; Li, X.; Hratchian, H. P.; Izmaylov, A. F.; Bloino, J.; Zheng, G.; Sonnenberg, J. L.; Hada, M.; Ehara, M.; Toyota, K.; Fukuda, R.; Hasegawa, J.; Ishida, M.; Nakajima, T.; Honda, Y.; Kitao, O.; Nakai, H.; Vreven, T.; Montgomery, Jr., J. A.; Peralta, J. E.; Ogliaro, F.; Bearpark, M.; Heyd, J. J.; Brothers, E.; Kudin, K. N.; Staroverov, V. N.; Kobayashi, R.; Normand, J.; Raghavachari, K.; Rendell, A.; Burant, J. C.; Iyengar, S. S.; Tomasi, J.; Cossi, M.; Rega, N.; Millam, J. M.; Klene, M.; Knox, J. E.; Cross, J. B.; Bakken, V.; Adamo, C.; Jaramillo, J.; Gomperts, R.; Stratmann, R. E.; Yazyev, O.; Austin, A. J.; Cammi, R.; Pomelli, C.; Ochterski, J. W.; Martin, R. L.; Morokuma, K.; Zakrzewski, V. G.; Voth, G. A.; Salvador, P.; Dannenberg, J. J.; Dapprich, S.; Daniels, A. D.; Farkas, .; Foresman, J. B.; Ortiz, J. V.; Cioslowski, J.; Fox, D. J. "Gaussian 09 Revision A.1", Gaussian Inc. Wallingford CT 2009.

[25] Jorgensen, W. L.; Maxwell, D. S.; Tiraldo-Rives, J. *J. Am. Chem. Soc.* **1996,** *118,* 11225-11236.

[26] Jorgensen, W. L. Encyclopedia of Computational Chemistry. In , Vol. 3; Wiley: New York, 1998; Chapter OPLS, force field, pages 1986–1989.

[27] Jorgensen, W. L.; McDonald, N. A. *J. Mol. Struct. (THEOCHEM)* **1998,** *424,* 145-155.

[28] Jorgensen, W. L.; McDonald, N. A. *J. Phys. Chem. B* **1998,** *102,* 8049-8059.

[29] Jorgensen, W. L.; Chandrasekhar, J.; Madura, J. D.; Impey, R. W.; Klein, M. L. *J. Chem. Phys.* **1983,** *79,* 926-935.

[30] Milano, G.; Mller-Plathe, F. *J. Phys. Chem. B* **2004,** *108,* 7415 -7423.

[31] Hess, B.; Kutzner, C.; van der Spoel, D.; Lindahl, E. *J. Chem. Theory Comput.* **2008,** *4,* 435-447.

[32] Hoover, W. G. *Phys. Rev. A* **1985,** *31,* 1695-1697.

[33] Parrinello, M.; Rahman, A. *J. Apply. Phys.* **1981,** *52,* 7182-7190.

[34] Nosé, S.; Klein, M. L. *Mol. Phys.* **1983,** *50,* 1055-1076.

[35] Miyamoto, S.; Kollman, P. A. *J. Comp. Chem.* **1992,** *13,* 952-962.

[36] Hess, B.; Bekker, H.; Berendsen, H. J. C.; Fraaije, J. G. E. M. *J. Comp. Chem.* **1997,** *18,* 1463-1472.

[37] Essmann, U.; Perera, L.; Berkowitz, M. L.; Darden, T.; Lee, H.; Pedersen, L. G. *J. Chem. Phys.* **1995,** *103,* 8577-8592.

[38] Chandler, D. Introduction to modern statistical mechanics; Oxford University Press: University of California, Berkeley, 1987; Chapter 7, page 201.

[39] Smith, L. J.; Daura, X.; van Gunsteren, W. *Proteins: Struct., Funct., and Genet.* **2002,** *48,* 487-496.

[40] Daura, X.; Jaun, B.; Seebach, D.; van Gunsteren, W. F.; Mark, A. E. *J. Mol. Biol.* **1998,** *280,* 925–932.

[41] Thirumalai, D.; Ha, B. Theoretical and Mathematical Models in Polymer Research. In ; Academic Press: San Diego, 1998; Chapter Statistical Mechanics of Semiflexible Chains: A Meanfield Variational Approach, pages 1–35.

[42] Becker, N. B.; Rosa, A.; Everaers, R. *Eur. Phys. J. E* **2010,** *32,* 53-69.

[43] Allen, M. P.; Tildesley, D. J. Computer Simulations of Liquies. ; Oxford Science Publications: Oxford, 1987.

[44] Roccatano, D. *Curr. Protein Pept. Sc.* **2008,** *9,* 407-426.

[45] Jas, G. S.; Wang, Y.; Pauls, S. W.; Johnson, C. K.; Kuczera, K. *J. Chem. Phys.* **1997,** *107,* 8800-8812.

[46] Hess, B. *J. Chem. Phys.* **2002,** *116,* 209-217.

[47] Kulasik, P. G.; Laaksonen, A.; Svishchev, I. M. Molecular dynamics: from classical to quantum methods; Elsevier Science B.V.: Sara Burgerhartstraat 25, Amsterdam, 1999.

[48] Impey, R. W.; Madden, P. A.; McDonald, I. R. *J. Phys. Chem.* **1983,** *87,* 5071-5083.

[49] Wiederrecht, G. P.; Svec, W. A.; Niemczyk, M. P.; Wasielewski, M. R. *J. Phys. Chem.* **1995,** *99,* 8918-8926.

[50] Van Der Spoel, D.; Lindahl, E.; Hess, B.; Groenhof, G.; Mark, A. E.; Berendsen, H. J. *J Comput Chem* **2005,** *26,* 1701–1718.

[51] Ballschmiter, K.; Katz, J. J. *J. Am. Chem. Soc.* **1969,** *91,* 2661-2677.

[52] Katz, J. J.; Norris, J. R.; Shipman, L. L.; Thurnauer, M. C. *Ann. Rev. Biophys. Bioeng.* **1978,** *7,* 393-434.

[53] Richardi, J.; Millot, C.; Fries, P. H. *J. Chem. Phys.* **1999,** *110,* 1138-1147.

[54] Oba, T.; Furukawa, H.; Wang, Z.-Y.; Nozawa, T.; Mimuro, M.; Tamiaki, H.; Watanabe, T. *J. Phys. Chem. B* **1998,** *102,* 7882-7889.

[55] Worcester, D. L.; Michalski, T. J.; Katz, J. J. *Proc. Natl. Acad. Sci.* **1986,** *83,* 3791-3795.

Available Supporting Information

The coordinates of the QM optimized structures of Chl A, chlorophyllide A, complexes of chlorophyllide A with with the solvent molecules, the bonded and non-bonded parameters used in the simulations and the histograms of the residence time of the solvent molecules in the chlorin ring are available in the supporting information. Supporting information can be obtained free of charge from http://pubs.acs.org/doi/suppl/10.1021/ct1004627 .

Chapter 4

Molecular Dynamics Simulation Study of Aggregation of Astaxanthin

Khadga Karki, Justyna Lenda, Danilo Roccatano

Abstract

In this chapter, we present the results of molecular dynamics simulations of astaxanthin molecules to study the aggregation phenomena in different co-solvent mixtures of water and ethanol. Aggregation is observed in mixtures with water content higher than 50%. The structure of the aggregates change with the water to ethanol ratio; at higher ratio amorphous three-dimensional aggregates are observed while at lower ratio linear arrays are observed. The structures and sizes of the aggregates observed in the simulations, and the interactions that lead to the aggregation are discussed.

Introduction

Astaxanthin (AXT) is a carotenoid commonly found in aquatic animals [1]. Its molecular structure consists of a polyene chain terminated with two ring systems containing hydroxyl (-OH) and keto (=O) groups (Fig.(4.1)); its chemical formula is $C_{40}H_{52}O_4$. Like many other carotenoids, it forms aggregates when dissolved in hydrated polar

solvents [2]. Spectroscopic analysis of the aggregates have shown that the absorption spectra of the aggregates can be blue shifted as well as red shifted compared to that of the monomers depending on the aggregation conditions [3, 2, 4]. The blue shift is attributed to the formation of H-aggregates (monomers are stacked in a card-pack arrangement) and the red shift is attributed to the formation of J-aggregates (monomers are stacked in a head to tail arrangement).

In this work we use MD simulations to investigate the structural properties of the aggregates in various water-ethanol mixtures to get insight into the role of different interactions, *viz*; hydrophobic and hydrogen bond interactions, in the aggregation phenomena.

Molecular modeling and MD simulations

The structure of the molecule without hydrogen atoms were obtained from protein data bank[1] (pdb code: AXT). The hydrogens were added manually using the program MOLDEN [6]. The structure was then optimized using B3LYP method with the 6-31G** basis set using the program Gaussian 09 [7]. The optimized structure is shown in Fig.(4.1).

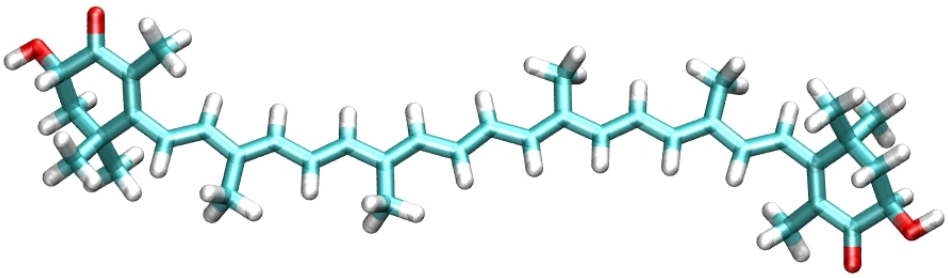

Figure 4.1: Optimized structure of AXT.

We used the OPLS-AA [8, 9, 10, 11] force field with additional parameters for the charges, the bond lengths, the angles and the dihedral angles based upon our QM

[1] www.pdb.org

calculations. OPLS force field parameters were also used for ethanol [12] and water (SPC/E model [13]).

All MD simulations and analysis were performed using the GROMACS package (version 4.0.7) [14]. The composition of the systems used in the simulations are shown in Table.(4.1). The temperature and the pressure of the system were coupled to the bath at 300 K and 1 bar using the Nose-Hoover [15] thermostat and the Parrinello-Rahman [16] pressure coupling method. The coupling time for the temperature and the pressure were set to 0.2 and 1.0 ps, respectively, and the compressibility was set to 4.5×10^{-5} bar^{-1}. For the simulations in ethanol, a cubic box of length 4.9 nm containing 1685 molecules was used. The coupling time for the temperature and the pressure were set to 0.1 and 1.5 ps, respectively. The compressibility was set to 1.2×10^{-4} bar^{-1}. The LINCS algorithm [17] was used to constrain all bond lengths. A 1.0-1.2 nm switched cutoff radius was used for the Lennard-Jones interactions. The PME method [18] was used for the electrostatic interactions with PME order of 4 , the Fourier spacing of 0.12 nm and dielectric permittivity of 1. The short-range neighbor list was set to 1.4 nm. All atoms were given an initial velocity obtained from a Maxwellian distribution at 300 K. A time step of 2 fs was used in the simulations and they were equilibrated by 500 ps of MD runs to allow the relaxation of the solvent molecules. After the equilibration, 50 ns production run for each simulation was performed.

The aggregation phenomena and the interactions that lead to aggregation were analysed using the radial distribution functions (RDF), spatial distribution functions (SDF) [19] and the structure of the aggregates.

Table 4.1: Composition of the different systems used in the simulations.

Simulation name	No. of AXT	No. of water molecules	No. of ethanol molecules
100% water	1	4050	0
0% water	1	0	4000
40% water	10	8000	12000
50% water	10	10000	10000
75% water	10	15000	15662
98% water	10	20710	464

Results and Discussion

Fig.4.2 shows the RDFs for different atom pairs in AXT and water (sub-figures (a) and (b)), and AXT and ethanol (sub-figures (c) and (d)). The RDFs in sub-figure (a) show that the distribution of H and O atoms of water molecules around the H atoms of AXT is lower in the vicinity of the later atoms compared to that in the bulk. Similar distribution is seen in the distribution of H and O atoms of ethanol in sub-figure (c). Sub-figure (c) also shows higher concentration of C atoms of ethanol around the hydrogen atoms of AXT in the vicinity of the later atoms compared to H and O atoms of ethanol. The low density of the atoms of water molecules and O and H atoms of ethanol near the H atoms of AXT is consistent with the fact that AXT overall is a hydrophobic molecule. However, the keto (=O) and hydroxyl (-OH) groups present in the terminal rings can form hydrogen bonds which affect the distribution locally. Sub-figure (b) shows the RDFs for H (solid line) and O (dashed line) atoms of water around the O atom of -OH group in AXT. The two peaks in the distribution of H at 0.18 and 0.33 nm on the flanks of the first peak at 0.28 nm of the distribution of O correspond to the two H atoms in a water molecule; the distribution of the peaks suggests the presence of organized hydration shells of water molecules near the -OH group. Similar distribution of H and O atoms of ethanol is seen in

sub-figure (d); the two peaks of the distribution of H atoms are at 0.19 and 0.33 nm, respectively, and the first peak of the distribution of O atoms is at 0.48 nm.

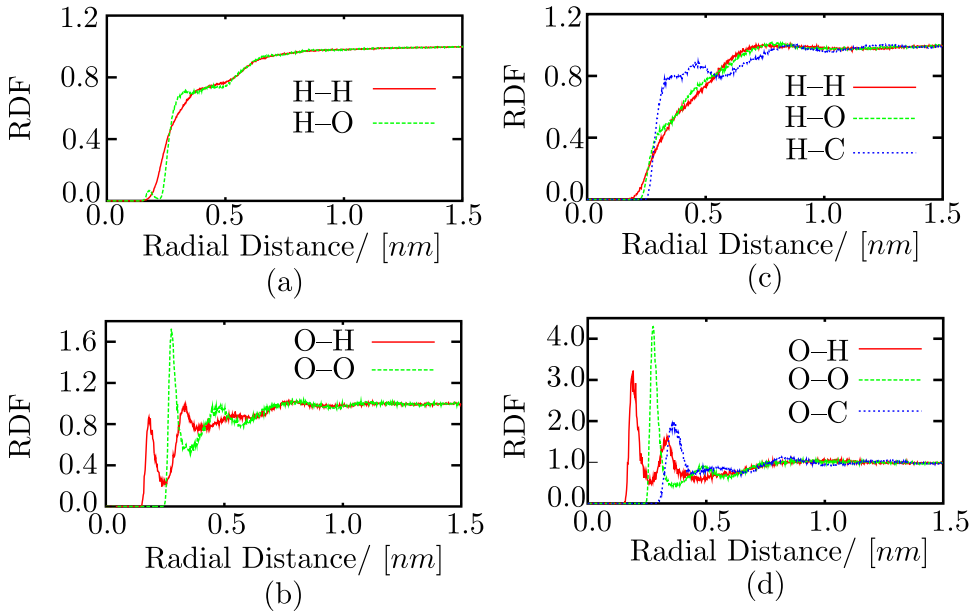

Figure 4.2: Pair correlation functions for different atom pairs: H atoms of AXT and H and O atoms of water (a), O atom of -OH group in AXT and H and O atoms of water (b), H atom of AXT and H, O and C atoms of ethanol (c), and O atoms of -OH group in AXT and H, O and C atoms in ethanol (d).

Sub-figures (a) and (b) in Fig.4.3 show the SDF of O (green) and H (yellow) atoms of water and ethanol molecules around AXT, respectively. Iso-surfaces with contour value of 10 and 13 are shown for the SDFs of water and ethanol, respectively. Sub-figure (a) shows lower concentration of water molecules around the central part of the polyene chain, which is more hydrophobic than the terminal rings where the concentration is higher. The SDF shows that O atoms of the water molecules are closer to AXT than H atoms except at two locations that are circled; these are the locations close to the -OH and =O groups that can form hydrogen bonds. The SDF in subfigure (b) also shows that the O atoms of the -OH group in ethanol are closer to AXT than the H atoms except at the vicinity of -OH and =O groups that are shown in circles.

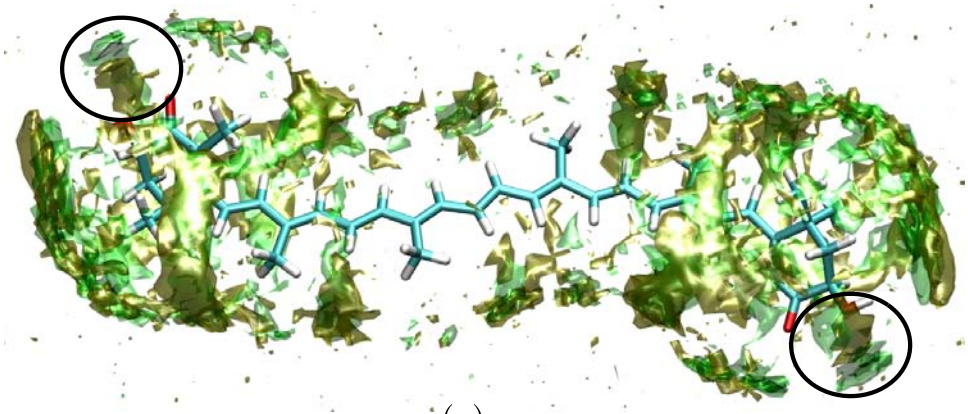

(a)

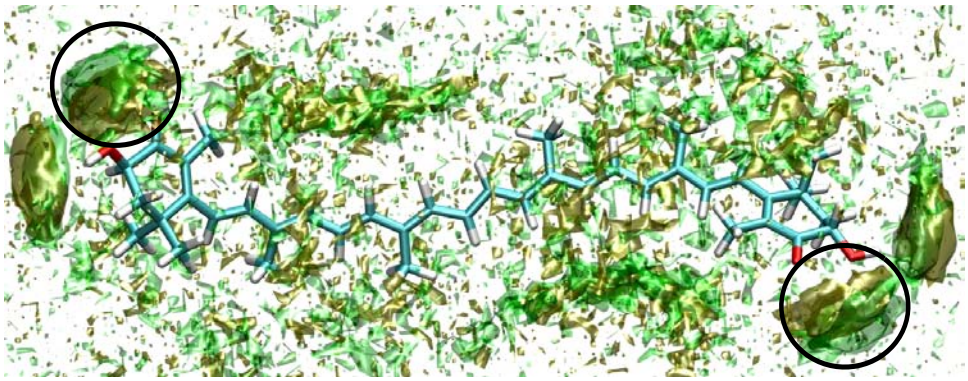

(b)

Figure 4.3: SDF of O (green) and H (yellow) atoms of water (a) and ethanol (b). The circles locate the regions where the H atoms of the solvents are attracted towards the molecule forming hydrogen bonds.

Both the RDFs and SDFs indicate that hydrophobic effects play a major role in aggregation of AXT which is also evident by the fact that aggregation is observed in systems with higher water content. Fig. 4.4 (a),(b) and (c) shows the structures of monomers and aggregates observed in the simulations containing 50% and 75% water in water-ethanol mixtures. Sub-figure (a) shows the starting configuration in the simulations, sub-figures (b) and (c) show the final configurations in the mixtures with 50% and 75% water, respectively; aggregation is observed only in the later mixture. However, when the simulations are started with the aggregate as initial configuration complete disaggregation of the aggregate is not observed within 50 ns of simulation

in 50% water mixture. On the other hand, complete disaggregation to monomers is observed in 40% water mixture. The final configurations of the AXT molecules after 50 ns of simulations starting with the initial configuration in sub-figure (c) are shown in sub-figures (d) and (e).

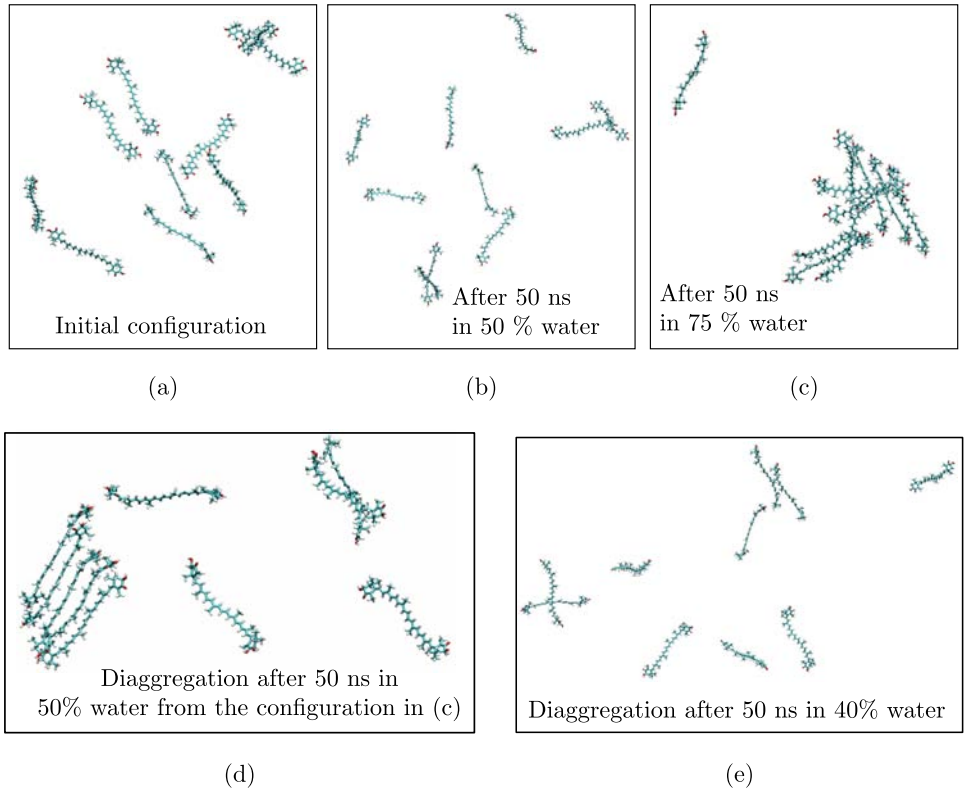

Figure 4.4: Monomers and aggregates observed after 50 ns of simulations of AXT in water-ethanol mixtures with 50% (b) and 75% water (c); the initial configuration is shown in (a). (d) and (e) show the final configurations after 50 ns simulations started with the configuration of the aggregate obtained in (c) in 50% and 40% water, respectively. Complete disaggregation to monomers is observed only in the mixture with 40% water.

The concentration of water in the mixtures affects the structure of the aggregates. As the aggregation is due to the hydrophobic effects, the aggregates tend to be more compact in mixtures with higher water content. Sub-figures (a), (b) and (c) in Fig. 4.5 show some of the structures of the aggregates observed in 98%, 75% and 50% water mixtures, respectively. The structure in (a) is a compact cylindrical three-

dimensional structure; some of the molecules pointed out by the arrows are arranged in a card-pack geometry while others are randomly oriented. The structure in (b) has less compact three-dimensional arrangement of a dimer, a trimer and monomers. The molecules in the dimer and the trimer are arranged in a card-pack geometry. The structure in (c) is a linear array of molecules; the molecules can be grouped into three dimers as indicated by the labels i, ii and iii, respectively. The monomers in each of the dimers are in card-pack arrangement while the dimers themselves are arranged in a head to tail configuration. In general, it can be inferred that the decreasing concentration of water in the mixture changes the less ordered and compact three-dimensional configuration of the aggregates to a more ordered linear array. However, a transition from H-aggregates to J-aggregates, as it is postulated to occur based on the absorption spectra of the aggregates in co-solvent mixtures [3, 2, 4], cannot be unambiguously inferred from the results of the simulations: firstly the three-dimensional aggregates are not H-aggregates and secondly even the linear array shown in sub-figure (c) is a combination of H and J aggregates. Considering the fact that the aggregation is driven by hydrophobic interactions, unambiguous formation of H-aggregates in the real systems is also less likely.

It is interesting to note that though the hydrophobic interactions play major role in the aggregation, the linear arrangement as shown in Fig. 4.5(c) requires other directed interactions; in case of AXT it is the network of hydrogen bonds between the bridging water molecules and -OH and =O groups in the rings. An example of such a network of hydrogen bonds in shown in Fig. 4.6. It is also interesting to note that the contribution of the hydrogen bond interactions in the alignment of the molecules in the aggregates decreases with increasing water concentration. In fact, the hydrogen bond interactions between the water molecules and the -OH and =O groups themselves become less energetic; this is inferred from the RDF of the H atoms of water molecules around the O atoms of -OH in AXT (shown in Fig. 4.7). Overall,

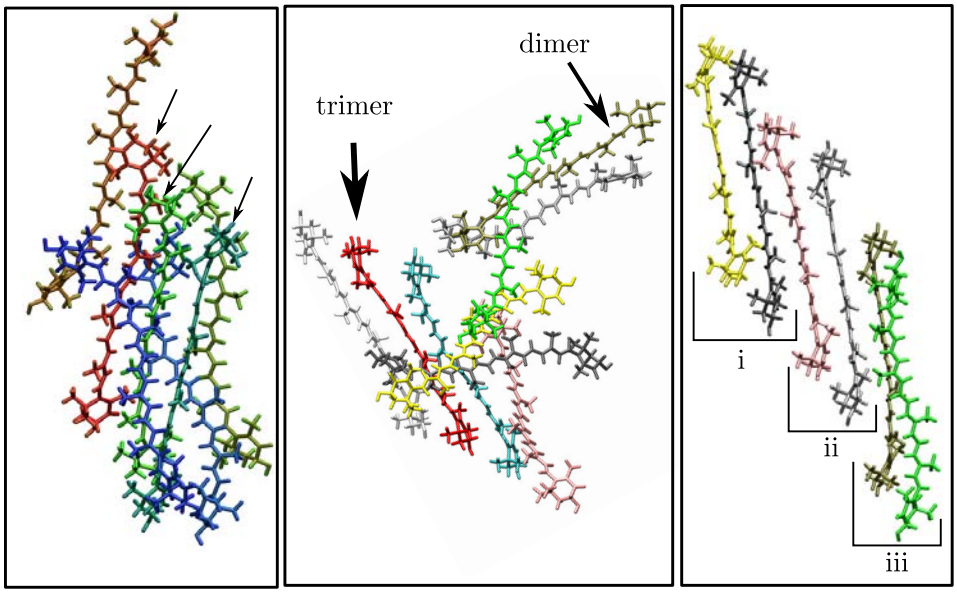

Figure 4.5: Representative structures of aggregates in water-ethanol mixtures with 95% (a), 75% (b) and 50% (c) of water in the mixtures.

the results indicate that the hydrophobic interactions are responsible for bringing the AXT molecules together and hydrogen bond interactions are responsible for aligning them in a linear array.

Conclusions

Herein, we have presented the investigation of aggregation of AXT in different mixtures of water and ethanol using MD simulations. The simulations show that the amount of water present in the mixtures changes the structure of the aggregates; three-dimensional compact aggregates are observed in mixture with high water content and linear aggregates are observed in lower water content. However, the aggregates cannot be unambiguously identified as H or J-aggregates. We also observe that, though hydrophobic interactions play major role in aggregation, a network of hydrogen bonds between the -OH and =O groups of AXT and water molecules maintain

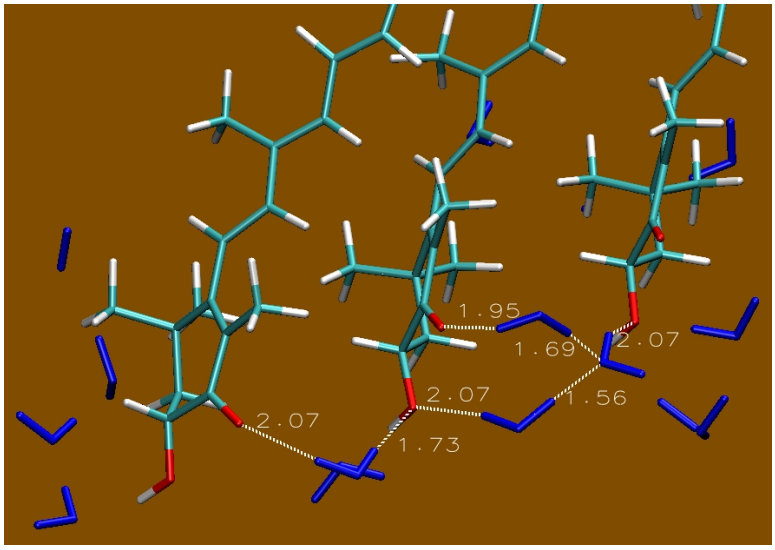

Figure 4.6: An example of hydrogen bond network between the AXT molecules in an aggregate.

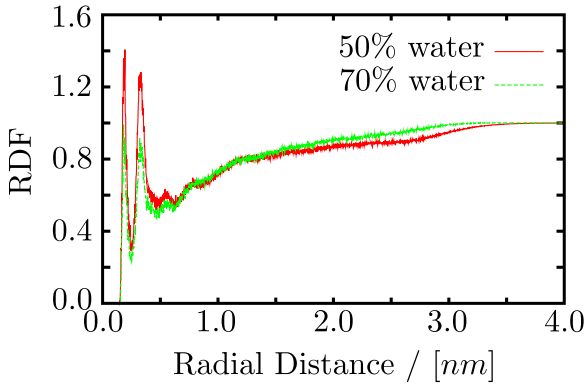

Figure 4.7: RDF of H atoms of water molecules around O atoms of the -OH group in AXT in water-ethanol mixtures with 50% water (solid line) and 75% water (dotted line). The peak heights at 0.19 and 0.33 nm radial distance in 70% water mixture are smaller than in 50% water mixture.

the linear arrangement of the molecules in the mixtures with lower water content. Aggregation is not observed in mixtures in which the water content is 40% or less.

Acknowledgements

This study was performed using the computational resources of the CLAMV (Computer Laboratories for Animation, Modeling and Visualization) at Jacobs University Bremen. This work was performed within the graduate program "Nanomolecular Science."

Bibliography

[1] Miki, W. *Pure & Appl. Chem.* **1991,** *63,* 141-146.

[2] Britton, G.; Liaaen-Jensen, S.; Pfander, H., Eds.; *Carotenoids, Volume 4: Natural Functions;* Birkhäuser Verlag: Basel, 2008.

[3] Köpsel, C.; Möltgen, H.; Schuch, H.; Auweter, H.; Kleinermanns, K.; Martin, H.-D.; Bettermann, H. *J. Mol. Struct.* **2005,** *750,* 109-115.

[4] Giovannetti, R.; Alibabaei, L.; Pucciarelli, F. *Spectrochim Acta A* **2009,** *73,* 157-162.

[5] Spano, F. C. *J. Am. Chem. Soc.* **2009,** *131,* 4267-4278.

[6] Schaftenaar, G.; Noordik, J. H. *J. Comput.-Aided Mol. Design* **2000,** *14,* 123-134.

[7] Frisch, M. J.; Trucks, G. W.; Schlegel, H. B.; Scuseria, G. E.; Robb, M. A.; Cheeseman, J. R.; Scalmani, G.; Barone, V.; Mennucci, B.; Petersson, G. A.; Nakatsuji, H.; Caricato, M.; Li, X.; Hratchian, H. P.; Izmaylov, A. F.; Bloino, J.; Zheng, G.; Sonnenberg, J. L.; Hada, M.; Ehara, M.; Toyota, K.; Fukuda, R.; Hasegawa, J.; Ishida, M.; Nakajima, T.; Honda, Y.; Kitao, O.; Nakai, H.; Vreven, T.; Montgomery, Jr., J. A.; Peralta, J. E.; Ogliaro, F.; Bearpark, M.; Heyd, J. J.; Brothers, E.; Kudin, K. N.; Staroverov, V. N.; Kobayashi, R.; Normand, J.; Raghavachari, K.; Rendell, A.; Burant, J. C.;

Iyengar, S. S.; Tomasi, J.; Cossi, M.; Rega, N.; Millam, J. M.; Klene, M.; Knox, J. E.; Cross, J. B.; Bakken, V.; Adamo, C.; Jaramillo, J.; Gomperts, R.; Stratmann, R. E.; Yazyev, O.; Austin, A. J.; Cammi, R.; Pomelli, C.; Ochterski, J. W.; Martin, R. L.; Morokuma, K.; Zakrzewski, V. G.; Voth, G. A.; Salvador, P.; Dannenberg, J. J.; Dapprich, S.; Daniels, A. D.; Farkas, .; Foresman, J. B.; Ortiz, J. V.; Cioslowski, J.; Fox, D. J. "Gaussian 09 Revision A.1", Gaussian Inc. Wallingford CT 2009.

[8] Jorgensen, W. L.; Maxwell, D. S.; Tiraldo-Rives, J. *J. Am. Chem. Soc.* **1996,** *118,* 11225-11236.

[9] Jorgensen, W. L. Encyclopedia of Computational Chemistry. In , Vol. 3; Wiley: New York, 1998; Chapter OPLS, force field, pages 1986–1989.

[10] Jorgensen, W. L.; McDonald, N. A. *J. Mol. Struct. (THEOCHEM)* **1998,** *424,* 145-155.

[11] Jorgensen, W. L.; McDonald, N. A. *J. Phys. Chem. B* **1998,** *102,* 8049-8059.

[12] Jorgensen, W. L. *J. Phys. Chem.* **1986,** *90,* 1276-1284.

[13] Berendsen, H. J. C.; Grigera, J. R.; Straatsma, T. P. *J. Phys. Chem.* **1987,** *91,* 6269-6271.

[14] Hess, B.; Kutzner, C.; van der Spoel, D.; Lindahl, E. *J. Chem. Theory Comput.* **2008,** *4,* 435-447.

[15] Hoover, W. G. *Phys. Rev. A* **1985,** *31,* 1695-1697.

[16] Parrinello, M.; Rahman, A. *J. Apply. Phys.* **1981,** *52,* 7182-7190.

[17] Hess, B.; Bekker, H.; Berendsen, H. J. C.; Fraaije, J. G. E. M. *J. Comp. Chem.* **1997,** *18,* 1463-1472.

[18] Essmann, U.; Perera, L.; Berkowitz, M. L.; Darden, T.; Lee, H.; Pedersen, L. G. *J. Chem. Phys.* **1995,** *103,* 8577-8592.

[19] Kulasik, P. G.; Laaksonen, A.; Svishchev, I. M. Molecular dynamics: from classical to quantum methods. In ; Elsevier Science B.V.: Sara Burgerhartstraat 25, Amsterdam, 1999; Chapter Spatial Structure in Molecular Liquids, pages 61–90.

[20] Chandler, D. Introduction to modern statistical mechanics. In ; Oxford University Press: University of California, Berkeley, 1987; Chapter 7, page 201.

Chapter 5

Study of structural and dynamic properties of liquid phenyltrimethoxysilane

Khadga Karki, Arnulf Materny, and Danilo Roccatano[1]

Abstract

Herein, we present a combined experimental and computational study of liquid phenyltrimethoxysilane. A femtosecond time-resolved optical Kerr effect experiment has been performed to study the rotational diffusion of the molecule. A new all-atoms molecular model of the compound, based on the OPLS force field, has been developed to reproduce the rotational diffusion time constant and other physical and dynamic properties available in the literature. The density obtained from the simulations is 1074 ± 4 kg m^{-3}, which is within 1% of the experimental value of 1062 kg m^{-3}. The viscosity from the simulations is 1.6 ± 0.1 mPa s while the experimental value is 2.1 mPa s. The average bulk dipole moment of 1.8 ± 0.5 Debye obtained from the simulation matches the experimental value of 1.77 Debye. The average relative dielectric constant from the simulations is 3.86±0.04, which is within 13% of the experimental value (4.4). The rotational diffusion time of the dipole moment obtained from the simulations is 20.39 ± 0.06 ps, which is in excellent agreement with

[1]This chapter is reproduced without modification from the article published in *Phys. Chem. Chem. Phys.,* 2011, **13**, 11864-11871

the experimental value of 20 ± 1 ps obtained from our measurements. The new model has also been used to calculate structural and dynamic properties of the molecule not yet determined experimentally.

Introduction

Organosilanes and siloxanes are molecules containing silicon-carbon and silicon-oxygen bonds [1]. Their ability to polymerize [2] forming sol/gel materials and polyhedral organosilane structures (POSS) [3] is used to make materials for new technological applications. Furthermore, they can be employed to functionalize inorganic surfaces with different organic functional groups. The presence of an organic layer on inorganic surfaces can substantially modify interfacial properties of the hybrid material. In addition, the new hybrid material can exhibit both the customized functional capability of the organic layer and the robustness of the inorganic framework [4]. The urge to understand the behaviour of these new materials at the molecular level is evident from the considerable number of experimental studies accumulated over more than half a century of research. Unfortunately, experimental techniques are still rather inefficient in understanding both the structural and dynamic properties of disordered hybrid systems. However, computational techniques, in particular molecular dynamics (MD) simulations, can provide information on both the properties of these materials with atomistic details. MD simulations, based on force-fields primarily suited for studying inorganic systems, have been done on POSS [3] and dimethoxysilane [5, 6, 7]. The parameters for class II force fields (CFF) [8] developed for polysiloxanes [9] and polysilanes [10] have been used for the MD simulations of the condensed phases of the polymers. However, the current research trend is in studying (bio)organic-inorganic hybrid systems of silanes and siloxanes.

[1]† Electronic Supplementary Information (ESI) available: Coordinates of the atoms in the optimized geometry, partial charges, figures for mean square displacement, dipole moment distribution and the dielectric constant.

To the best of our knowledge, molecular models based on the force fields like OPLS, which can be used to simulate silane functionalized materials with proteins and other biological systems, have yet to be proposed.

In this paper, we report optimized parameters for the OPLS force field of one of the important organosiloxanes, phenyltrimethoxysilane (PhTMS). The calculated physico-chemical properties of the model have been validated against different experimental data, like density, viscosity, bulk dipole moment and relative permittivity. In addition, we have conducted transient birefringence measurements to obtain the rotational diffusion time of the dipole moment in bulk solution that has also been reproduced in the simulations. Different structural and dynamic properties that are not yet available from experimental measurements have also been calculated using the model.

The paper is organized as follows. In the "Material and Methods" section, the details of the force field parameters, MD simulations, and analysis of the various properties of the system are presented. The experimental technique and the setup used to measure the rotational dynamics of the molecule is also presented in this section. The different properties that are known experimentally and that can be compared with the results from the simulations are presented at the beginning of the section "Results and Discussion". Properties like the self-diffusion coefficient and the radial distribution function (RDF) obtained from the simulations, but not yet determined experimentally, are presented later in the section. Finally, in the "Conclusion", a summary of the study is reported with an outlook on the further applications of the model.

Material and Methods

PhTMS force field parameters.

The geometry optimization was performed with the DFT-Becke3LYP method using the 6-31G* basis set. All quantum mechanics calculation were performed using the program Gaussian 03 [11]. The optimized structure is reported in Fig. (5.1). The initial partial atomic charges were calculated by fitting the electrostatic potential to the charge density of the optimized structure using the CHELPG procedure [12]. The partial charges were later increased by 10% to reproduce the experimental dielectric constant of the liquid system. The coordinates of the optimized structure and the partial atomic charges are reported in the ESI.

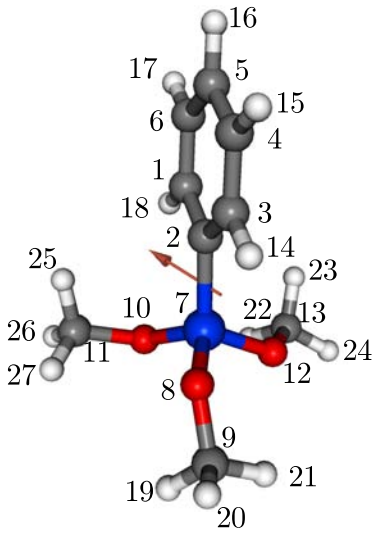

Figure 5.1: Optimized geometry of PhTMS. Coloring of the atoms: white H, grey C, red O and blue Si. The arrow shows the direction of the dipole moment.

The bond lengths, angles and dihedral angles were obtained from the optimized geometrical structure of the molecule. All atom OPLS [13, 14] force field parameters were used in the simulations. The force constants for bonds, bond angle and torsional interaction terms were adapted from OPLS force field parameters for similar functional groups. The Lennard-Jones parameters were optimized to reproduce

the experimental density of the compound. The final optimized parameters for the PhTMS are reported in Table 5.1.

Table 5.1: Parameters for the PhTMS Force Field

atoms	σ/ [nm]	ϵ/[kJ mol^{-1}]
Si	0.37000	1.70704
C	0.35090	0.35076
O	0.29600	0.87864
H_{Ph}[a]	0.24200	0.00505
H_M[b]	0.25000	0.00503

bonds	bond length/ [nm]
C-C	0.139
C-Si	0.187
C-H_{Ph}	0.107
Si-O	0.167
C-O	0.142
C-H_M	0.108

angles	angle/ [deg]	force constant/[kJ mol^{-1} rad^{-2}]
C-C-C	120	527.18
C-C-H_{Ph}	120	292.88
C-C-Si	120	397.48
C-Si-O	110	397.48
O-C-H_M	108	292.88
H_M-C-H_M	109	292.88

dihedrals	Ryckaert-Belleman Coefficients/[kJ mol^{-1}]					
	C0	C1	C2	C3	C4	C5
C-C-C-C	30.334	0.000	-30.334	0.000	0.000	0.000
O-Si-O-C	20.920	0.000	-20.920	0.000	0.000	0.000
Si-O-C-H_M	1.589	4.770	0.000	-6.360	0.000	0.000
O-Si-C-C	-1.428	-0.005	55.403	1.253	-41.518	-1.351

[a] Phenyl hydrogens.
[b] Methyl hydrogens.

MD simulations.

All simulations and analyses were performed using the GROMACS package [15]. The simulations were performed in a cubic box of length 4.925 nm containing 389 molecules with periodic boundary conditions. An infinite external dielectric constant was used to get a relatively stable estimate of the dielectric constant [16]. The density, linear and rotational diffusion constants, radial and spatial distribution functions, and

dielectric constant were calculated from a 35 ns long equilibrium MD simulations at constant pressure.

Constant volume simulations were done to calculate the isothermal compressibility and the specific heat at constant volume. Two simulations with different box lengths, 4.91 nm and 4.93 nm, were done to compute the isothermal compressibility (see Eq.(5.10)). Two 5 ns long simulations at 300 and 315 K were performed to calculate the isothermal compressibility using Eq.(5.12). A 35 ns long simulation was also done in constant volume at 300 K to calculate the viscosity using the Green-Kubo formula (Eq.(5.1)).

The SHAKE algorithm [17] was used to constrain all bond lengths in the simulations. The simulations were done with a time step of 2 fs. A 0.9-1.1 nm switched cutoff [15] radius was used for the Lennard-Jones interactions. The PME method [18] was used for the electrostatic interactions with PME order of 4 and Fourier spacing of 0.12 nm. The cutoff of the short-range neighbor list was set to 1.2 nm. All atoms were given an initial velocity generated from a Maxwell distribution at the temperature used in the simulations. The temperature of the systems was coupled to a bath at the simulation temperature using the Nose-Hoover thermostat [19] while the pressure was kept constant using the Parrinello-Rahman pressure coupling method as implemented in GROMACS [20, 21]. The coupling constants for the temperature and the pressure were 0.5 and 3.0 ps, respectively, while the compressibility was set to 9.1×10^{-5} bar^{-1}.

Physical properties

Viscosity. The shear viscosity of a liquid was calculated from the fluctuations of the off-diagonal elements of the pressure tensor using the Green-Kubo formula

reformulated as an Einstein relation [22]:

$$\eta = \lim_{t\to\infty} \frac{V}{2k_BT}\frac{d}{dt}\left\langle \left(\int_{t_0}^{t_0+t} P_{xz}(t')dt' \right)^2 \right\rangle_{t_0} \tag{5.1}$$

where, V is the volume of the box, k_B is the Boltzmann constant, T is the temperature and P is the pressure.

Dielectric constant. The dielectric constant ϵ was calculated using the fluctuation formula [23, 24],

$$\epsilon - \epsilon_\infty = \frac{4\pi\langle \Delta M^2 \rangle}{3Vk_BT} \tag{5.2}$$

where, ϵ_∞ is the high frequency dielectric constant which is approximated to 1. The fluctuation $\langle \Delta M^2 \rangle$ is given by

$$\langle \Delta M^2 \rangle = \left(\langle M^2 \rangle - \langle M \rangle^2 \right) \tag{5.3}$$

where M is the dipole moment of the simulation box.

Structural properties. Pair correlation functions $g_{xy}(r)$ (also known as radial distribution function (RDF)), where x and y denote the atom pairs, were calculated to get information on the local enviroment around each solvent molecule. The correlation functions were computed using three different pairs of atoms, namely, Si-Si, Si-O and Si-C (C from phenyl ring). The number of different atomic species in the different solvation shell around the Silicon atom was calculated using the running integration number (RIN)

$$n = 4\pi\rho_0 \int_0^R g_{xy}(r) r^2 dr \tag{5.4}$$

where ρ_0 is the number density of the atoms.

The anisotropy in the structure of the first solvation shell was obtained from the spatial distribution function (SDF) [25]. For the calculation of the SDF, a reference frame was defined using the three atoms numbered 1,2, and 3 in Fig. (5.1). The distribution was calculated in the Cartesian coordinate system with origin fixed to atom 1, two of the vectors defined by the vectors joining atom 1 to atom 2 and atom 3 and the third vector orthogonal to the plane formed by the three atoms.

Dynamical properties

Translational diffusion. The translational diffusion coefficient of PhTMS was calculated using the Einstein relation [26]:

$$6Dt = \frac{1}{N}\left(\sum_{i=1}^{i=N} ||\mathbf{r}_i(t) - \mathbf{r}_i(0)||^2\right) \tag{5.5}$$

where $\mathbf{r}_i(t)$ is the coordinate vector of the particle i at time t, $\mathbf{r}_i(0)$ the coordinate vector of the particle i at time $t = 0$ and N the total number of particles.

For a spherical particle, the self-diffusion coefficient is related to the viscosity by the Stokes-Einstein relation:

$$D = \frac{k\,T}{6\pi\eta r_a} \tag{5.6}$$

where r_a is the radius of the particle. The diffusion coefficients obtained using Eq.(5.5) and Eq.(5.6) were compared to check the validity of Eq.(5.6) in the case of PhTMS.

Rotational diffusion. The rotational diffusion of the molecule around a vector was calculated by using the autocorrelation function of the vector:

$$C_l(t) =< P_l(\mathbf{n}(0) \cdot \mathbf{n}(t)) > \tag{5.7}$$

where P_l is the Legendre polynomial of order l, $\mathbf{n}$ is the unit vector, about which the autocorrelation is calculated, and the brackets indicate the average along the

trajectory [27]. The correlation function (Eq.5.7) in general can be approximated by an exponential decay [28]:

$$C_l(t) = a \exp(-l(l+1)D_r t) \tag{5.8}$$

with the relaxation time τ_l given by

$$\tau_l = \frac{1}{l(l+1)D_r} \tag{5.9}$$

where D_r is the rotational diffusion constant. To compare with the experimental result, the second order Legendre polynomial was used to compute the rotational diffusion time constant of the dipole moment of the molecule. The Debye relaxation time was calculated using the first order Lengendre polynomial [29].

Thermodynamic properties

Isothermal compressibility. The isothermal compressibility β_T was evaluated using the finite difference relationship [30]:

$$\beta_T = \frac{1}{\rho}\left(\frac{\partial \rho}{\partial P}\right)_T \approx \left(\frac{\Delta \ln P}{\Delta P}\right)_T = \left(\frac{\ln\left(\frac{\rho_2}{\rho_1}\right)}{P_2 - P_1}\right)_T \tag{5.10}$$

and also estimated from the fluctuations using the relation [26]

$$\beta_T = \frac{\langle \Delta V^2 \rangle}{V k_B T} \tag{5.11}$$

where V is the volume of the box. The parameters ρ_1, ρ_2 and P_1, P_2 are the densities and the pressures obtained from two simulations at the same temperature but different pressures, respectively. The difference in pressure was obtained by increasing the box volume by 0.12%.

Thermal expansion coefficient. The thermal expansion coefficient α was evaluated using the following numerical derivative [30]:

$$\alpha = \frac{1}{V}\left(\frac{\partial V}{\partial T}\right)_P = -\frac{1}{\rho}\left(\frac{\partial \rho}{\partial T}\right)_P \approx -\left(\frac{\ln\left(\frac{\rho_2}{\rho_1}\right)}{T_2 - T_1}\right)_P \tag{5.12}$$

and also estimated from the fluctuations in the volume of the system using the relation [26]

$$\alpha = \frac{\langle \Delta V \Delta \mathcal{H} \rangle + P\langle \Delta V^2 \rangle}{k_B T^2 V} \tag{5.13}$$

where $\mathcal{H}$ is the Hamiltonian of the system.

Heat of vaporization. The heat of vaporization was estimated as

$$\Delta H_{vap} = -\left[E(l) - E_{intra}(g)\right] + RT \tag{5.14}$$

where $E(l)$ is the energy due to the intra and inter-particle interaction in the liquid, $E_{intra}(g)$ is the intramolecular energy in the gas phase and R is the gas constant. The intramolecular energy was averaged by performing a simulation of a single particle in the box.

Specific heat. The specific heat at constant volume C_v was estimated using the relation [26]

$$\langle \Delta \mathcal{H}^2 \rangle_{NVT} = k_B T^2 C_v. \tag{5.15}$$

The specific heat at constant pressure C_p was estimated using the relation [31]

$$C_p - C_v = \frac{\alpha^2 T V}{\beta_T}. \tag{5.16}$$

where V is the volume of one kilogram of the substance when C_P and C_v are calculated per kilogram.

Experimental setup

Determination of rotational relaxation time constant using the optical Kerr effect (OKE) . Electric fields can induce birefringence in different media. This well-known Kerr effect can also be induced when strong electromagnetic light fields interact with the molecules. OKE is the birefringence induced on an isotropic medium due to a strong linearly polarized light field [32]. In the case of the birefringence induced in polar liquids four dynamically distinct responses associated with the nonlinear susceptibility are observed [33]. These responses have different origins, namely the electronic cloud distortion, the molecular libration, the molecular redistribution, and the molecular reorientational motion [34, 32]. The timescales of these responses are also different. When a femtosecond pump pulse is used to induce the birefringence and another time delayed probe pulse is used to interrogate the transient birefringence, the signal, *i.e.* the probe laser light transmitted through a crossed polarizer, as a function of delay time between pump and probe pulses shows features corresponding to these four different responses of the system. An instantaneous symmetric trace is observed at time zero, which is due to the ultrafast relaxation of the electron cloud distortion occurring in few hundred attoseconds [32]. An approximately exponentially decaying trace is observed on a sub-picosecond time scale, which is due to the fastest nuclear motions. On a longer timescale, the trace shows a bi-exponential decay with two time constants, one in the range of 0.5-5 ps and one in the range of 5-100 ps [35]. The former is due to the translational anisotropy and the resultant intermolecular distortion of the molecular polarizability and the later is due to the diffusive reorientation [33].

The relaxation time of the diffusive reorientation calculated from the MD simulations can be compared with the experimentally determined diffusive reorientation time.

The schematic of the setup of the optical Kerr experiment used to measure the rotational diffusion is shown in Fig. (8.1). In the experiments, deposition grade (purity $\geq 98\%$) PhTMS, purchased from Sigma-Aldrich [36] was used as the sample without further purification. Pulses at 775 nm with a length of 150 fs were generated in a fiber laser followed by a Ti:Sapphire chirped-pulse amplifier (CPA 2010, Clark-MXR, Inc.) at 984 Hz repetition rate. These pulses with an average pulse energy of approx. 1 mJ were split into two equal parts, which were used to pump two optic parametric amplifiers (OPAs; TOPAS, Light Conversion). One of the OPAs was used to generate pulses at 510 nm, which after compression in a prism setup had a length of approx. 100 fs. The second OPA was used to generate pulses at 650 nm with a length of approx. 110 fs after compression. Both pulses were horizontally polarized. The polarization was further controlled using polarizers. A Berek compensator was used in the beam path of the pump pulse at 650 nm to rotate the polarization by 45°. The beam was then focused into the cuvette (length 0.5 cm) containing the sample with a lens of focal length $f = 30$ cm. The average pulse energy at the sample was about 1 μJ. The probe pulses at 510 nm were variably delayed by a computer-controlled translation stage in a Michelson arrangement and then focused into the sample with the same lens. The average probe pulse energy at the sample was about 50 nJ. After the sample, the probe beam was collimated using a second lens. The spectrum of the beam was then recorded using a monochromator equipped with a CCD detector. An analyzer was used before the spectrometer to extinguish the probe beam when no pump beam was focused into the sample. By varying the delay time between the pump and probe laser pulses, the time-dependent birefringence could be observed by measuring the intensity of the probe laser light transmitted through the analyzer due to its changed polarization state.

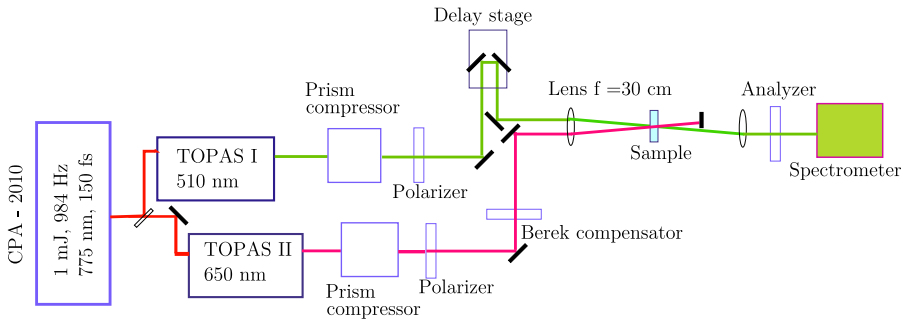

Figure 5.2: Experimental setup to determine the rotational diffusion time constant of PhTMS. Transient birefringence is induced in the sample using pump beam at 650 *nm* and the relaxation of the birefringence is probed by polarized probe beam. See the text for the details of the setup.

Results and Discussion

Physical properties

Density and viscosity.

The density of PhTMS calculated from the simulation is 1072.8 ± 0.1 kg m^{-3} which is within 1% of the experimental density of 1064 kg m^{-3} at 298.15 K.

The average viscosity calculated using Eq.(5.1) is 1.6 ± 0.1 mPa s. The viscosities calculated from the three components of the pressure tensor, P_{xz}, P_{xy} and P_{yz} (Fig.(5.3)), are relatively constant and similar from $t_0 = 20$ ps to 500 ps so the averaging is done over this interval. The experimental viscosity of PhTMS is 2.1 mPa s [37], which is about 25% higher than the computed value.

Dipole moment and dielectric constants.

The distribution of the dipole moment averaged over the trajectory is shown in Fig.(1) of ESI. The average dipole moment from the simulation is 1.8 ± 0.5 Debye which is in excellent agreement with the experimental value of 1.77 Debye of liquid PhTMS [38].

The dielectric constant estimated using Eq.(5.2) for different simulation times is shown in Fig.(2) of ESI. The fluctuation of 1.0% calculated over the last 15 ns of the

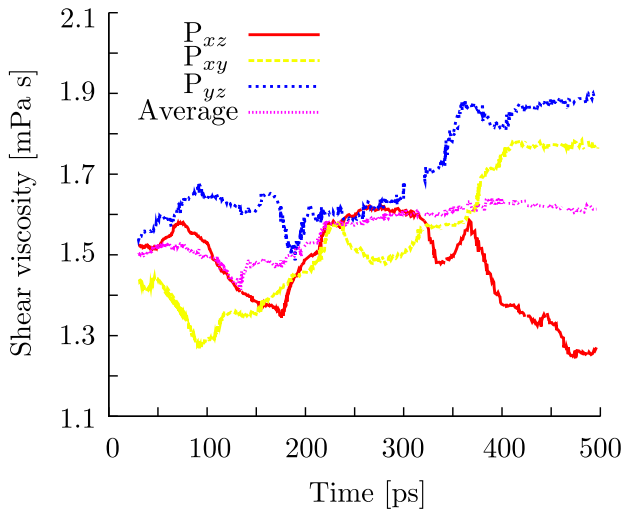

Figure 5.3: The viscosity of PhTMS calculated from the fluctuations in the pressure tensor. The viscosity calculated from the three components of the tensor are similar to each other. The average viscosity obtained from the simulation is 1.6 ± 0.1 mPa s.

simulation indicates a good convergence. The calculated dielectric constant is equal to 3.86 ± 0.04 with a discrepancy of only 13% from the experimental value of 4.44 [38].

Structural properties.

The RDFs and SDFs are used to describe the structure of the solvation shell around each of the solvent molecule. The RDF and RIN of silicon, oxygen and carbon atoms of the phenyl ring around the silicon are shown in Fig.(5.4). The pair distribution function $g_{Si-Si}(r)$ has two distinct peaks at 0.65 nm and 1.27 nm. These two peaks indicate the extent of the first and the second solvation shells, respectively. The distance between the peaks is about 0.63 nm. Thus, the approximate radius of the molecule is 0.32 nm. The RIN up to 0.66 nm shows about 2.5 Si atoms around the reference silicon atom. $g_{Si-O}(r)$ shows three peaks at 0.58, 0.75 and 1.34, respectively. The first two peaks come from the neighboring molecules in the first solvation shell. The distinct two peaks indicate preferential spatial arrangement of the molecules in the first shell. The RIN up to 0.58 nm shows 3.8 O atoms and the RIN up to 0.75 nm shows 14 O atoms which correspond to 1.3 and 4.7 molecules, respectively. The

RDF of C atoms has a distinct peak at 0.63 nm and other weak peak at 1.02. The RIN up to 0.63 nm is 13.72 which corresponds to 2.3 molecules.

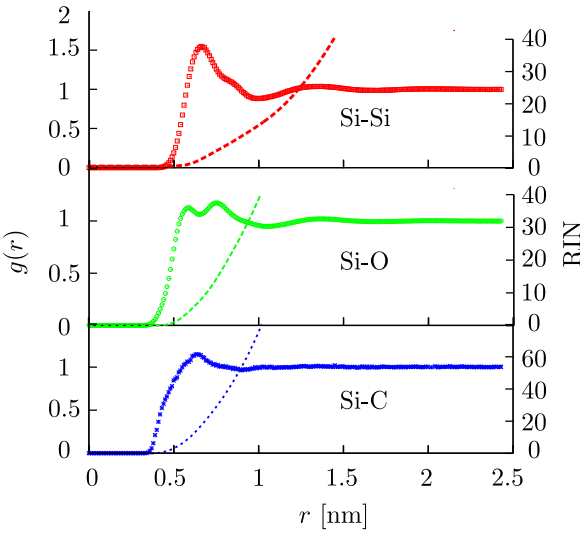

Figure 5.4: The radial distribution function, $g(r)$, of Si ,O and C atoms of the phenyl ring around the Silicon. The points show $g(r)$ and the dotted lines show the running integration number for the corresponding pairs.

The anisotropic distribution of the molecules in the first solvation shell is evident from the SDF of the different atomic species (Fig.(5.5)). The SDF is calculated in a 8 nm^3 cubic grid with a bin width of 0.05 nm. The SDF of Si atom shows a high distribution in the plane of phenyl ring and in one of the lateral sides, which give the first peak and the shoulder in the flank of $g_{Si-Si}(r)$, respectiveily. The SDF of two of the oxygen atoms (atom 8 and atom 10 in Fig.(5.1)), green and transparent blue contour surfaces, overlap while the SDF of the third oxygen atom (atom 12 in Fig.(5.1)), red contour surface, is distinct. This indicates that the molecules in the first solvation shell have a preferential orientation that is induced by the dipole-dipole interaction. The SDF of the carbons of the methyl groups show high density in the lateral positions of the phenyl rings (Fig.(5.5c)).

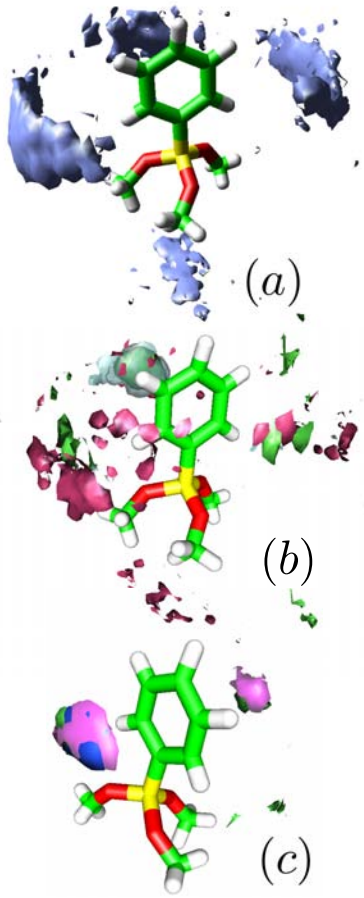

Figure 5.5: The spatial distribution functions. Isosurfaces of (a) Si with contour value 2.5, (b) O with contour values 2.2 (green) for O8, 2.2 (transparent blue) for O10 and 1.9 (red) for 012, and (c) C of methyl groups with contour values 3.4 (pink) for C9 , 4.4 (blue) for C11 and 3.2 (green) for C13.

Dynamical properties

Self-diffusion.

The self-diffusion coefficient of PhTMS has not yet been determined experimentally. As our model reproduces well physical and dynamic properties like density, viscosity, dielectric constant, and rotational diffusion time constant, the self-diffusion coefficient predicted by the model can be expected to be close to the actual value.

Eq.(5.5) is used to compute the diffusion coefficient from the simulation. The average root-mean square displacement is shown in Fig. (3) of ESI. A linear fit

$f(t) = at$ of the points from 0 - 10 ns gives $a = (3.7267 \pm 0.0003) \times 10^{-9}$ m^2 s^{-1} . The corresponding self diffusion coefficient is $(0.62)\times 10^{-9}$ m^2 s^{-1}. The self-diffusion estimated from the viscosity and the hydrodynamic radius of the molecule (calculated from the first minimum of the $g_{Si-Si}(r)$) using Eq.(5.6) is 0.43×10^{-9} m^2 s^{-1}, which is slightly lower than the diffusion constant calculated using Eq.(5.5). This observation is consistent with the investigation done by Walser et. al.[39] on the validity of Stokes-Einstein behaviour where they report the diffusion coefficient of a molecule computated using Eq.(5.6) varies with the change in the mass distribution in the molecule. For a qualitative comparison we note that the self-diffusion coefficient of benzene at 298.15 K is 2.2×10^{-9} m^2 s^{-1} [40]. As the self-diffusion coefficient of a fluid is inversely related to the molar mass [41], the self-diffusion of PhTMS obtained from the simulation can be considered reasonable.

Rotational and Debye relaxation time constants.

The autocorrelation of the dipole moment rotational diffusion of the molecules is shown in Fig. (5.6). The data from the simulation are displayed as points. The correlation shows two decay time scales. The bi-exponential decay function, $f(t) = A_0 + A_1 \exp(-t/\nu_1) + A_2 \exp(-t/\nu_2)$, fitted through the data points is shown by the dotted curve. The two time constants obtained from the fit are $\nu_1 = 0.134 \pm 0.003$ ps and $\nu_2 = 20.39 \pm 0.06$ ps. The faster decay-time constant is due to the rapid fluctuations of the dipole caused by fast angular distortions between the bonds. It is not related to the overall rotation of the molecules. The slower decay-time constant ν_2 can be attributed to the decrease in correlation by the rotation of the molecules and is equal to τ_2 in Eq.(5.9). The slower decay-time constant can be compared with the rotation time constant obtained from the experiment.

The trace of the transient birefringence obtained from the OKE experiment is shown in Fig. (5.7). The two time constants obtained from the biexponential fit

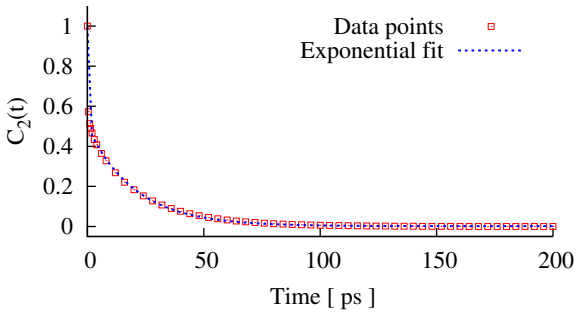

Figure 5.6: Autocorrelation of the rotational diffusion of the dipole moment of the molecules. The time constants obtained from the bi-exponential fits are $\nu_1 = 0.134 \pm 0.003$ ps and $\nu_2 = 20.39 \pm 0.06$ ps.

$f(t) = A_0 + A_1 \exp(-t/\nu_{1,ex}) + A_2 \exp(-t/\nu_{2,ex})$ done after 1 ps after the exact overlap of the pump and probe pulses are $\nu_{1,ex} = 1.58 \pm 0.03$ ps and $\nu_{2,ex} = 20 \pm 1$ ps. The fitting is done after 1 ps of the overlap to avoid the effects of the instantaneous non-linearities arising from the non-equilibrium electron cloud distortions on the results. These distortions induced by the high intensity pulses can be assumed to die out within 1 ps. Among the two observed relaxation times, the faster relaxation time, $\nu_{1,ex}$, is due to translational anisotropy and the slower relaxation time, $\nu_{2,ex}$, is due to the rotational diffusion. The rotational diffusion time of the dipole moment computed from the simulation is within the errors of the value obtained from the experiment. The Debye relaxation time approximated from the simulation is $\tau_1 = 53.4 \pm 0.6$ ps.

Thermodynamic properties

Experimental values for thermodynamic properties of PhTMS have not been reported yet. Different thermodynamic properties that have been calculated from our simulations are presented below.

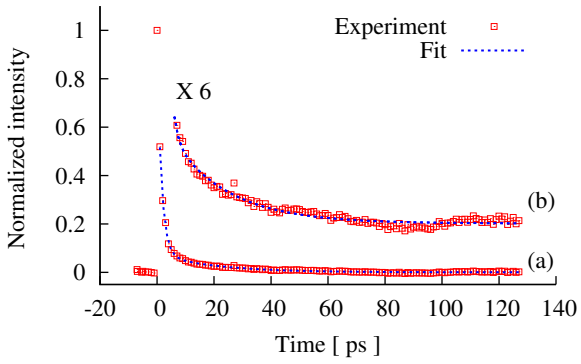

Figure 5.7: Experimentally determined trace of the transient birefringence in PhTMS (a). Part of (a) after 7 ps is magnified in (b) to show the dynamics at longer delay time. The time constants obtained from the bi-exponential fit are $\nu_{1,ex} = 1.58 \pm 0.3$ ps and $\nu_{2,ex} = 20 \pm 1$ ps. $\nu_{2,ex}$ corresponds to the average rotational diffusion time of the molecules.

Isothermal compressibility.

The volumes of the boxes used in the simulations are $V_1 = 1.1815 \times 10^{-25}$ m^3 and $V_2 = 1.1994 \times 10^{-25}$ m^3, respectively. The densities and the pressures obtained from the two simulations done at constant volume and temperature (300 K) are $\rho_1 = 1084.03$ kg m^{-3}, $\rho_2 = 1067.93$ kg m^{-3}, $P_1 = 98.38$ bar and $P_2 = -69.99$ bar, respectively. The isothermal compressibility β_T evaluated using Eq.(5.10) is 8.89×10^{-5} bar^{-1}, which is similar to the compressibility of 1.0×10^{-4} bar^{-1} computed using Eq.(5.11).

Thermal expansion coefficient.

The densities obtained from the simulations done at constant pressure and two different temperatures, $T_1 = 300$ K and $T_2 = 315$ K, are $\rho_1 = 1072.8$ kg m^{-3} and $\rho_2 = 1053.7$ kg m^{-3}, respectively. The thermal expansion coefficient α evaluated using Eq.(5.12) is 1.2×10^{-3} K^{-1}, which is very close to the value of 1.4×10^{-3} K^{-1} computed using the fluctuation formula (Eq.(5.13)).

Heat of vaporization.

The heat of vaporization is estimated using Eq.(5.14). The contribution from the inter and intra-molecular interaction is -66.7±0.4 kJ mol^{-1}. The contribution from the intra-molecular interaction is -14.1±0.4 kJ mol^{-1}. The heat of vaporization is then 55.1 ± 0.6 kJ mol^{-1}.

Specific heats C_V and C_P.

The specific heat at constant volume C_V calculated using Eq.(5.15) is 2.4×10^3 J K^{-1} kg^{-1} at 300 K and as the thermal expansion coefficient is very low the specific heat at constant pressure C_P calculated using Eq.(5.16) has the same value.

Conclusions

We have presented results of an experimental investigation of the rotational diffusion of phenyltrimethoxysilane based on the optical Kerr effect (OKE). We have also presented a new model of the molecule for MD simulations based on the OPLS force field. The model has been developed to reproduce the rotational diffusion time, density, dipole moment and dielectric constant. The viscosity is in sufficient agreement with the experimental value. As the parameters used in the model give properties of the molecule that are in good agreement with experiments, the parameters may also be used for the study of systems like functionalized inorganic surfaces, siloxane dendrimers and POSS.

Acknowledgements

The experimental work was performed in the femtosecond laboratory (Femtoland) of Jacobs University Bremen. The simulations were performed using the computational

resources of the CLAMV (Computer Laboratories for Animation, Modeling and Visualization) at Jacobs University Bremen. This work was performed under the graduate program "Nanomolecular Science" with financial support from the research center for "Functional Materials and Nanomolecular Science (NanoFUN)" at Jacobs University Bremen.

Bibliography

[1] Colvin, E. W. Silicon in Organic Synthesis; Butterworths: London, 1981.

[2] Thames, S. F.; Panjnini, K. G. *J. Inorg. Organomet. P.* **1996,** *6,* 59-94.

[3] Corder, D. B.; Lickiss, P. D.; Rataboul, F. *Chem. Rev.* **2010,** *110,* 2081-2173.

[4] Baney, R. H.; Itoh, M.; Sakakibara, A.; Suzukit, T. *Chem. Rev.* **1995,** *95,* 1409-1430.

[5] Smith, J. S.; Borodin, O.; Smith, G. D. *J. Phys. Chem. B* **2004,** *108,* 20340-20350.

[6] Ionescu, T. C.; Qi, F.; McCabe, C.; Striolo, A.; Kieffer, J.; Cummings, P. T. *J. Phys. Chem. B* **2006,** *110,* 2502-2510.

[7] Matsubara, H.; Pichierri, F.; Kurihara, K. *J. Chem. Theory Comput.* **2010,** *6,* 1334-1340.

[8] Maple, J. R.; Hwang, M.-J.; Stockfisch, T. P.; Dinur, U.; Waldman, M.; Ewig, C. S.; Hagler, A. T. *J. Comput. Chem.* **1994,** *15,* 162-182.

[9] Sun, H.; Rigby, D. *Spectrochim Acta A* **1997,** *53,* 1301-1323.

[10] Sun, H. *Macromolecules* **1995,** *28,* 701-712.

[11] Frisch, M. J.; Trucks, G. W.; Schlegel, H. B.; Scuseria, G. E.; Robb, M. A.; Cheeseman, J. R.; Montgomery, Jr., J. A.; Vreven, T.; Kudin, K. N.; Burant, J. C.; Millam, J. M.; Iyengar, S. S.; Tomasi, J.; Barone, V.; Mennucci, B.; Cossi, M.; Scalmani, G.; Rega, N.; Petersson, G. A.; Nakatsuji, H.; Hada, M.; Ehara, M.; Toyota, K.; Fukuda, R.; Hasegawa, J.; Ishida, M.; Nakajima, T.; Honda, Y.; Kitao, O.; Nakai, H.; Klene, M.; Li, X.; Knox, J. E.; Hratchian, H. P.; Cross, J. B.; Bakken, V.; Adamo, C.; Jaramillo, J.; Gomperts, R.; Stratmann, R. E.; Yazyev, O.; Austin, A. J.; Cammi, R.; Pomelli, C.; Ochterski, J. W.; Ayala, P. Y.; Morokuma, K.; Voth, G. A.; Salvador, P.; Dannenberg, J. J.; Zakrzewski, V. G.; Dapprich, S.; Daniels, A. D.; Strain, M. C.; Farkas, O.; Malick, D. K.; Rabuck, A. D.; Raghavachari, K.; Foresman, J. B.; Ortiz, J. V.; Cui, Q.; Baboul, A. G.; Clifford, S.; Cioslowski, J.; Stefanov, B. B.; Liu, G.; Liashenko, A.; Piskorz, P.; Komaromi, I.; Martin, R. L.; Fox, D. J.; Keith, T.; Al-Laham, M. A.; Peng, C. Y.; Nanayakkara, A.; Challacombe, M.; Gill, P. M. W.; Johnson, B.; Chen, W.; Wong, M. W.; Gonzalez, C.; Pople, J. A. "Gaussian 03, Revision C.02", Gaussian, Inc., Wallingford, CT, 2004.

[12] Breneman, C. M.; Wiberg, K. B. *J. Comp. Chem.* **1990,** *11,* 361-397.

[13] Jorgensen, W. L.; Tiraldo-Rives, J. *J. Am. Chem. Soc.* **1988,** *110,* 1657-1666.

[14] Jorgensen, W. L. Encyclopedia of Computational Chemistry. In , Vol. 3; Wiley: New York, 1998; Chapter OPLS, force field, pages 1986–1989.

[15] Van Der Spoel, D.; Lindahl, E.; Hess, B.; Groenhof, G.; Mark, A. E.; Berendsen, H. J. *J Comput Chem* **2005,** *26,* 1701–1718.

[16] Leeuw, S. W. D.; Perram, J. W.; Smith, E. R. *Proc. R. Soc. Lond. A* **1983,** *388,* 177-193.

[17] Ryckaert, J.-P.; Ciccotti, G.; Berendsen, H. J. C. *J. Comput. Chem.* **1977,** *23,* 327-341.

[18] Essmann, U.; Perera, L.; Berkowitz, M. L.; Darden, T.; Lee, H.; Pedersen, L. G. *J. Chem. Phys.* **1995,** *103,* 8577-8592.

[19] Hoover, W. G. *Phys. Rev. A* **1985,** *31,* 1695-1697.

[20] Parrinello, M.; Rahman, A. *J. Apply. Phys.* **1981,** *52,* 7182-7190.

[21] Nosé, S.; Klein, M. L. *Mol. Phys.* **1983,** *50,* 1055-1076.

[22] Zwanzig, R. *Annu. Rev. Phys. Chem.* **1965,** *16,* 67-102.

[23] Neumann, M. *Mol. Phys.* **1983,** *50,* 841-858.

[24] Neumann, M.; Steinhauser, O. *Chem. Phys. Lett.* **1983,** *102,* 508-513.

[25] Kulasik, P. G.; Laaksonen, A.; Svishchev, I. M. Molecular dynamics: from classical to quantum methods. In ; Elsevier Science B.V.: Amsterdam, 1999; Chapter Spatial Structure in Molecular Liquids.

[26] Allen, M. P.; Tildesley, D. J. *Computer Simulation of Liquids;* Clarendon Press: Oxford University Press, Walton Street, Oxford OX2 6 DP, 1991.

[27] Roccatano, D. *Curr. Protein Pept. Sc.* **2008,** *9,* 407-426.

[28] Hansen, J. P.; McDonald, I. R. *Theory of simple liquids;* Academic Publishers: London, 1986.

[29] Kurtović, Z.; Marchi, M.; Chandler, D. *Mol. Phys.* **1993,** *78,* 1155-1165.

[30] Fioroni, M.; Burger, K.; Mark, A. E.; Roccatano, D. *J. Phys. Chem. B* **2000,** *104,* 12347-12354.

[31] Atkins, P.; Paula, J. D. *Physical Chemistry;* Oxford University Press: Great Clarendon Street, Oxford OX2 6DP, 2006.

[32] Ho, P. P.; Alfano, R. R. *Phys. Rev. A* **1979,** *20,* 2170-2187.

[33] McMorrow, D.; Lotshaw, W. T.; Kenney-Wallace, G. A. *IEEE J. Quantum. Elect.* **1988,** *24,* 443-454.

[34] Sala, K.; Richardson, M. C. *Phys. Rev. A* **1975,** *12,* 1036-1047.

[35] Smith, N. A.; Meech, S. R. *Int. Rev. Phys. Chem.* **2002,** *21,* 75-100.

[36] Sigma-Alrich, web portal: http://www.sigmaaldrich.com.

[37] Flaningam, O. L. *The analytical chemistry of silicones;* J. Wiley & Sons, Inc.: Weinheim, 1991.

[38] Gelest, Inc., online catalogue: http://www.gelest.com/.

[39] Walser, R.; Hess, B.; Mark, A. E.; van Gusteren, W. F. *Chem. Phys. Lett.* **2001,** *334,* 337-342.

[40] McCool, M. A.; Collings, A. F.; Woolf, L. A. *J. Chem. Soc., Faraday Trans. 1* **1972,** *68,* 1489-1497.

[41] Douglas, D. C.; McCall, D. W.; Anderson, E. W. *J. Chem. Phys.* **1960,** *34,* 152-157.

Supplementary Information

Supplementary information can be obtained free of charge from http://pubs.rsc.org/en/Content/ArticleLanding/2011/CP/c1cp20349e .

Part II

Space and Time-Resolved Spectroscopy

Chapter 6

Time resolved spectroscopy

Fundamental processes like vibrations, energy transfer and charge transfer, etc. in molecular systems occur on a femto-second time scale [1]. These processes can be investigated in real time using femto-second laser pules. Such short pulses are routinely generated by mode locking [2]. Mode locking refers to the technique, by which a constant phase is imparted to the different longitudinal modes of an oscillator. A typical laser oscillator supports longitudinal modes given by

$$\omega_m = \frac{mc}{2n(\omega_m)L} \tag{6.1}$$

where ω_m is the frequency, $m \in \{0, 1, 2, ...\}$ is the mode index, c is the speed of light in vacuum, n is the refractive index and L is the length of the cavity; the product $n(\omega_m)L$ gives the effective optical length of the cavity. The spacing between two adjacent modes is given by

$$d\omega_m = \omega_{m+1} - \omega_m = \frac{c}{2n(\omega_m)L} \tag{6.2}$$

and in the case $n(\omega_m)$ is constant the difference between the frequencies is also constant and it can be denoted simply as $d\omega$. The electric field $E(t)$ of a laser with M

adjacent longitudinal modes with central frequency ω_l and field amplitude given by $\mathcal{E}(\omega)$ is a superposition of all the modes:

$$\begin{aligned} E(t) &= \sum_{m=(1-M)/2}^{(M-1)/2} \mathcal{E}(\omega) \exp\{i(\omega_l + 2m\pi d\omega)t + \phi_m\} \\ &= \exp(i\omega_l t) \sum_{m=(1-M)/2}^{(M-1)/2} \mathcal{E}(\omega) \exp\{i(2m\pi d\omega)t + \phi_m\} \end{aligned} \tag{6.3}$$

where ϕ_m is the phase of mode m. Though $E(t)$ in general is a vector quantity, here we take it as a scalar to simplify the following derivation. When the oscillator is mode-locked, ϕ_m is constant and for a gain medium with a finite spectral bandwith with typically about 10^6 cavity modes, the time domain description of the field can be approximated as

$$E(t) \propto \int_{-\infty}^{\infty} \mathcal{E}(\omega) \exp(i\omega t) dt \tag{6.4}$$

which is the Fourier transform of the frequencies in the field, and depending on the spectral bandwidth pulsed output is generated in the time-domain, with larger spectral bandwidth giving shorter pulses.

Though the energy per pulse in an amplified femto-second pulses is quite small, few millijoules, the intensity of such a pulse can be quite large, e.g. the intensity of a pulse with 1 mJ energy and duration of 150 fs focused to a spot with diameter 100 μm is about 9.5×10^{13} Wcm^{-2}. At such intensities different non-linear optical interactions can be observed and such responses can be investigated to understand the ultra-fast processes in atoms, molecules and condensed matter [3]. The experimental works presented in this thesis are done using three closely related non-linear techniques, namely, pump-probe, transient grating and optical Kerr effect.

The response of an isotropic medium perturbed by the external electric field $E(t)$ is described by the induced polarization (dipole moment per unit volume) $P(t)$:

$$\begin{aligned} P(t) =& \varepsilon_0 \sum_{n=1}^{\infty} \chi^{(n)} \cdot E^n(t) \\ =& \sum_{n=1}^{\infty} P^{(n)}(t) \end{aligned} \tag{6.5}$$

where ε_0 is the vacuum permittivity, $\chi^{(n)}$ is the n^{th}-order susceptibility and $P^{(n)}(t)$ is the n^{th}-order polarization [3]. An expression for the polarization can be derived using the semi-classical approach in which the electric field is treated classically and the medium – the system of interest – is treated quantum mechanically. The details of the derivation can be found in reference [4], here only the general concepts are outlined.

Let H_0 denote the Hamiltonian of the unperturbed system, i.e., when no external field is present. The density matrix of the unperturbed system can be written as

$$\rho^{(0)} = \sum_n p_n |\psi_n\rangle\langle\psi_n| \tag{6.6}$$

where p_n is the probability of the system being in an eigenstate $|\psi_n\rangle$. The density matrix of a system with time-independent Hamiltonian does not evolve in time. When the system is subjected to a weak time dependent external electric field the total Hamiltonian of the system at time t can be written as

$$H(t) = H_0 + E(t) \cdot \mu, \tag{6.7}$$

where μ is the dipole operator. The perturbation leads to the evolution of the density matrix in time:

$$\rho(t) = \rho^{(0)} + \sum_{n=1}^{\infty} \rho^{(n)}(t) \tag{6.8}$$

with the n^{th}-order density matrix given by

$$\rho^{(n)}(t) = \left(-\frac{i}{\hbar}\right) \int_{-\infty}^{t} d\tau_n \int_{-\infty}^{\tau_n} d\tau_{n-1} ... \int_{-\infty}^{\tau_2} d\tau_1 E(\tau_n)E(\tau_{n-1})...E(\tau_1)$$
$$U_0(t,t_0)[\mu(\tau_n),[\mu(\tau_{n-1}),...[\mu(\tau_1),\rho^{(0)}]...]]U_0^{\dagger}(t,t_0), \tag{6.9}$$

where $i = \sqrt{-1}$ is the imaginary number and $\hbar$ is the reduced Planck constant. $U_0(t,t_0)$ is the time evolution operator given by

$$U_0(t,t_0) = e^{-\frac{i}{\hbar}H_0(t-t_0)} \tag{6.10}$$

and $\mu(t)$ is given by

$$\mu(t) = U_0^{\dagger}(t,t_0)\mu U_0(t,t_0). \tag{6.11}$$

In the density matrix formalism, the n^{th}-order polarization is given by

$$P^{(n)}(t) = \langle \mu\rho^{(n)}(t)\rangle. \tag{6.12}$$

General expression for n^{th}-order polarization can be written using Equ.(6.9) and (6.12). Here, as all the techniques used in the experiments described in this thesis investigate the induced third order polarization $P^{(3)}(t)$, only the expression for $P^{(3)}(t)$ is given:

$$P^{(3)}(t) = \left(-\frac{i}{\hbar}\right)^3 \int_{-\infty}^{t} d\tau_3 \int_{-\infty}^{\tau_3} d\tau_2 \int_{-\infty}^{\tau_2} d\tau_1 E(\tau_3)E(\tau_2)E(\tau_1)$$
$$\langle \mu(t)\cdot[\mu(\tau_3),[\mu(\tau_2),[\mu(\tau_1),\rho^{(0)}]]]\rangle. \tag{6.13}$$

In the experiments where ultra-short laser pulses are used, the semi-impulsive limit is often used to simplify Equ.(6.6). In this limit, the envelope of the three pulses can be approximated by the δ-functions and their electric fields are written as

$$\begin{aligned} E(\tau_1) &= E_1\delta(t_1-\tau_1)(e^{-i(\omega_1\tau_1-k_1r)}+e^{i(\omega\tau_1-kr)}) \\ E(\tau_2) &= E_2\delta(t_2-\tau_2)(e^{-i(\omega_2\tau_2-k_2r)}+e^{i(\omega\tau_2-kr)}) \\ E_3(\tau_3) &= E_3\delta(t_3-\tau_3)(e^{-i(\omega_3\tau_3-k_3r)}+e^{i(\omega\tau_3-kr)}). \end{aligned} \tag{6.14}$$

Here the time zero is taken to be the moment when the first pulse interacts with the system. Equ.(6.14) can be used to simplify Equ.(6.13) to

$$\begin{aligned} P^{(3)}(t) &= \left(-\frac{i}{\hbar}\right)^3 E_1(t_1)E_2(t_2)E_3(t_3)\langle\mu(t)\cdot[\mu(t_3),[\mu(t_2),[\mu(t_1),\rho^{(0)}]]]\rangle \\ &= \left(-\frac{i}{\hbar}\right)^3 E_1(t_1)E_2(t_2)E_3(t_3)\langle C(t,t_1,t_2,t_3)\rangle \end{aligned} \tag{6.15}$$

The commutator relations in Equ.(6.15) give eight terms:

$$\begin{aligned} C(t,t_1,t_2,t_3) =& \mu(t)\mu(t_3)\mu(t_2)\mu(t_1)\rho^{(0)} \\ &+ \mu(t)\mu(t_2)\rho^{(0)}\mu(t_1)\mu(t_3) \\ &+ \mu(t)\mu(t_3)\rho^{(0)}\mu(t_1)\mu(t_2) \\ &+ \mu(t)\mu(t_1)\rho^{(0)}\mu(t_2)\mu(t_3) \\ &- \mu(t)\mu(t_2)\mu(t_1)\rho^{(0)}\mu(t_3) \\ &- \mu(t)\mu(t_3)\mu(t_1)\rho^{(0)}\mu(t_2) \\ &- \mu(t)\mu(t_3)\mu(t_2)\rho^{(0)}\mu(t_1) \\ &- \mu(t)\rho^{(0)}\mu(t_1)\mu(t_2)\mu(t_3). \end{aligned} \tag{6.16}$$

Each of the terms in Equ.(6.16) contribute to different non-linear interactions of the electric field with the system and they can be expressed conveniently using the double sided Feynman diagrams. The interaction on the left corresponds to the interaction on ket and the interaction on the right corresponds to the interaction on

bra. A set of the Feynman diagrams representing the first two terms in Equ.(6.16) are shown below (Fig.(6.1)). Sub-figures (a) and (b) in Fig.(6.1) show two of the possible interactions represented by the first term. In (a) the electric field with positive frequency, $E_1 e^{-i(\omega t - k_1 r)}$, promotes the ket side of the density matrix to the first excited state denoted by 1 at time t_1, at time t_2 another field with negative frequency, $E_2 e^{i(\omega t - k_2 r)}$, lowers the ket side of the density matrix to the ground state denoted by 0, at time t_3 a third field with positive frequency, $E_3 e^{-i(\omega t - k_3 r)}$, again promotes the ket to the first excited state and the response of the system at time t is shown by the dotted arrow. In (b) the field $E_2 e^{-i(\omega t - k_2 r)}$ promotes the ket to the second excited state at time t_2 and subsequent interaction with the third field $E_3 e^{i(\omega t - k_3 r)}$ lowers the ket to the first excited state. Sub-figure (c) shows one of the possible interactions contributing to the second term in Equ.(6.16).

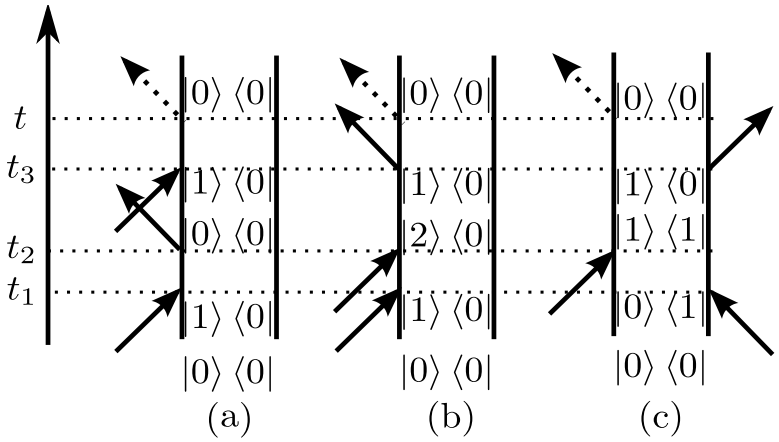

Figure 6.1: Double sided Feynman diagrams for some of the third order nonlinear interaction of light field with matter.

In a pump probe spectroscopy experiment two laser pulses are used; one pump pulse to initiate the dynamics and a time delayed probe pulse to monitor the dynamics. The Feynman diagram of excited state absorption is shown in Fig.(6.2(a)).

As shown in Fig.(6.2(a)), the pump pulse interacts with the system twice creating a population in the excited state. The probe pulse creates a coherence in the excited

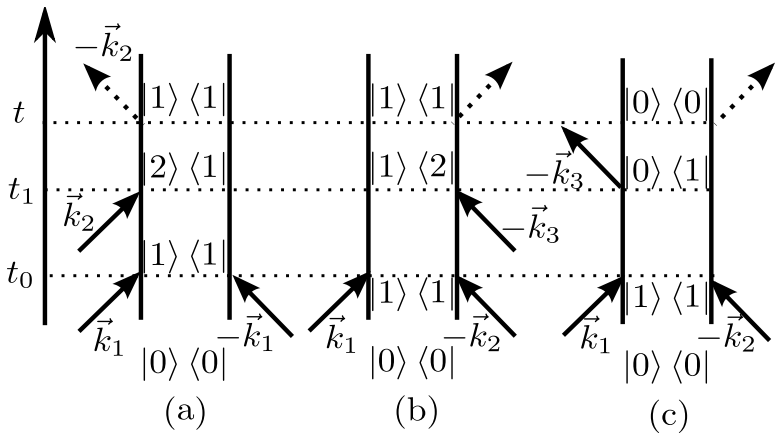

Figure 6.2: The Feynman diagrams for pump-probe (excited state absorption) spectroscopy (a) and transient gratings (b) and (c). Transient grating in (b) creates a ρ_{21} coherence while in (c) it creates ρ_{10}.

state. The generated third order polarization

$$P^{(3)}(t) \propto \mu_{10}^2 \mu_{21}^2, \tag{6.17}$$

where μ_{10} and μ_{21} represent the transition dipole moments from the ground state to the first excited state and from the first excited state to the higher excited state, respectively, overlaps with the probe pulse and is heterodyned with the probe pulse acting as the local oscillator. The schematics of the experimental setup is shown in Fig.(6.3).

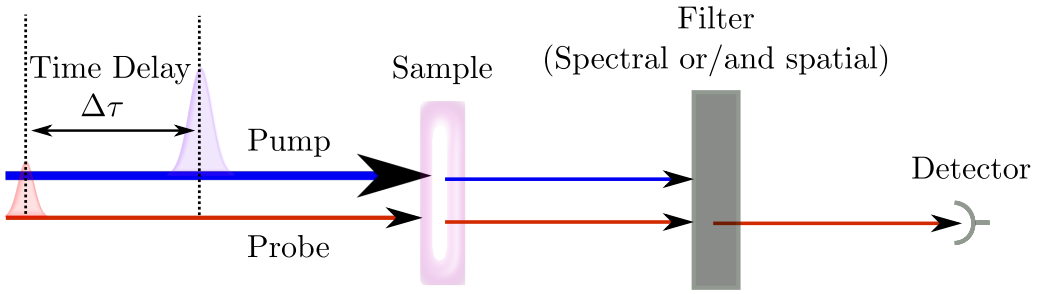

Figure 6.3: A schematic drawing of a pump-probe setup.

Fig.(6.2(b)) shows the Feynman diagram of the transient grating. The interactions of the different fields with the system is similar to that in pump-probe spectroscopy,

however, in the transient grating technique two separate pump pulses have different wave-vectors, $\vec{k}_1$ and $\vec{k}_2$, which leads to the polarization being directed into a different direction than the probe pulse – the probe pulse has the wave-vector $\vec{k}_3$ while the polarization has the wave-vector $\vec{k}_{pol_a} = -\vec{k}_1 + \vec{k}_2 + \vec{k}_3$. The wave-vector of the polarization is determined by the fact that the momentum is conserved in the interaction. The interaction of the two pump pulses in Fig.(6.2(b)) can be interchanged, which changes the wave-vector of the polarization to $\vec{k}_{pol_b} = \vec{k}_1 - \vec{k}_2 + \vec{k}_3$. Waves propagating in both the directions, $\vec{k}_{pol_a}$ and $\vec{k}_{pol_b}$ can be observed in the experiments. The schematics of the transient grating setup is shown in Fig.(6.4). Fig.(6.2(c)) shows an-

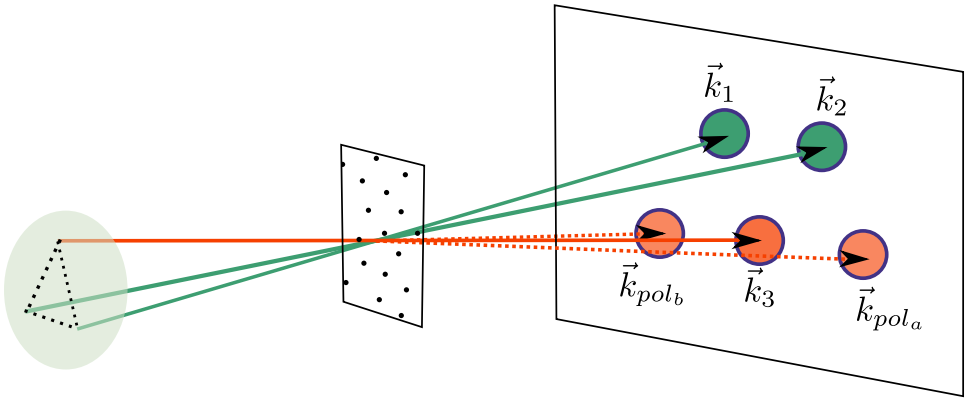

Figure 6.4: A schematic drawing of a transient grating setup.

other interaction of the three pulses, which leads to the generation of a propagating wave in the direction of $\vec{k}_{pol_a}$. The contribution of this wave to the detected signal depends on the resonance condition, i.e. if the probe pulse is resonant with the $1 \rightarrow 0$ transition. In the experiment described in Chapter 8 the probe pulse is resonant with the $1 \rightarrow 2$ transition rather than $1 \rightarrow 0$, thus the signal is predominantly due to the interaction shown in Fig.(6.2(b)).

Both the pump-probe and the transient-grating techniques have their advantages and disadvantages. The pump-probe technique is easy to implement experimentally as it requires only two beams. In the experiment presented in Chapter 7 this technique has been combined with near field optical scanning microscopy to study the exciton

dynamics in 160 nm thin layers of PTCDA on glass with 100-150 nm lateral spatial resolution. This technique, however, has as drawback that when the layer thickness is decreased, the interaction of the field with the sample decreases and the very weak signal cannot be recovered from the huge probe background because of the noise due to the fluctuations in the laser pulses. The transient grating technique overcomes this limitation as the signal does not overlap with the probe, and using this technique it has been possible to study the ultrafast dynamics of sub-nanometer thin films of PTCDA on glass. The results of this experiment are presented in Chapter 8.

Bibliography

[1] De Schryver, F.C.; De Feyter, S.; Schweitzer, G. Femtochemistry; Wiley-VCH Verlag GmbH: Weinheim, Germany, 2001.

[2] Diels, J. C.; Rudolph, W. Ultrashort Laser Pulse Phenomena; Academic Press: 84 Theobald's Road, London WC1X 8RR, UK, 2006.

[3] Boyd, R. W. Nonlinear Optics; Academic Press: 84 Theobald's Road, London WC1X 8RR, UK, 2003.

[4] Mukamel, S. Principles of Nonlinear Optical Spectroscopy; Oxford University Press: 200 Madison Avenue, New York, 1995.

Chapter 7

Pump-probe scanning near field optical microscopy (PP-SNOM): Sub-wavelength resolution chemical imaging and ultrafast local dynamics

Khadga Karki, Mahesh Namboodiri, Tahir Zeb Khan,

and Arnulf Materny

Abstract

Results of two color femtosecond time-resolved pump-probe experiments using scanning near field optical microscopy (SNOM) on thin films of organic semiconductor 3,4,9,10 Perylenetetracarboxylic dianhydride (PTCDA) are presented. With this technique quantitative information on exciton dynamics with high temporal and spatial resolution can be obtained by fitting a rate model to the transient absorption spectra. Additionally, the chemical selectivity inherent to this technique enhances the contrast which could be used for video-rate imaging when high-repetition rate lasers are used.

Scanning near-field optical microscopy (SNOM) is a powerful technique for imaging nano-objects with lateral resolution better than 100 nm using visible light [1, 2]. The technique has also been combined with time-resolved spectroscopy using a pump-

probe set up to study the ultrafast dynamics in quantum wells, wires, and dots of inorganic semiconductors [3, 4, 5, 6]. We have used a similar technique to study the exciton dynamics in 160 nm thin films of PTCDA composed of nano-crystals on glass prepared by molecular beam evaporation in ultra-high vacuum (see Fig. (1) in the Supplementary Information (SI)). The absorption spectrum of the film shows a broad band peaked around a wavelength of 490 nm (Fig. 2 in the SI), which is due to the excitation of the molecules to their first singlet (S_1) excitonic state.

In our experiments, a pump pulse with center wavelength at 520 nm was used for the excitation and the transient absorption from the S_1 state was measured with a probe pulse centered at 650 nm. The experimental setup consisted of a regeneratively amplified Ti:Sapphire laser system (CPA 2010, Clark MXR) having a repetition rate of 1 kHz, 1 mJ pulse energy, and 150 fs pulse width centered around 775 nm. The output of CPA was used to pump two optical parametric amplifiers (TOPAS, Light Conversion), one of which provided the pump and the other the probe pulse. The outputs of the OPAs wee compressed to about 80 fs pulse duration by a prism compressor setup. After traversing computer controlled delay stages, the pump and probe beams were made collinear. Finally, they were coupled into an inverted microscope (Olympus) equipped with a commercial scanning probe microscopy (SPM) system (Nanonics Multiview 2000). The sample was placed on a piezo controlled XYZ translator. The pulses were focused on to the sample with an objective lens (Olympus PLAN N 10×, NA = 0.25). The intensity of the probe beam collected by a SNOM tip attached to a tuning fork in the near field (shown in Fig. (8.1)) was recorded by an avalanche photo-diode detector (STM1DAPD10, Amplification Technologies, Inc). SNOM tips with aperture diameters of approx. 100 nm were used in the experiments. The height of the tip above the sample was kept constant with the tuning fork feed-back mechanism [7]. The pump-probe SNOM (PPSNOM) images

were taken by delaying the probe by 200 fs after the pump. The 128×128 pixels images were recorded with 1-100 ms integration time per pixel.

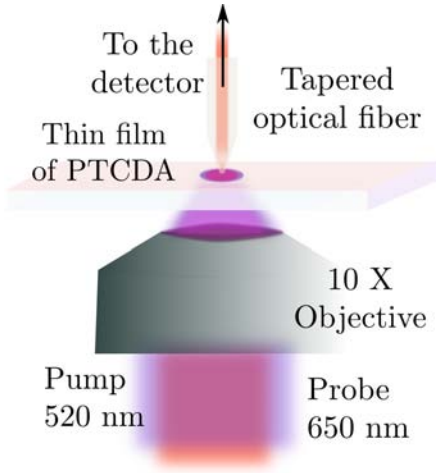

Figure 7.1: The experimental setup showing the SNOM.

Figure (7.2(a)) shows the transient absorbance for different pump intensities recorded using the SNOM tip. The time profiles of the absorbance map the population of the excitons in the S_1 state, both the free (F) excitons and the self trapped (ST) excitons. The transients are found to be different for different pump intensities. At low energies of approx. 20 pJ per pulse the decay in absorbance is mono-exponential while at higher energies the decay has more components. This can be seen from the transients obtained for 120 and 350 pJ per pulse shown in Fig. (7.2(a)). The average exciton densities at these pulse energies are $8.12 \times 10^{18}, 3.828 \times 10^{19}$, and 9.86×10^{19} cm^{-3} for 20, 120, and 350 pJ pulses, respectively. The intensity-dependent decay profiles can be modeled taking into account the following three processes: (i) exciton-exciton annihilation, (ii) relaxation of the F excitons to the ST excitons, and (iii) relaxation of the ST excitons to the ground state. The decay profiles show that exciton annihilation is discernible only for densities higher than 1×10^{19} cm^{-3}. A similar model has been used to describe exciton dynamics in β-perylene crystals [8]. In the annihilation process, the S_0, ground state, and the highly excited singlet S_N state are generated. The S_N state rapidly relaxes to the S_1 state through internal

conversion thereby reducing the number of excitons by half. The overall relaxation process can be described by the following rate equations:

$$\frac{dn_F(t)}{dt} = -k_{FS}n_F(t) - \frac{\gamma}{2}n_F(t)^2 \tag{7.1}$$

$$\frac{dn_{ST}(t)}{dt} = k_{FS}n_F(t) - k_{SG}n_{ST}(t) \tag{7.2}$$

where n_F is the population of the F excitons, k_{FS} is the rate of relaxation of the F excitons to the ST excitons, γ is the rate of annihilation, n_{ST} is the population of the ST excitons, and k_{SG} is the rate of relaxation of the ST excitons to the ground state. The transient absorbance signal can be modeled by summing the contributions from the F and ST excitons:

$$A(t) = (\varepsilon_F n_F(t) + \varepsilon_{ST} n_{ST}(t))d = (n_F(t) + \alpha n_{ST}(t))\varepsilon_F d \tag{7.3}$$

where ε_F and ε_{ST} are the absorption coefficients of F and ST excitons,respectively, d is the sample thickness, and $\alpha := \varepsilon_{ST}/\varepsilon_F$. The solution to eq. (8.1) is $n_F(t) = 2k_{FS}/[\{(2k_{FS}/n_F(0)) + \gamma\}\exp(tk_{FS}) - \gamma]$. The solution to eq. (7.2) is found numerically using the Runge-Kutta method.

We use solutions to eqs. (8.1) and (7.2), and eq. (7.3) to fit the observed time profiles of transient absorbance with the fitting parameters k_F, γ and α. $\varepsilon_F = 3.24 \times 10^4$ M^{-1} cm^{-1} is calculated from the density of excitons, the absorbance at zero time delay, and the thickness of the film. $k_{SF} = 2.1 \times 10^9$ s^{-1} is taken from literature [9]. From the fitting of the experimental data, the values of k_{FS}, γ and α are found to be $7 \pm 1 \times 10^{10}$ s^{-1}, $2.2 \pm 0.1 \times 10^{-8}$ cm^3 s^{-1} and 0.6 ± 0.05, respectively. Similar measurements done in the far field (shown in Fig. (3) in the SI) give $\gamma = 2.95 \times 10^{-8}$ cm^3 s^{-1}, which is larger than the value obtained by using the SNOM technique. The difference in the annihilation rates obtained from the measurements in the near-

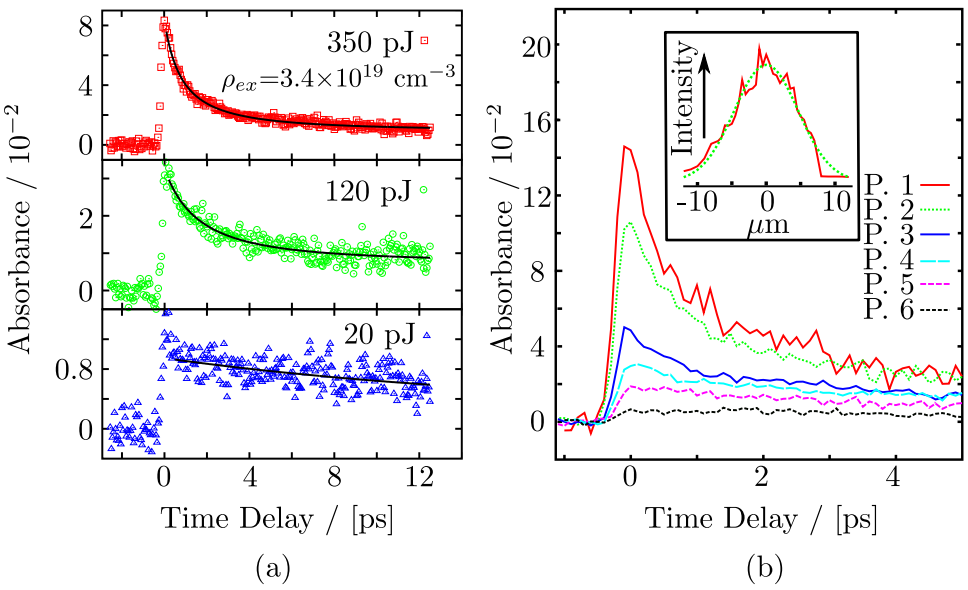

Figure 7.2: Time profile of transient absorbance at different pump intensities at the maximum of the focus spot (a) and at different points in the focus spot (b).

field and the far-field highlight the importance of the SNOM technique in obtaining accurate information about the exciton dynamics. As shown in Fig. (7.2(b)), the profiles of the transient absorbance recorded using the SNOM at different positions within the focus area are different, which is because the intensity of the pulse over the focus is not uniform, but is best described by a Gaussian distribution function; the intensity profile over the focus scanned by the SNOM is shown in the inset. The exciton densities, which are proportional to the intensity of the beam, at the different positions in the focus area are different. As a result, the transient absorbance recorded in the far-field is averaged over different decay profiles. As seen in our measurements, using the average exciton density to calculate the annihilation constant from the absorbance profile overestimates the annihilation constant.

We also used the PP-SNOM technique to image the thin films. Compared to AFM imaging, which gives topographical information only, PP-SNOM also gives chemical information of the specimen investigated. In case of PTCDA thin films, PP-SNOM can be used to image the population of excitons, which is not possible with either

AFM or conventional SNOM. Figs. (7.3(a)) and (7.3(b)) show the PP-SNOM and AFM topography image taken using the SNOM tip during the scanning of the edge of the 160 nm film of PTCDA on glass. In the PP-SNOM image, the intensity of the probe beam, delayed by 200 fs after the pump, is recorded to image the F excitons in the film. The left part in the PP-SNOM image, where the intensity of the probe beam is high, is the glass surface and the right part, where the intensity of the probe beam is low due to the absorption by the F excitons, is the film. The glass surface and the PTCDA film are also distinguishable in the AFM image, however the resolution of the AFM image is worse than that of the PP-SNOM image. The better resolution in the PP-SNOM image is due to two reasons: the aperture that collects the evanescent field in the SNOM tip is smaller than the tip itself and the PP-SNOM image is less affected by the drifts in the voltage feedback used to actuate the piezo scanner during the scanning process, which reduce the resolution of the AFM.

We have also investigated the performance of the PP-SNOM *vs.* conventional SNOM. Figs. (7.4(a)) and (7.4(b)) show the images of the film using the PP-SNOM and the change in OD of the probe beam alone (conventional SNOM), respectively. The images were taken using single shots of the probe pulse per pixel. The glass on the left and the PTCDA film on the right side of the image are clearly visible in the PP-SNOM while, apart from the edge effects from surface inhomogeneities [10], such distinction is not clear in the conventional SNOM image. It is interesting to note that images are taken with a single laser shot per point and that the energies required to take the images are very low – 500 pJ pump and 10 pJ probe in our example. Such pulse energies are readily available from a high repetition rate oscillator (100 MHz and higher), which could be used to take a 512×512 pixel image in only 3 ms provided the scanners can be actuated at high frequencies. Video-rate imaging would be possible with such a system. The use of high repetition laser systems has another advantage.

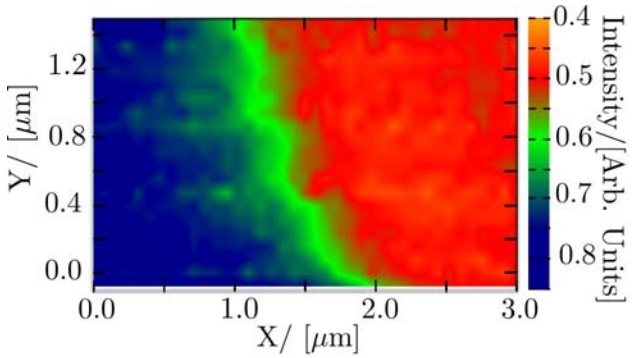

(a) PP-SNOM image

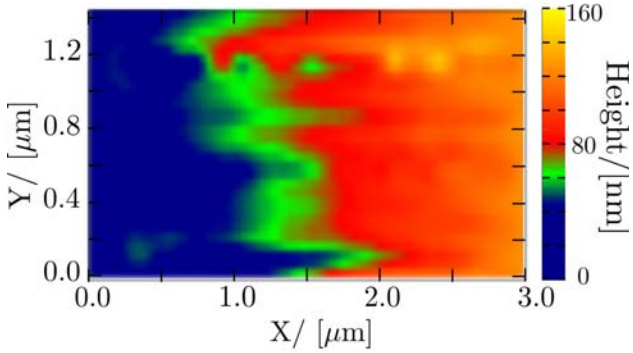

(b) AFM topography

Figure 7.3: SNOM images of the 160 nm film of PTCDA using transient absorption (a) and AFM image (b).

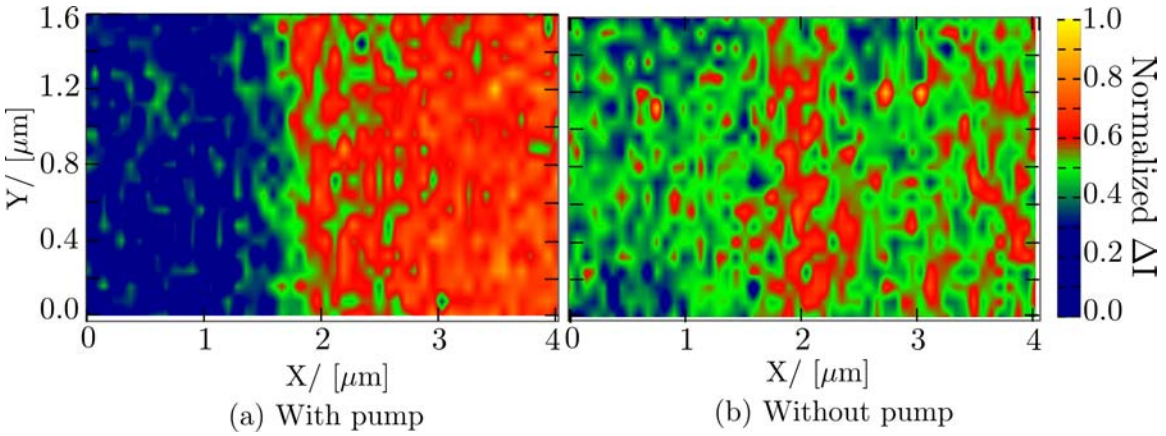

(a) With pump (b) Without pump

Figure 7.4: SNOM images of the 160 nm film of PTCDA using transient absorption with single laser shots per point (a) and using only the probe pulse (b).

The energy per pulse used for transient absorbance measurements can be reduced further.

The transient absorption signal depends linearly on the intensity of the pump and the probe pulses, $S \propto I_{pump} I_{probe}$. When a laser system with the repetition rate of f kHz is used instead of 1 kHz, the intensity of the pump and the probe can be simultaneously scaled down to $I_{pump}/\sqrt{f}$ and $I_{probe}/\sqrt{f}$, respectively, to get the same integrated signal.Based on the lowest pulse energy of only 20 pJ at 1 kHz repetition rate, with which we have been able to record dynamics, we estimate that a 100 MHz oscillator could enable recording the dynamics with pulses having only 70 femto-joule pulse energy. Exciton dynamics studied with such low pulse energies better approximate the actual dynamics in the usual lighting conditions.

In summary, the two color pump-probe measurements done using a SNOM show intensity-dependent exciton dynamics at exciton densities higher than 10^{19} cm^{-3}, which can be attributed to exciton-exciton annihilation. From the time profiles of the transient absorbance we were able to calculate the annihilation rate of the excitons. Comparison of the results with the measurements done in the far-field revealed that the annihilation constant obtained from those measurements is overestimated. Our measurements also show that the pump-probe SNOM gives better image contrast than the conventional SNOM and a single laser shot per pixel is good enough for imaging. We note that SNOM with high repetition rate laser systems can significantly speed up the imaging and also enable pump-probe measurements with very low, few femto-joule, pulse energies.

Acknowledgments

Financial support from NanoFun-Center, Jacobs University Bremen and DFG (MA-17 Femto-opt.Nahfeld) is gratefully acknowledged. Authors thank Gesa Helms and

Prof. Jürgen Fritz for the high resolution AFM images of the thin films and Prof. Veit Wagner for the help in preparing the thin films.

Bibliography

[1] Pohl, D. W.; Denk, W.; Lanz, M. *Appl. Phys. Lett.* **1984,** *44,* 651-653.

[2] Lewis, A.; Issacson, M.; Harootunian, A.; Murray, A. *Ultramicroscopy* **1984,** *13,* 227-231.

[3] Levy, J.; Nikitin, V.; Kikkawa, J. M.; Cohen, A.; Samarth, N.; Garcia, R.; Awschalom, D. D. *Phys. Rev. Lett.* **1996,** *76,* 1948-1951.

[4] Smith, S.; Holme, N. C. R.; Orr, B.; Kopelman, R.; Norris, T. *Ultramicroscopy* **1998,** *71,* 213-223.

[5] Achermann, M.; Nechay, B. A.; Morier-Genoud, F.; Schertel, A.; Siegner, U.; Keller, U. *Phys. Rev. B* **1999,** *60,* 2101-2105.

[6] Guenther, T.; Lienau, C.; Elsaesser, T.; Glanemann, M.; Axt, V. M.; Kuhn, T.; Eshlaghi, S.; Wieck, A. D. *Phys. Rev. Lett.* **2002,** *89,* 057401-1-4.

[7] Betzig, E.; Finn, P. L; Weiner, J. S. *Appl. Phys. Lett.* **1992,** *60,* 2484-2487.

[8] Yago, T.; Tamaki, Y.; Furube, A.; Katoh, R. *Phys. Chem. Chem. Phys.* **2008,** *10,* 4435-4441.

[9] Engel, E.; Leo, K.; Hoffmann, M. *Chem. Phys.* **2006,** *325,* 170-177.

[10] Hecht, B.; Sick, B.; Wild, U. P.; Deckert, V.; Zenobi, R.; Martin, O. J. F.; Pohl, D. W. *J. Chem. Phys.* **2000,** *112,* 7761-7774.

Supporting Information

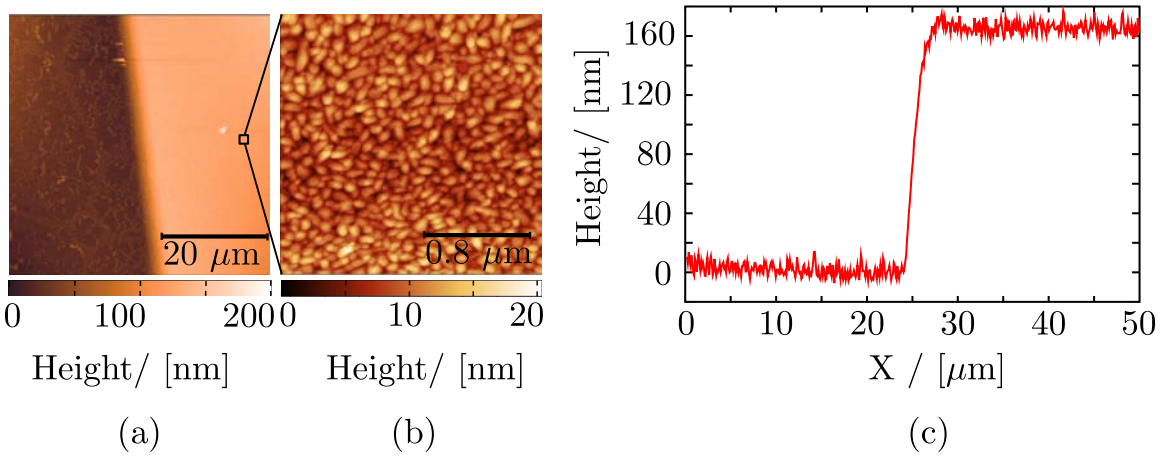

Figure 7.5: AFM image of the edge of PTCDA layer on glass (a), image of nanocrystals of PTCDA on the layer taken with high resolution AFM (b) and height profile of the layer (c)

.

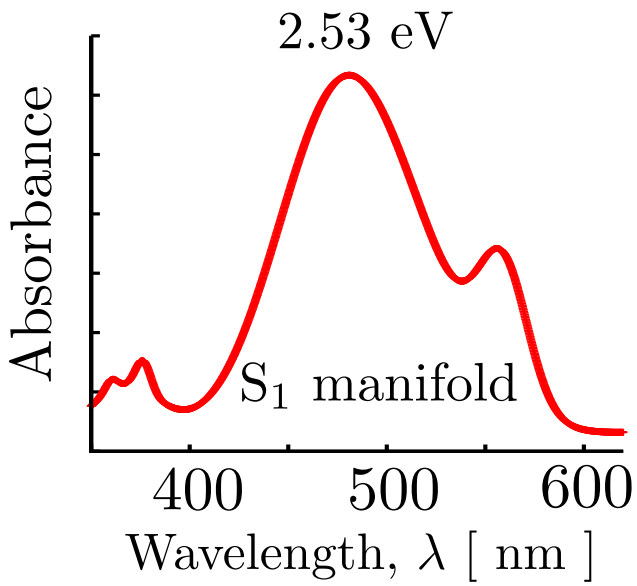

Figure 7.6: Absorption spectra of 160 nm thin film of PTCDA on glass.

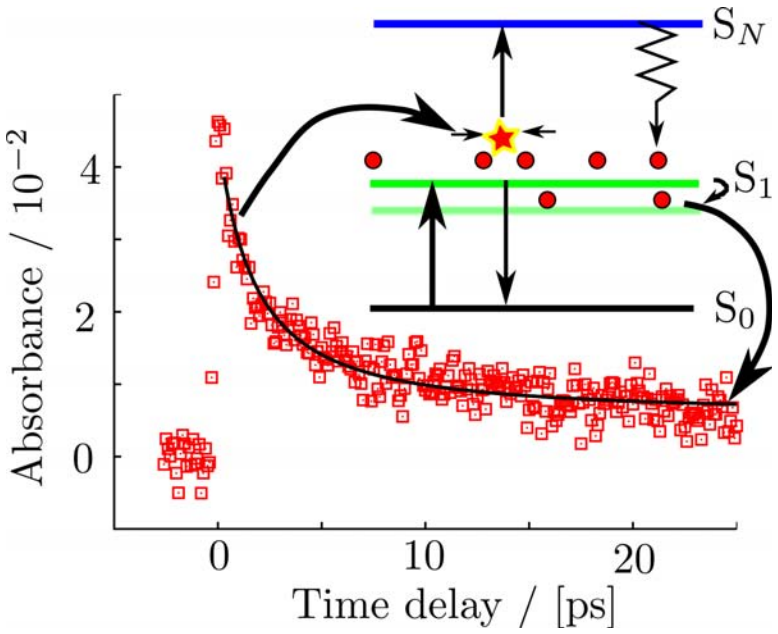

Figure 7.7: Transient absorbance of PTCDA film recorded in the far field. Illustration also shows the different processes in exciton dynamics.

Chapter 8

Transient Grating Studies of Femtosecond Processes in Ultra-Thin Layers of PTCDA

K. Karki, G. Helms, M. Namboodiri, V. Wagner,

J. Fritz, and A. Materny[1]

Abstract

Elementary processes like energy transfer, charge transport, and exciton diffusion in thin films occur on time scales of femtoseconds. So far time-resolved photo-electron spectroscopy [1, 2], a technique limited to specialized ultra-high vacuum environment and proper choice of substrate, has been used to study ultrafast processes in sub-nanometer thin films. Here, we show that a transient (population) grating [3] created by the interference of laser pulses can be used to study the ultrafast processes in such films in ambient conditions. Our investigation of exciton dynamics in 1.4±0.2 and 0.4±0.2 nm thin films formed by nano-crystals of 3,4,9,10-Perylenetetracarboxylic dianhydride (PTCDA) on glass and mica shows that the dynamics differs with the crystal size, possibly due to the confinement induced changes in the electronic structure. The technique is sensitive enough to investigate the dynamics in systems where only 20% of the surface is covered by the nano-crystals. We expect that an optical

[1]This chapter is reproduced without modification from the article which has been accepted for publication in *Chem. Phys. Chem.*

technique sensitive enough to study dynamics in few to sub-nanometer thin layers in ambient condition will be important in investigating ultrafast dynamics on surfaces, interfaces, functionalized materials, organic semiconductors, and quantum phenomena in ordered structures of reduced dimensions like quantum dots and graphene sheets.

Introduction

Diffraction based techniques were first used by Zu et al. to study the diffusion of adsorbates on surfaces at monolayer [4] coverage and later by Reider et al. at submonolayer [5] coverages. In their work, holographic gratings were created by laser-induced desorption (LID) of an adsorbed layer by two pulsed laser beams intersecting on the surface [4]. Then the second harmonic of a third laser pulse diffracted by such a grating was used to investigate changes in the grating induced by the diffusion of the adsorbate molecules. Though the diffusion dynamics investigated in those experiments lasted hundreds of seconds the technique was sensitive enough to monitor molecular diffusion on surfaces at sub-monolayer coverages.

Gratings can also be created by a periodic arrangement of optically excited and relaxed molecules on a surface. When two coherent laser beams interfere, the molecules in the bright zones will be in an excited state and will have different optical properties than the molecules in the dark zones which are in their ground state. When the gratings are created by the interaction of two ultrashort pulses (pump pulses) in the sample with wavevectors $\vec{k}_1$ and $\vec{k}_2$ a third pulse (probe pulse) with wavevector $\vec{k}_3$ gets diffracted in the phase matched directions $\vec{k}_s = \vec{k}_2 - \vec{k}_1 + \vec{k}_3$ and $\vec{k}'_s = \vec{k}_1 - \vec{k}_2 + \vec{k}_3$ (Fig.(8.1)). Such gratings are known as transient gratings as the grating pattern smears out with time due to molecular processes like the relaxation of the excited state [3]. Thus various ultrafast processes occurring in the molecules can be studied

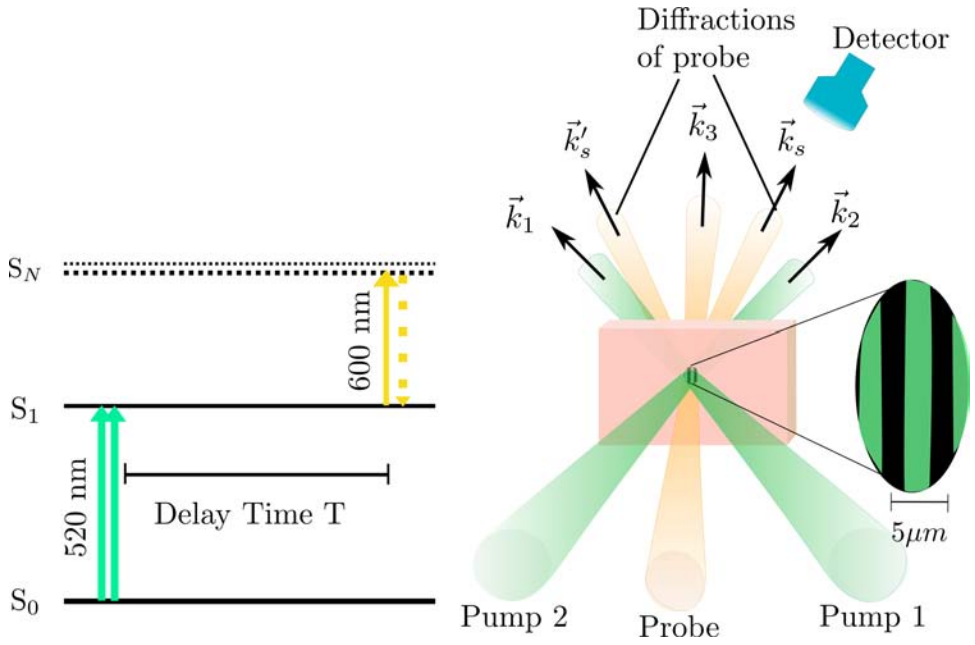

Figure 8.1: The energy level diagram of PTCDA(left) and the beam geometry (right) of the time-resolved transient grating experiment. Two time coincident beams (Pump 1 and Pump 2) resonant with the $S_0 \rightarrow S_1$ transition and wavevectors $\vec{k}_1$ and $\vec{k}_2$ interact with the sample creating a population grating. A third beam (Probe) resonant with $S_1 \rightarrow S_N$ transition and wavevector $\vec{k}_3$ is diffracted by the grating in the phase matched directions $\vec{k}_s = -\vec{k}_1 + \vec{k}_2 + \vec{k}_3$ and $\vec{k}_{s'} = \vec{k}_1 - \vec{k}_2 + \vec{k}_3$. The effective grating constant for the beam geometry used in the experiment is about $5\mu m$. The diffracted signal $\vec{k}_s$ is monitored in our experiments.

simply by investigating the smearing out of the grating. This technique has been applied to study dynamics in quantum dots in solution [6] and films thicker than 40 nm on substrates [7]. Our experiments show that, like in the case of physical gratings induced by LID [4], transient gratings could be applied to study ultrafast dynamics in molecular adsorbates on surfaces at sub-nanometer thin coverage.

Results and Discussions

We have investigated the relevance of the method in very thin films of PTCDA, an archetypal organic semiconductor, which forms well-ordered layers on a variety of substrates [8, 9, 10, 11]. We used thin films (Fig.8.2) of PTCDA showing nanometer sized islands when grown by molecular beam deposition on transparent substrates

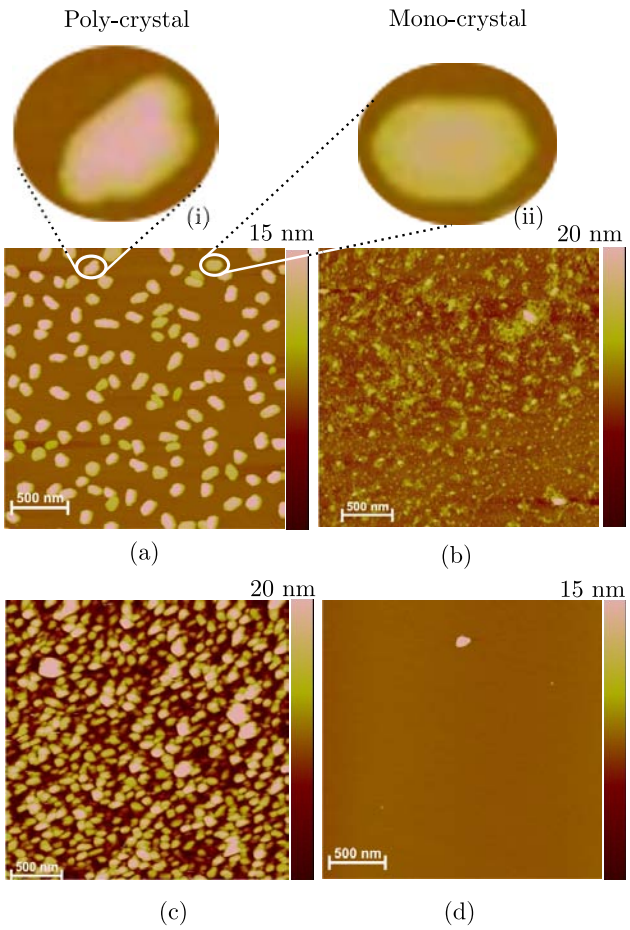

Figure 8.2: AFM images of the thin films of PTCDA investigated in this work: 1.4 nm film on mica (a), 1.4 nm film on glass (b), 100 nm film on glass (c) and 0.4 nm film on mica (d) as determined by QCM. In (a) the film consists of about 100 nm long nano-crystals. Both poly-crystals (an example is shown in inset (i)), and mono-crystals with six sharp faces (an example is shown in inset (ii)) are found on the surface. The average height of the crystals is about 7 nm and they cover roughly a quarter of the surface. In (b) the crystals are much smaller and their sizes are more dispersed. In (c) the surface roughness of the glass is not visible, showing that multiple layers of crystals are produced and the average crystal size is larger than in (b). In (d) sparsely distributed nano-crystals are observed.

such as mica or glass. The film thickness was determined by a quartz crystal microbalance (QCM) and the morphology of the films was investigated by atomic force microscopy (AFM). In 1.4 nm thick films on mica about 20% of the surface is covered by islands of PTCDA with a diameter about 100 nm and an average height of about 7 nm (Fig.8.2(a)). The islands in our films show similar features as PTCDA films on hydrogen-terminated Si(111) by Sazaki *et al.* [12] The Volmer-Weber growth mode is assumed for the growth of islands as they consist of monocrystals (with six sharp facets as shown in inset (ii) in Fig.(8.2)) [13] as well as poly-crystals (shown in inset (i) in Fig.(8.2)) formed by the coalescence of smaller crystals. About 41% of the islands observed in the AFM image are mono-crystals indicating that Oswald ripening, a phenomenon in which a larger crystal grows by "eating up" smaller ones, occurs during the layer growth [12]. On glass the surface roughness (RMS roughness of about 5 nm as determined by AFM) hinders the diffusion of the molecules resulting in the formation of much smaller, but densely distributed islands (Fig.8.2(b)). Sparsely distributed islands are observed in a 0.4 nm layer on mica (Fig.8.2(c) shows only three islands of PTCDA on an area of 4 μm^2) while no islands or crystals are visible on a similar layer on glass. A uniform layer of 0.35 nm thickness corresponds to a monolayer of PTCDA.

The absorption spectrum of thin films of PTCDA (thickness $>$ 10 nm) has a narrow peak at $E = 2.23$ eV and a broad feature at $E > 2.3$ eV which have been explained as the excitation to the S_1 excitonic levels [8]. The proposed electronic structure of the PTCDA crystals, which is also supported by electroabsorption spectra, shows a strong mixing of Frenkel and charge transfer exciton [15, 16, 17] because of which a multi-exponential relaxation dynamics of the excited state can be expected. Such dynamics have been observed in the pump-probe experiments done by Engel *et al.* on 20 nm films of PTCDA [18, 19]. Similar experiments, using a simple pump-probe technique, have not been done on few nanometer or sub-nanometer layers mainly

because the pump-probe technique, which measures the change in the optical density (OD), is not sensitive enough to investigate dynamics of such thin films as the change in the OD is very small compared to the huge probe background. This limitation is eliminated in a grating based technique reported here where the sideward diffracted laser signal is spatially separated from the probe laser beam.

Formation of a transient grating is a non-linear process which depends on the third order susceptibility, $\chi^{(3)}$, of the medium describing its response to electric fields. In our experiments two time-coincident laser pulses (pump beams), with a duration of about 70 fs, energies of 9 nJ and a wavelength centered around 520 nm for exciting $S_0 \rightarrow S_1$ transition, were focused onto the PTCDA films to create gratings with an approximate grating constant of 5 μm. A third laser beam (probe beam), with a duration of about 80 fs and an energy of about 3 nJ was then diffracted by the grating. The wavelength of the third pulse was centered around 600 nm, which is in resonance with $S_1 \rightarrow S_N$ transition, to selectively study the relaxation dynamics of the population of the S_1 state. The spectrum of one of the diffracted signals $\vec{k}_s$ was recorded and the time dependence of the signal intensity at 600 nm was analysed.

First we investigated the diffracted signal from a 70 nm PTCDA film on glass which is visible to the naked eye. The signal intensity at 600 nm at different delay times between the pump beams and the probe beam shows a multi-exponential decay (Fig.8.3 (a)). The initial fast bi-exponential decay is clearly visible in the figure and the slow decay is shown in inset (i) on a longer time scale. Such a multi-exponential decay has been attributed in literature to exciton-exciton interaction and annihilation in PTCDA at excitation densities higher than 5×10^{18} cm^{-3} [19]. Since in our experiment the excitation density is about 1.0×10^{20} cm^{-3} we assume similar mechanism. In addition, inset (ii) in Fig.8.3 shows that the maximum intensity of the diffracted signal is delayed by about 100 fs after time zero. Such a delay has been observed previously in 20 nm films and it has been attributed to the ultrafast intraband relaxation

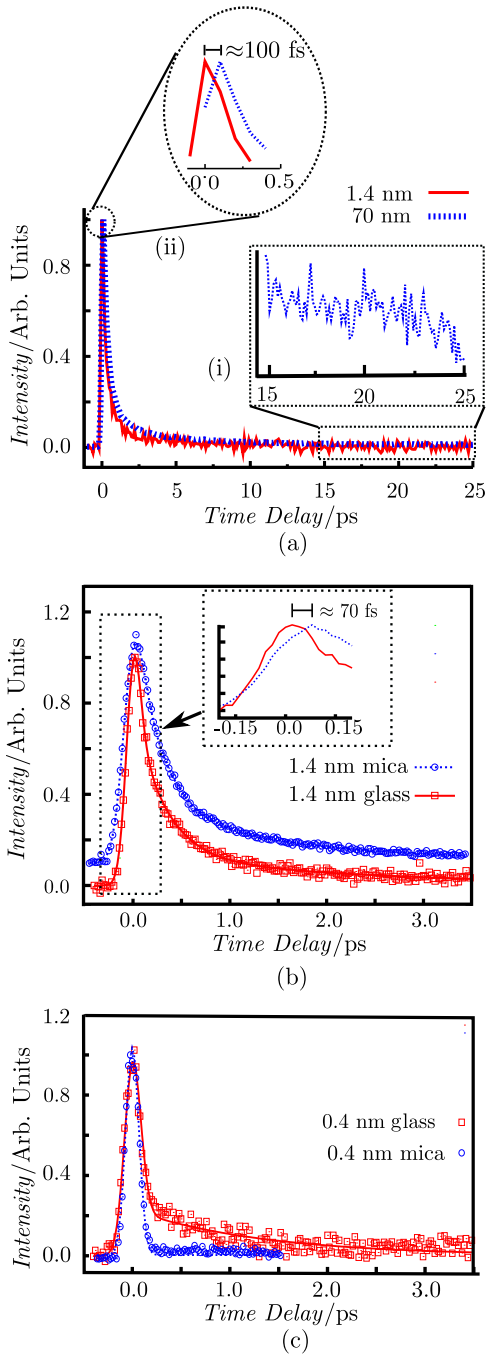

Figure 8.3: Intensity of the diffracted signal *vs.* delay time for 70 nm and 1.4 nm thin PTCDA films on glass (a), 1.4 nm thin films on glass and mica (b) and 0.3 nm thin films on glass and mica (c). The transients show a multi-exponential decay behavior, a fast initial decay followed by a slow decay for 70 nm and 1.4 nm thin films (a,b) and a mono-exponential decay for 0.4 nm thin film on glas (c). 0.4 nm thin film on mica shows only the non-resonant background (c).

of the initially excited state to the border of the Brillouin zone of nanocrystals [18]. Compared to the 70 nm film the delay is less pronounced in the 1.4 nm PTCDA film on glass indicating that the difference in delay could be related to the size or/and the arrangement of the islands on the surface – islands in the 1.4 nm film are substantially smaller than the 70 nm film, and they form single layer in the 1.4 nm film while in the 70 nm film they form multiple layers. A more detailed analysis of the transients from the 1.4 nm films on mica and glass hints that the difference in the rise time is mainly due to the difference in the crystal sizes.

Transients of 1.4 nm films on mica and glass, shown in Fig.(8.3)(b), are modeled as a convolution of a multi-exponential function with a Gaussian instrument response:

$$S(t) = \begin{cases} A \exp\left(-\frac{t^2}{2\tau_0^2}\right) & \text{if } t < 0 \\ A \exp\left(-\frac{t^2}{2\tau_0^2}\right) + \int\limits_{-\infty}^{\infty} dt' \exp\left(-\frac{(t-t')^2}{2\tau_0^2}\right) \sum\limits_{i=1}^{N} B_i \exp\left(-\frac{t}{\tau_i}\right) & \text{if } t \geq 0 \end{cases} \tag{8.1}$$

where τ_0 is a measure of the instrument response time. Three exponential functions with relaxation times $\tau_i, i = 1, 2, 3$ are needed to fit the transients of 1.4 nm films while only one exponential function is used in the case of a 0.4 nm film on glass. The first term in the signal, the Gaussian function, describes the non-resonant background from the substrate. In the 1.4 nm thick PTCDA films the three time constants for the exponential decays obtained from the model are 90 ± 50 fs, 240 ± 27 fs and 1.64 ± 0.07 ps for mica, and 19 ± 6 fs, 300 ± 22 fs and 2.33 ± 0.3 ps for glass. The prefactors to the first exponential decay are negative meaning that this time constant is assigned to the delay in the rise of the signal due to the intraband relaxation. The rise time agrees well with the size-dependent delayed rise mentioned before. The deviation of the observed decay from a single exponential – here it can only be modeled by a bi-exponential – provides further evidence for the exciton-exciton annihilation [19]. The differences in the time constants are most likely also due to the different sizes

of the crystals influencing the electronic properties of the PTCDA films. To date, no other studies have been conducted on PTCDA layers by changing the size or the morphology of the islands. However, such size dependent relaxation of the excitonic excitations have also been reported for thin films of GaAs [20].

Compared to the previous 1.4 nm PTCDA layers we found in an only 0.4 nm thick film of PTCDA on glass a single exponential decay of the diffracted signal (Fig.8.3 (c)) which is most likely due to the prevalence of monolayer islands on the surface. Exciton diffusion in PTCDA films, which is described by a one-dimensional diffusion model with the diffusion along the stacking direction of the layers [19], is hindered in monolayer structures. In this case the relaxation of the excited state to the ground state takes place by vibrational coupling. As seen in Fig.(8.3 (c)), the diffracted signal in the 0.4 nm film on mica can be modeled as a Gaussian centered at time zero, and it is due to the non-resonant contribution from the substrate. Surprisingly, there is no indication of dynamics in the films on mica, but this can be related to the structure of the film. Since the PTCDA film on mica has only sparsely distributed islands covering less than 2% of the surface as seen on a 4 μm^2 area in Fig.(8.2). This is not sufficient to form an effective grating when the interference fringes are separated by about 5 μm. On the other hand, the diffracted signal from the 1.4 nm film on mica indicates that a 20% surface coverage is sufficient enough to form a transient grating and observe dynamics. This shows that transient grating technique is also sensitive to the structure and coverage of the thin films on surfaces. The grating constant can be controlled by changing the focal length – larger focal length results in larger grating constants – which provides the means to control the structure sensitivity of the technique. It would be interesting to investigate if the technique can be developed to study the percolation of islands of the molecular crystals on the surfaces.

Conclusions and Outlook

The observations reported here demonstrate that transient gratings can be used to study the dynamics with femtosecond time resolution of only a few angstrom thick films. Our results provide evidence to the fact that the exciton relaxation dynamics of PTCDA layers is affected by the size of the PTCDA islands. Dynamics typical to monomers and aggregates have been observed depending on the thickness of the layers. The gratings are also sensitive to the distribution of the islands on the surfaces. The effects of different factors, like the size and height of the islands, surface coverage and stacking, in the exciton mobility in nano-crystals, which have not been accessible to investigation hitherto in ambient conditions, could be studied using the technique. The technique can also be extended to optical two-dimensional spectroscopy [21] providing full information related to the third order non-linear response from the investigated systems, which is important in understanding of the coherent and incoherent processes [22] in ultra-thin films and nano-structures. The investigation of phenomena like coherent charge transport in nanometer and sub-nanometer thin films with respect to morphology and thickness is important in understanding the charge separation processes in hetero-junctions, which is crucial in designing highly efficient systems for photovoltaics and molecular electronics.

Experimental Section

Sample preparation: 97% pure PTCDA was purchased from Aldrich (Germany). Thin films were prepared by organic molecular beam deposition at 350°C at 5.0×10^{-7} mbar pressure on cleaned glass substrates and freshly cleaved mica plates. The thickness of the layers was monitored by a calibrated QCM. The calibration was done by measuring the actual thicknesses of the layers using an AFM. The morphologies of

PTCDA layers were investigated by AFM using a Multimode AFM with a Nanoscope IIIa controller (Veeco, Germany) operated in tapping mode in air.

Time resolved measurements: Short laser pulses with a pulse length of approx. 150 fs, a center wavelength at 770 nm, and an average pulse energy of 1 mJ were obtained from a commercially available chirped pulse amplification system (CPA 2010, from Clark-MXR, Inc.). The wavelengths needed for the experiment were generated using optical parametric oscillators (OPAs). For this, the CPA output was split into two equal energy pulses to pump two traveling wave OPAs (TOPAS, from Light Conversion Ltd.). One OPA was tuned to 520 nm, while the other one emitted pulses centered at 600 nm. The pulses were compressed using pairs of prisms. The pulse duration were checked by an autocorrelator based on second harmonic generation. The beam at 520 nm was split into two using a 50:50 beam splitter and the resulting pulses were focused onto the sample with a 15 cm focal length lens to generate the population grating. The time delay between these pulses was set to zero using a motor driven delay stage in a Michelson interferometer setup. The pulses at 600 nm were time delayed with respect to the two pump pulses to record the time-dependent changes in the grating using a similar setup and also focused onto the sample using the 15 cm lens. The diffraction of the third beam was collimated with another 15 cm focal length lens and was then analyzed using a spectrometer (TRIAX 180, from HORIBA Jobin Yvon). The wavelength integrated intensities from 599 to 601 nm were used in the data analysis.

Bibliography

[1] Scholl, A.; Baumgarten, L.; Jacquemin, R.; Eberhardt, W. *Phys. Rev. Lett.*,**1997**, *79,* 5146–5149.

[2] Schwalb, C. H; Marks, M.; Sachs, S.; Schöll, A.; Reiner, F.; Umback, E.; Höfer, U. *Eur. Phys. J. B*, **2010**, *75,*, 23–30.

[3] Mukamel, S. Principle of nonlinear optical spectroscopy; Oxford University Press: 200 Madison Avenue, New York, New York, 1995.

[4] Zhu, X. D.; Rasing, T.; Shen, Y. R. *Phys. Rev. Lett.*, **1988**, *61,* 2883–2885.

[5] Reider, G. A.;Höfer, U.; Heinz, T. F. *Phys. Rev. Lett.*, **1991**, *66,* 1884–1997.

[6] Huxter, V. M.; Scholes, G. D. *J. Chem. Phys.*, **2010**, *132,* 104506.

[7] Dao, L. V.; Davis, J.; Hannaford, P.; Cho, Y. H.; Green, M. A.; Cho, E. C. *Appl. Phys. Lett.*, **2007**, *90,* 81105.

[8] Forrest, S. R. *Chem. Rev.*, **1997**, *97,* 1793–1896.

[9] Hauschild, A.; Karki, K.; Cowie, B. C. C.; Rohlfing, M.; Tautz, F. S.; Sokolowski, M. *Phys. Rev. Lett.*, **2005**, *94,* 036106.

[10] Kaiser, R.; Friedrich, M.; Schmitz-Hübsch, T.; Sellam, F.; Kampen, T. U.; Leo, K. D. R. T. Zahn, *Fresenius J. Anal. Chem.*, **1999**, *363,* 189–192.

[11] Ludwid, C.; Gompf, B.; Glatz, W.; Petersen, J.; Eisenmenger, W.; Möbus, M.; Zimmermann, U.; Karl, N. *Z. Phys. B - Condensed Matter*, **1992**, *86,* 397–404.

[12] Sazaki, G.; Fujino, T.; Usami, N.; Ujihara, T.; Fujiwara, K.; Nakajima, K. *J. Cryst. Growth*, **2005**, *273,* 594–602.

[13] Sazaki, G.; Fujino, T.; Sadowski, J. T.; Usami, N.; Ujihara, T.; Fujiwara, K.; Takahashi, Y.; Matsubara, E.; Sakurai, T.; Nakajima, K. *J. Cryst. Growth*, **2004**, *262,* 196–201.

[14] Vragović, I.; Scholz, R. *Phys. Rev. B*, **2003**, *68*, 155202.

[15] Hennessy, M. H.; Soos, Z. G.; Pascal, R. A.; Girlando, A. *Chem. Phys.*, **1999**, *245,* 199–212.

[16] Hoffmann, M.; Soos, Z. G. *Phys. Rev. B*, **2002**, *66,* 024305.

[17] Mazur, G; Petelenz, P.; Slawik, M. *J. Chem. Phys.*, **2003**, *118,* 1423–1432.

[18] Engel, E.; Koschorreck, M. K.; Leo, K.; Hoffmann, M. *Phys. Rev. Lett.*, **2005**, *95,* 157403.

[19] Engel, E.; Leo, K.; Hoffmann, M. *Chem. Phys.*, **2006**, *325,* 170–177.

[20] Akiyama, K.; Tomita, N.; Nishimura, T.; Nomura, Y.; Isu, T.; Ishihara, H.;Cho, K. *Physica B*, **2002**, *314,* 293-296.

[21] Jonas, D. M. *Annu. Rev. Phys. Chem.*, **2003**, *54,* 425–463.

[22] Engel, G. S.; Calhourn, T. R.; Read, E. L.; Mančal, T.; Cheng, Y. C.; Blankenship, R. E.; Fleming, G. R. *Nature*, **2007**, *446,* 782–786.

Chapter 9

Summary and Outlook

The works presented in this thesis describe the computational and experimental investigation of stuctural and dynamic properties of molecules and molecular nano-aggregates of different organic molecules, *viz*; ChlA, AXT, PhTMS and PTCDA.

ChlA is a representative molecule of a large number of chlorophylls and AXT is a representative molecule of hundreds of different carotenoids found in the plants and animals. MD simulations and QM calculations done to study interaction of ChlA with three different solvent molecules – water, methanol and benzene – show that the structural and dynamic properties of ChlA differ in the different solvent environments. The simulations also show formation of dimers in benzene and larger aggregates in water but only monomeric structures in methanol. The structure of the aggregates show that the dimer formation in benzene is due to the interaction of ester C=O group of one of the molecule with the Mg of the other. The aggregation in water is controlled by both the ChlA-ChlA and ChlA-water interactions where hydrophobicity of the phytol tail as well as the coordination of a water molecule with the Mg play important role.

Molecular modeling and simulations of AXT show that the aggregation of the molecule in a co-solvent mixture of water and ethanol depends on the ratio of the

co-solvents. Aggregates are observed in mixtures in which the water content is more than 50%. The results of the simulations show that hydrophobicity of the conjugated chain in astaxanthin plays a major role in aggregation.

The parameters of both ChlA and AXT developed in the work presented in this thesis can be adapted to study the structural and dynamic properties of the different chlorophylls and carotenoids in various biological environments. Apart from that, chlorophylls as well as their derivatives like chlorophyllides and porphyrins, and carotenoids can be self-assembled on various substrates, and as such nano-assemblies are efficient light absorbers, they are being investigated for potential applications in photovoltaics and artificial photosynthesis. However, the structure of the aggregates need to be controlled for such applications. One of the ways to control aggregation on surfaces is to change the hydrophobicity of the surfaces for which the surfaces, like silica surfaces, need to be functionalized with hydrophobic functional groups; modeling of PhTMS is done for this purpose. The parameters of the PhTMS model can be used in modeling hydrophobic phenyl groups on silica surfaces.

Different processes like the formation of excitons, their motion, energy dissipation, charge separation, etc. that follow the absorption of photons, and which play important role in the functionality of nano-assemblies, are not well known. The experiments presented in this thesis describe the development and implementation of two closely related non-linear optical techniques, PPSNOM and transient gratings, to investigate the ultra-fast processes in nano-systems.

The results of the investigation of exciton dynamics in thin films of PTCDA using PPSNOM shows that the technique can be used to study local dynamics in nano-structures with a few tens of nano-meter spatial resolution. The chemical selectivity inherent to this technique allows chemical imaging of the samples with very high lateral spatial resolution. The technique can be further improved by using high-repetition rate laser systems that are commercially available. This will allow video-

rate chemical imaging. This technique, however, is useful in studying the dynamics in thin films and nano-structures of functional molecules that have few tens of nanometer thickness. This limitation can be overcome by transient grating technique. The exciton dynamics studied in few nano-meters to sub-nanometer thin films show that the technique could potentially be used to study ultra-fast process in mono-layers and sub-monolayer structures. The results also show that the technique is sensitive to the organization of nano-structures, mainly the distance between the nano-structures. Transient grating technique can also be easily extended to more sophisticated photon-echo and two-dimensional spectroscopy which allow better understanding the coherent processes in the nano-systems.

Abbreviations

AFM: Atomic Force Microscopy.

AXT: Astaxanthin.

ChlA: Chlorophyll A.

B3LYP: Becke 3-parameter Lee Yang Parr.

CCD: Charge Coupled Device.

CHELPG: CHarges from Electrostatic Potentials using a Grid based method.

LHC: Light Harvesting Complex.

LINCS: LINnear Constraint Solver.

LJ: Lennard Jones.

OKE: Optical Kerr Effect.

OPA: Optical Parametric Amplification.

OPLS: Optimized Parameters for Liquid Simulations.

OPLS-AA: Optimized Parameters for Liquid Simulations - All Atom.

PCM: Polarizable Continuum Model.

PhTMS: Phenyltrimethoxysilane.

PME: Particle Mesh Ewald.

PMF: Potential of Mean Force.

POSS: Polyhedral Organo Silane Structures.

PPSNOM: Pump Probe Scanning Near-field Optical Microscopy.

PTCDA: 3,4,9,10 Perylenetetracarboxylic dianhydride.

QM: Quantum Mechanical.

RDF: Radial Distribution Function.

RIN: Running Integration Number.

SDF: Spatial Distribution Function.

SNOM: Scanning Near-field Optical Microscopy.

WLC: Worm Like Chain